

A scanning eye-safe rotational Raman lidar in the ultraviolet for measurements of tropospheric temperature fields

Dissertation zur Erlangung des Doktorgrades
der Naturwissenschaften (Dr. rer. nat.)

Fakultät Naturwissenschaften
Universität Hohenheim

Institut für Physik und Meteorologie

vorgelegt von
Marcus Radlach

aus Gotha
2009

This thesis was accepted as a doctoral dissertation in fulfillment of the requirements for the degree “Doktor der Naturwissenschaften” by the Faculty of Natural Sciences at the University of Hohenheim, Stuttgart, Germany on 13 January 2009.

Date of oral examination: 9 February 2009

Examination committee:

Supervisor and reviewer: Prof. Dr. Volker Wulfmeyer
Institute of Physics and Meteorology,
University of Hohenheim

Co-reviewer: Prof. Dr. Christoph Kottmeier
Institute for Meteorology and Climate Research,
University of Karlsruhe

Additional examiner: Prof. Dr. Kurt Jetter
Institute of Applied Mathematics and Statistics,
University of Hohenheim

Dean: Prof. Dr. Heinz Breer
Faculty of Natural Sciences,
University of Hohenheim

Abstract

Within the frame of the virtual Institute COSI^{TRACKS} the first scanning rotational Raman lidar has been developed and deployed successfully in two large field campaigns. This has allowed new investigations of the convective boundary layer and contributed to studies on the initiation of convection during the PRINCE campaign (PRediction, Identification and trackiNg of Convective cElls) in July 2006 and the COPS experiment (Convective and Orographically-induced Precipitation Study) from June to August 2007. The University of Hohenheim rotational Raman lidar was deployed in both these campaigns on Hornisgrinde (48.61 °N, 8.20 °E, 1161 m above sea level), the highest peak in the Northern Black Forest in southwest Germany.

The lidar provides measurements of atmospheric temperature fields in the troposphere with high spatial and temporal resolution at day and night. Daytime scanning temperature measurements within a range of 3 km using a temporal resolution of 169 s and a moving average of 300 m in range show statistical temperature uncertainties of less than 1 K while pointing at 21 directions. Temperature uncertainties of less than 1 K are achieved during nighttime up to a range of 8 km using a temporal resolution of 3 minutes and a range resolution of 300 m. The lidar resolves also turbulence in the convective boundary layer, e.g., at 470 m height with a temporal resolution of 10 s and statistical uncertainties of only 0.41 K.

In addition to temperature, also the particle backscatter coefficient and the particle extinction coefficient are measured independently.

The instrument operates with a primary wavelength of 355 nm. This has instrumental advantages compared to 532 nm but also yields eye-safety beyond a range of ~ 500 m which facilitates the deployment. Highly efficient spectral separation of the atmospheric backscatter signals is performed by a polychromator with narrow-band interference filters in a sequential setup. The spectral characteristics of these filters were optimized with respect to high measurement performance in the daytime planetary boundary layer and the lower free troposphere.

Pioneering measurements of the 2-dimensional temperature distribution in the lower troposphere in the vicinity of a mountain ridge are presented.

Zusammenfassung

Im Rahmen des virtuellen Institutes COSI^{TRACKS} wurde das erste abtastende Rotations-Raman-Lidar entwickelt und in zwei großen Feldmesskampagnen erfolgreich eingesetzt. Dies ermöglichte neue Untersuchungen in der konvektiven Grenzschicht und trug während der Messkampagne PRINCE (PRediction, Identification and trackiNG of Convective cElls) im Juli 2006 und dem COPS Experiment (Convective and Orographically-induced Precipitation Study) von Juni bis August 2007 zu Studien der Auslösung von Konvektion bei. Das Rotations-Raman-Lidar der Universität Hohenheim wurde während beider Messkampagnen auf der Hornisgrinde (48.61 °N, 8.20 °O, 1161 m ü. NN), der höchsten Erhebung im Nordschwarzwald im Südwesten Deutschlands, stationiert.

Das Lidar erlaubt Messungen atmosphärischer Temperaturfelder in der Troposphäre mit zeitlich und räumlich hoher Auflösung am Tag und in der Nacht. Abtastende Temperaturmessungen in 21 unterschiedlichen Richtungen am Tage bis zu einer Entfernung von 3 km, mit einer zeitlichen Auflösung von 169 s und einer räumlichen Glättungslänge von 300 m zeigen statistische Messunsicherheiten der Temperatur von weniger als 1 K. Messunsicherheiten von weniger als 1 K werden in der Nacht mit einer zeitliche Auflösung von 3 Minuten und einer Entfernungsauflösung von 300 m bis zu einer Entfernung von 8 km erreicht. Das Lidar löst ebenso die Turbulenz in einer konvektiven Grenzschicht auf, z.B. in einer Höhe von 470 m mit einer zeitlichen Auflösung von 10 s und statistischen Unsicherheiten von nur 0.41 K.

Zusätzlich zur Temperatur werden unabhängig voneinander auch der Partikel-Rückstreukoeffizient und der Partikel-Extinktionskoeffizient gemessen.

Das Gerät wird bei einer Primärwellenlänge von 355 nm betrieben, dies bietet im Vergleich zu 532 nm instrumentelle Vorteile, aber auch die Augensicherheit wird in einer Entfernung von ~ 500 m erreicht, was den Einsatz sehr erleichtert. Eine sehr effiziente spektrale Aufteilung des atmosphärischen Rückstreusignals erfolgt in der Strahlseparationseinheit mit schmalbandigen Interferenzfiltern in einem sequentiellen Aufbau. Die spektralen Eigenschaften der Filter wurden im Hinblick auf hohe Effizienz für Tageslichtmessungen in der planetaren Grenzschicht und der unteren freien Troposphäre optimiert.

Erstmals werden Messungen der 2-dimensionalen Temperaturverteilung in der unteren Troposphäre in der Umgebung eines Berges gezeigt.

Contents

Contents	i
List of abbreviations	iii
Chapter 1 Introduction	1
Chapter 2 Lidar	5
2.1 Lidar technique	5
2.2 Atmospheric scattering processes	5
2.3 Pure rotational Raman scattering	8
2.4 Lidar equation	9
Chapter 3 Atmospheric temperature measurements by remote sensing	12
Chapter 4 System setup	19
4.1 Filter optimization	19
4.1.1 Basic concept	19
4.1.2 Filter optimization results	22
4.1.3 Discussion and conclusion	25
4.2 The scanning rotational Raman lidar of University of Hohenheim	26
4.2.1 Transmitter setup	28
4.2.2 Receiver setup	31
Chapter 5 Data analysis	35
5.1 Lidar calibration	35
5.2 Analysis of systematic errors	39
5.2.1 Stability of calibration function: laser drift	39
5.2.2 Stability of calibration function: ambient conditions	41
5.2.3 Leakage of elastic signal into the inelastic channels	43
Chapter 6 Test measurements at University of Hohenheim	46
Chapter 7 Temperature measurements during the field campaign PRINCE in July 2006	50
7.1 The PRINCE campaign	50

7.2	Vertical temperature measurements	52
7.3	Scanning temperature measurements during the night of 10 July 2006	52
7.4	Performance during PRINCE	57
Chapter 8 Temperature measurements during the field campaign		
	COPS in summer 2007	61
8.1	COPS	61
8.2	Daytime scanning measurements on 25 August 2007	62
8.3	Performance	68
	8.3.1 Statistical temperature uncertainties in dependence on the solar elevation angle	68
	8.3.2 Temporal and range resolution	72
8.4	Spectral analysis of a high resolved temperature measurement in the boundary layer on 14 June 2007	74
	8.4.1 Temperature variance	76
	8.4.2 Results	78
Chapter 9 Conclusion and outlook 86		
Appendices 91		
Appendix A Optimizing filter parameters 93		
	A.1 Gaussian filter curves	93
	A.2 Simulated filter curves by Barr	97
Appendix B Lidar operation times and measurement modes during PRINCE and COPS 100		
	B.1 PRINCE	100
	B.2 COPS	101
Bibliography 105		
Acknowledgements 116		

List of abbreviations

ACF	autocovariance function
AERI	atmospheric emitted radiance interferometer
AGL	above ground level
AOI	angle of incidence
ASL	above sea level
CAPE	convective available potential energy
CIN	convective inhibition
CI	convective initiation
COPS	Convective and Orographically-induced Precipitation Study
COSI-TRACKS	Convective Storms Virtual Institute, Transporte und chemische Umsetzungen in konvektiven Systemen
CPS	counts per second
CWL	central wavelength
DIAL	differential absorption lidar
DWD	German Weather Service (Deutscher Wetterdienst), Offenbach, Germany
FWHM	full width at half maximum
HALO	High Altitude and Long Range Research Aircraft
HSRL	high spectral resolution lidar
IfT	Institute for Tropospheric Research, Leipzig, Germany
IMAA-CNR	Instituto di Metodologie per l'Analisi Ambientale Consiglio Nazionale delle Ricerche, Potenza, Italy
IMK-FZK	Institute of Meteorology and Climate Research, Research Center Karlsruhe (Institut für Meteorologie und Klimaforschung, Forschungszentrum Karlsruhe), Germany
IOP	intensive observations period
IPA-DLR	Institute of Atmospheric Physics, German Aerospace Center (Deutsches Zentrum für Luft- und Raumfahrt), Oberpfaffenhofen, Germany
IPA (Mainz)	Institute for Atmospheric Physics, University of Mainz, Germany
IPM	Institute of Physics and Meteorology, UHOH, Germany
IRCTR	International Research Center for Telecommunications-transmission and Radar, University of Delft, The Netherlands
lidar	light detection and ranging
NASA GSFC	National Aeronautics and Space Administration, Goddard Space Flight Center, Greenbelt, MD, USA
Nd:YAG	Neodymium-doped Yttrium Aluminum Garnet

NWP	numerical weather prediction
PAEP	power-aperture-efficiency product
PBL	planetary boundary layer
PPI	plane position indicator
PRINCE	PRediction, Identification and trackiNg of Convective cElls
radar	radio detection and ranging
RASC	Radio Science Center for Space and Atmosphere, Kyoto, Japan
RASS	radio acoustic sounding system
RFOV	receiver field-of-view
RHI	range-height-indicator
RMS	root mean square
RR	rotational Raman
SNR	signal-to-noise ratio
TARA	Transportable Atmospheric Radar
UHOH	University of Hohenheim, Stuttgart, Germany
UNIBAS	University of Basilicata, Potenza, Italy
UTC	Universal Time Coordinated
UV	ultraviolet
WMO	World Meteorological Organization, Geneva, Switzerland

Chapter 1

Introduction

Temperature is a state variable of the Earth's atmosphere. The atmosphere is divided into several layers, based on the mean vertical profile of temperature.

The lowest part of the atmosphere is influenced by the Earth surface through frictional forcing (Stull, 1988). This layer is primarily characterized by turbulent processes and is called the planetary boundary layer (PBL). It is particularly influenced by the underlying topography. The PBL ranges from a few meters up to 2–3 km above ground. Above the PBL, the free troposphere exists which in principle is characterized by advection processes. Within the troposphere the temperature decreases with height. The temperature minimum at the top of the troposphere is called tropopause. On average it occurs between 10–12 km above sea level (ASL) in the Mid-latitudes. Above this zone, the mean temperature is isothermal and eventually increases with height in the stratosphere.

The atmospheric temperature in general is of utmost importance for many processes in the atmosphere. Also, it has an influence on the human well-being, e.g., the air quality in wintertime can significantly decrease in the Mid- and High-latitudes due to radiative cooling at night and a developing strong temperature inversion close to the ground. Hence, pollutants are aggregated below the inversion layer causing severe health hazards in populated areas (Janhäll et al., 2006; Malek et al., 2006).

Research interests of the upper troposphere/lower stratosphere, for which the temperature is important, include atmospheric chemistry, e.g.: the formation of polar stratospheric clouds by heterogeneous chemical reactions. Different cloud types with specific chemical and optical properties can form depending on the ambient temperature (Rosen et al., 1997; Stein et al., 1999). These clouds occur mainly in the polar regions of the Earth being responsible for the ozone depletion (Crutzen and Arnold, 1986; Hofmann et al., 1991).

Within this work, the diurnal variation of temperature layering in the free troposphere and the PBL is of particular interest. The temperature gradient together with humidity rules atmospheric stability. Thus, the initiation of convection or the propagation of gravity waves depends on the temperature stratification. Temperature differences between valleys and mountains in complex terrain due to differential heating develop local circulation systems. This may trigger deep convection if instability is present in the troposphere (Lugauer and Winkler, 2005).

For a comprehensive understanding of such processes, it is desirable to have an instrument which is capable of measuring temperature from close to the ground up to the tropopause. Furthermore, it is beneficial that this device is also capable of performing

scanning measurements. Observing the spatial structure of atmospheric key parameters allows one to get new insight into PBL processes and the dynamics of the lower troposphere.

The accuracy and resolution of such an instrument have to be rather high meeting the observational requirements defined by the World Meteorological Organization (WMO) (Gustafsson et al., 2001). An accuracy for temperature measurements of 0.5–1.5 K throughout the whole troposphere is needed in combination with a vertical resolution of 10 m and 100 m with an observing cycle of 10 minutes and 30 minutes within the PBL and the whole troposphere, respectively. These requirements apply for both day- and nighttime measurements. It is important to mention that a vertical and temporal resolution of 300 m and 1 h, respectively, already fulfill useful requirements within the PBL. Such high spatial and temporal resolution can only be achieved by active remote sensing techniques.

Lidar (light detection and ranging) is an active remote sensing technique that allows temporal- and range-resolved investigations, e.g., of temperature, water vapor, wind and aerosol optical properties in the atmosphere by observing light scattering of molecules and aerosols. At date, the rotational Raman (RR) technique is the most reliable method for remote sensing of temperature (Behrendt, 2005) in the troposphere. Therefore, the temperature measurements in this thesis are performed according to the RR technique.

At University of Hohenheim (UHOH), Stuttgart, Germany, a scanning RR lidar has been developed. This work was carried out within COSI-TRACKS (Convective Storms Virtual Institute), a virtual institute within the “Impuls- und Vernetzungsongs” of the Helmholtz Research Association between the Institute of Meteorology and Climate Research at Research Center Karlsruhe (IMK-FZK), Institute of Atmospheric Physics at the German Aerospace Center (IPA-DLR) Oberpfaffenhofen, Institute for Atmospheric Physics (IPA) at University of Mainz and the Institute of Physics and Meteorology (IPM) at UHOH. The goal of COSI-TRACKS was to combine modeling and measuring efforts to obtain a deeper understanding about processes initiating and modifying convective storms. The joint measurement campaign PRINCE (PRediction Identification and trackiNG of Convective cElls) was carried out in July 2006 in the Northern Black Forest, Germany. A unique setup of state-of-the-art remote sensing instruments with scanning capability for 3-dimensional observation of the atmosphere was deployed on the mountain Hornisgrinde (48.61 °N, 8.20 °E, 1161 m ASL). In addition, different flight patterns were performed by the research aircraft DO-128 (Corsmeier et al., 2001) of the Technical University of Braunschweig, Germany. Details are described in Chapter 7. A case study of 12 July 2006 of the experiment (Groenemeijer et al., 2008) and the predictability of convection in numerical weather prediction (NWP) models was assessed (Trentmann et al., 2008). The techniques and measurement strategies that were developed and applied successfully during this experiment were utilized one year later during the international field experiment COPS (Convective Orographically-induced Precipitation Study).

The field campaign COPS took place from 1 June–31 August 2007 in the southwestern part of Germany and eastern France. The COPS region stretches from the Swabian

Jura over the Black Forest to the Rhine Valley and the Vosges mountains in eastern France. COPS (Behrendt et al., 2006; Wulfmeyer et al., 2008a,c) is a key part of the German Priority Program “*Praecipitationis Quantitativae Predictio*” of the German Research Foundation and is endorsed as Research and Development Project in the World Weather Research Program. It is the overarching objective of COPS to advance the quality of forecasts of orographically-induced convective precipitation by 4D observations and modeling of its life cycle. A large suite of state-of-the-art ground-based and airborne remote sensing systems were combined with in-situ instruments. A transect of three measurement sites (supersites) was established through the Northern Black Forest. Two additional supersites were located in the French Vosges mountains and on the east side of the Black Forest near Stuttgart, Germany, respectively. Further details are given in Chapter 8.

The radiation source of the UHOH RR lidar is the frequency tripled wavelength of Nd:YAG of 355 nm. The system is optimized for daytime temperature measurements in the lower troposphere but shows also high performance during nighttime and allows then also stratospheric measurements up to the lower stratosphere (Radlach et al., 2006, 2008a). Detailed simulations were performed in order to find the most suitable filter parameters to extract the RR signals out of the backscattered light. These simulations were performed with respect to different background signals in order to simulate daytime performance. The better optical performance of narrow-band interference filters in the ultraviolet (UV) that can be realized today leads to a better system performance for tropospheric temperature profiling than for comparable systems in the visible domain due to the higher molecular backscatter coefficient and a higher efficiency of the detectors at lower wavelengths. Details are described in Chapter 3. The RR receiver makes use of a cascade filter mounting which allows a high efficiency. This setup was first introduced by Behrendt and Reichardt (2000) and used near the frequency doubled wavelength of Nd:YAG of 532 nm.

The UHOH RR lidar can be operated in a scanning mode which allows measurements of temperature fields. This is particularly beneficial for process studies in complex terrain because of horizontal inhomogeneities that exist which are considered to be important to understand the mechanisms of locally driven convection.

This thesis consists of nine chapters. Chapter 2 describes basic principles of lidar and Raman scattering in the atmosphere, followed by an explanation of the RR technique and the lidar equation. Chapter 3 gives an overview about active and passive remote sensing techniques being capable for temperature measurements in the lower troposphere. In Chapter 4, the filter optimization calculations are presented and the system setup is described. Chapter 5 explains the lidar calibration and discusses systematic errors. First test measurements of the new RR lidar are presented in Chapter 6. The lidar data were acquired at UHOH campus in March 2006. An example of the measurement obtained on the mountain Hornisgrinde in the Northern Black Forest during the PRINCE experiment in summer 2006 is described in Chapter 7. Scanning temperature measurements along a west-east transect during nighttime is discussed in detail. Chapter 8 describes the results obtained during the campaign COPS in 2007. For this campaign the total system performance was improved compared to the previous

deployments which allowed the first scanning temperature measurements in daytime. The statistical uncertainties are analyzed in dependence on the solar elevation angle. The chapter closes with a spectral analysis of a high-resolved temperature time series. A discussion of the results and an outlook are given in Chapter 9.

Chapter 2

Lidar

2.1 Lidar technique

Lidar is an instrument for active remote sensing of various atmospheric variables (e.g. Weitkamp (2005)). The light source is usually a high-power laser that emits short pulses of monochromatic light at a specific wavelength λ into the atmosphere. Eventually, this laser pulse interacts with molecules and particles in the atmosphere. Lidar uses not only the visible part of the electromagnetic spectrum but the range from the UV (~ 200 nm) to the infrared wavelength region (~ 11 μm). Molecules and aerosols are responsible for scattering and absorption of the incident light. Scattering by molecules include elastic and inelastic scattering processes whereas aerosols usually cause only elastic scattering. A telescope collects the backscattered light which then can be analyzed in a polychromator by one or several detectors. The height information is derived from the detection time t taking into account that the laser pulse travels with the speed of light c through the atmosphere. Thus, the range R from the lidar to the scattering volume is

$$R = \frac{1}{2}ct . \quad (2.1.1)$$

2.2 Atmospheric scattering processes

The emitted laser pulse interacts with the constituents along its way through the atmosphere. In this section only the scattering by molecules, which are much smaller than the laser wavelength, is discussed.

For elastic scattering, the molecule's quantum state is not changed. Thus, the energy of the scattered photon is similar to that of the incident photon. If the energy is changed during the scattering process, the frequency of the scattered photon is different. This scattering process is termed inelastic or Raman scattering. Hereinafter, the quantity wavenumber $\tilde{\nu}$ is used with the unit cm^{-1} , which is linked to frequency ν and wavelength λ by $\tilde{\nu} = \nu/c = 1/\lambda$. The shift in wavenumber

$$\Delta\tilde{\nu} = \tilde{\nu}_S - \tilde{\nu}_0 = \frac{\Delta E}{hc} \quad (2.2.1)$$

is specific to the respective molecule. The wavenumber of the incident photon is $\tilde{\nu}_0$ and that of the scattered photon $\tilde{\nu}_S$. ΔE is the difference between the energy levels that are involved in the scattering process and h is Planck's constant.

When energy is absorbed by the molecule and a higher energy level is reached by it, then the scattered photon has a lower wavenumber and, therefore, has a longer

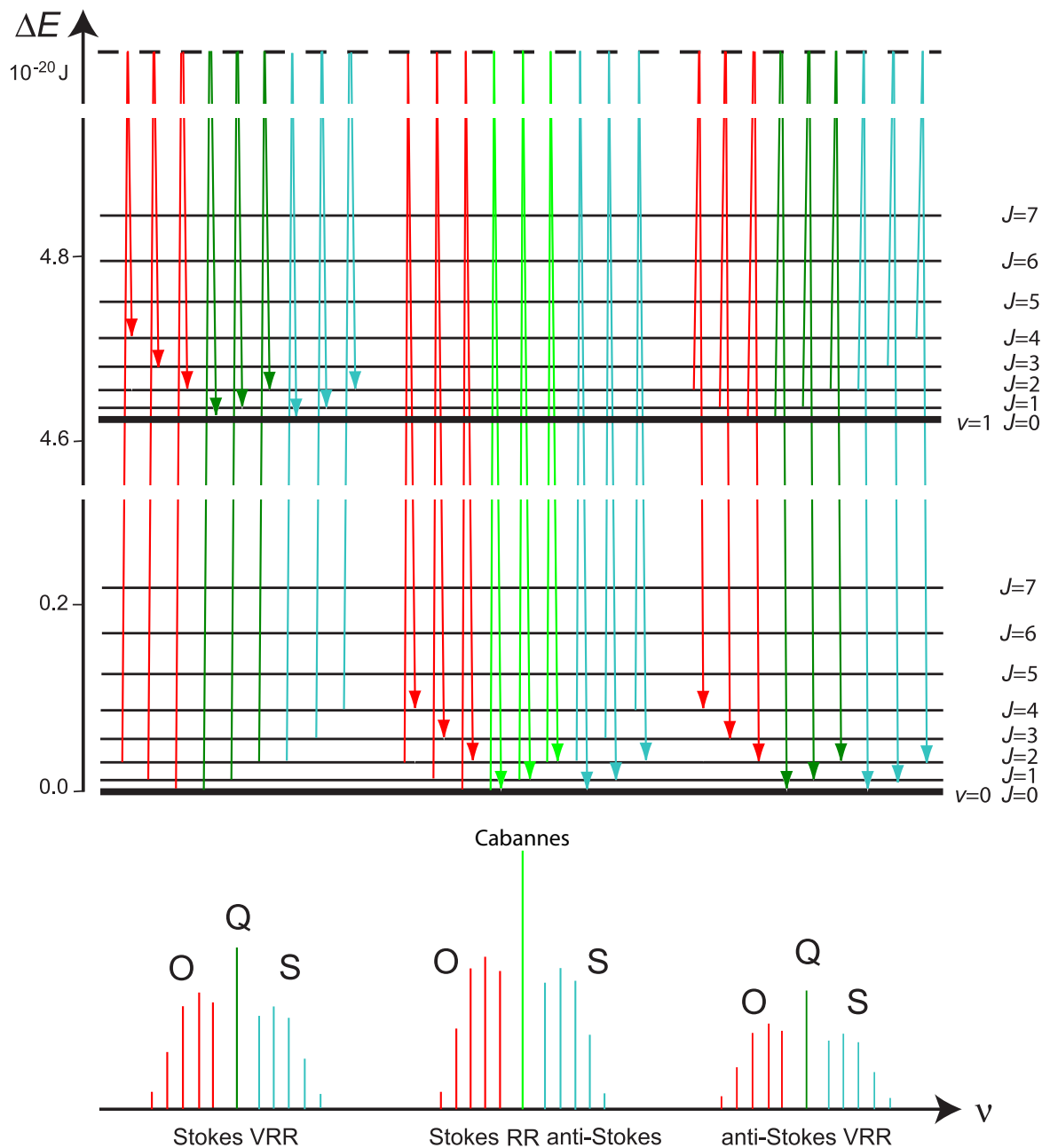


Figure 2.1: Schematic drawing of the N_2 molecule's Raman transitions for the first vibrational level and the lowermost rotational levels. In the lower part the resulting spectrum is shown. VRR refers to vibrational and rotational transitions and RR to pure rotational transitions. The figure is adapted from Wandinger (2005).

wavelength. This process is called Stokes Raman scattering. If energy is transferred from the molecule to the scattered photon, $\tilde{\nu}_S$ is increased and, as a result, the wavelength becomes shorter. This process is called anti-Stokes Raman scattering. Possible transitions exist between the rotational levels J and the vibrational levels v . Considering a change of the rotational level, the selection rules for homonuclear diatomic molecules (Herzberg, 1950), e.g. N_2 and O_2 , are: $\Delta J = \pm 2$, $\Delta v = 0$. On the other hand, for transitions where the vibration-rotation levels are changed, the selection rules are: $\Delta J = \pm 2$, $\Delta v = \pm 1$. Figure 2.1 shows a schematic overview of the possible energy transitions of nitrogen. Elastic scattering corresponds to the transitions where J and v are not changed yielding the Cabannes line. The Cabannes line is composed of the Brillouin doublet (change of the molecule's kinetic energy) and the central Gross or Landau-Placzek line (no change of energy). Transitions of $\Delta J = +2$ and $\Delta J = -2$ lead to the S and O branch, respectively, with $\Delta J = J_1 - J_2$. J_1 is the initial rotational quantum state and J_2 the final state. If only the rotational quantum number is changed with $\Delta J = \mp 2$ one gets the pure Stokes and anti-Stokes RR lines to both sides of the Cabannes line. Other transitions that lead to both a change of the vibrational and rotational levels result in the Stokes and anti-Stokes vibration-rotation bands with selection rules $\Delta v = +1$, $\Delta J = \pm 2$ and $\Delta v = -1$, $\Delta J = \pm 2$, respectively. In case the rotational level remains unchanged, the resulting line with $\Delta v = \pm 1$ is called the Q branch.

The energy levels are well known for homonuclear diatomic molecules like N_2 and O_2 . According to quantum mechanics, the energy levels of homonuclear diatomic molecules are given by the model of a freely rotating harmonic oscillator (Long, 2002). Thus, the energy of the vibrational level is

$$E_{vib,v} = hc\tilde{\nu}_{vib}(v + 1/2), \quad v = 0, 1, 2, \dots \quad (2.2.2)$$

$\tilde{\nu}_{vib}$ is the oscillator frequency of the molecule and v is the vibrational quantum number. The rotational energy with rotational quantum number J is calculated by

$$E_{rot,J,v} = hc[B_v J(J+1) - D_v J^2(J+1)^2], \quad J = 0, 1, 2, \dots, \quad (2.2.3)$$

with the rotational constant B_v and the centrifugal distortion D_v . The later parameter describes the contribution of stretching of the molecule's axis due to rotation and is usually negligible for small J 's. Furthermore, the two constants depend on the molecule's vibrational level. The constants are given in Butcher et al. (1971); Bendtsen (1974) and Long (2002). There is a branch of rotational lines existing for each vibrational level. An individual vibration-rotation energy level is calculated by the sum of Eqs. (2.2.2) and (2.2.3). Under atmospheric conditions most of the molecules are not excited to higher vibrational quantum states. The most probable transitions exist between the pure Stokes and anti-Stokes rotational levels and the first Stokes vibrational level including the corresponding rotational levels. About 3% of the scattered light by molecules in the Earth atmosphere are attributed to pure RR scattering while the strongest RR line of, e.g., N_2 is by approximately 5×10^{-4} weaker than the Cabannes line. The anti-Stokes vibrational levels are not useful for detection by lidar, because

they are several orders of magnitude weaker in intensity. Elastic scattering of aerosols or cloud particles are by 2–4 orders of magnitude more intense than elastic scattering of molecules. For this thesis, only the pure RR scattering of the main atmospheric constituents N_2 and O_2 is of interest.

2.3 Pure rotational Raman scattering

The energy levels for the rotational quantum states J are described by Eq. (2.2.3). The wavenumber shift between the single quantum states is calculated by applying Eq. (2.2.3) to Eq. (2.2.1). Following the selection rule $J \rightarrow J + 2$ for Stokes transitions gives

$$\Delta\tilde{\nu}_{\text{rot,St}}(J) = \tilde{\nu}_{J+2} - \tilde{\nu}_J = -4B_0(J + 3/2) + D_0[3(2J + 3) + (2J + 3)^3], \quad J = 0, 1, 2, \dots \quad (2.3.1)$$

For transitions in the anti-Stokes band the selection rule is $J \rightarrow J - 2$ and thus

$$\Delta\tilde{\nu}_{\text{rot,A-St}}(J) = \tilde{\nu}_{J-2} - \tilde{\nu}_J = 4B_0(J - 1/2) - D_0[3(2J - 1) + (2J - 1)^3], \quad J = 2, 3, 4, \dots \quad (2.3.2)$$

The values for B_0 and D_0 are listed in Table 2.1. The differential backscatter cross section for single lines can be written as (Behrendt, 2005)

$$\left(\frac{d\sigma}{d\Omega}\right)_{\text{RR}}^{\pi} = \frac{112\pi^4}{15} \frac{g(J)hcB_0(\tilde{\nu}_0 + \Delta\tilde{\nu}(J))^4\gamma^2}{(2I + 1)^2 kT} X(J) \exp\left(-\frac{E_{\text{rot}}(J)}{kT}\right). \quad (2.3.3)$$

It is for the

$$\text{Stokes branch: } X(J) = \frac{(J + 1)(J + 2)}{2J + 3}, \quad (2.3.4)$$

$$\text{and the anti-Stokes branch: } X(J) = \frac{J(J - 1)}{2J - 1}. \quad (2.3.5)$$

The nuclear weighting factor $g(J)$ depends on the nuclear spin I which is $I_{O_2} = 0$ and $I_{N_2} = 1$. For the initial quantum state, this gives for J even-numbered $g(J) = 6$, $g(J) = 0$ and for J odd-numbered $g(J) = 3$, $g(J) = 1$ for N_2 and O_2 , respectively. γ^2 is the anisotropy of the molecular polarizability tensor, k is Boltzmann's constant and T the temperature.

The energy levels of the quantum states J follow a Boltzmann distribution. Therefore, the backscatter cross section of the individual RR lines are temperature dependent as can be seen in Eq. (2.3.3). The pure RR spectra, calculated for an incident laser wavelength of 354.7 nm, a nitrogen and oxygen content of 0.781 and 0.209, respectively, at temperatures of 300 K and 250 K are shown in Fig. 2.2. For decreasing temperatures, RR lines close to the exciting wavelength λ_0 increase in intensity, whereas RR lines farther apart show an intensity decrease. This characteristic can be used to measure atmospheric temperature by extracting two regions out of the spectrum with reversed temperature dependency as suggested by Cooney (1972).

Table 2.1: Rotational constant B_0 and centrifugal distortion D_0 for N_2 and O_2 taken from Bendtsen (1974) and Butcher et al. (1971), respectively. The anisotropy of the molecular polarizability tensor γ^2 is taken from Buldakov et al. (1979).

Gas	B_0, cm^{-1}	D_0, cm^{-1}	γ^2, cm^6
N_2	1.98957	$5.76 \cdot 10^{-6}$	$0.51 \cdot 10^{-48}$
O_2	1.43768	$4.85 \cdot 10^{-6}$	$1.27 \cdot 10^{-48}$

Figure 2.2 shows the position of the interference filters that were used in this thesis in order to extract the signals out of the RR spectrum. Further details about the interference filters are given in Sect. 4.2.

2.4 Lidar equation

For a single scattering event at the wavelength λ , the power of the lidar signal $P_\lambda(R)$ depending on the range R is described by the lidar equation. For elastic scattered light at the laser wavelength λ_0 , it reads

$$P_{\lambda_0}(R) = P_0 \frac{c\tau}{2} \frac{O(R)}{R^2} A_T \eta_{\lambda_0} \beta_{\lambda_0}(R) \exp \left[-2 \int_0^R \alpha_{\lambda_0}(R') \, dR' \right], \quad (2.4.1)$$

with

- $P_{\lambda_0}(R)$ detected signal power at wavelength λ_0 and range R ,
- P_0 mean laser power per pulse,
- τ pulse duration,
- c speed of light,
- $O(R)$ overlap function of the laser beam and the receiver field-of-view,
- A_T surface area of the receiving telescope,
- η_{λ_0} system efficiency at wavelength λ_0 ,
- $\beta_{\lambda_0}(R)$ backscatter coefficient at wavelength λ_0 and
- $\alpha_{\lambda_0}(R)$ extinction coefficient at wavelength λ_0 .

The overlap function $O(R)$ describes the geometry of the laser beam in relation to the receiver field-of-view (RFOV). $O(R)$ becomes 1 when the laser beam is completely in the RFOV. The backscatter coefficient $\beta_{\lambda_0}(R)$ gives the relative scattered intensity with respect to the incident radiation. For elastic scattering processes, $\beta_{\lambda_0}(R)$ is the sum of the molecular and the particle backscatter coefficient. The extinction coefficient $\alpha_{\lambda_0}(R)$ characterizes the attenuation of the radiation at λ_0 due to scattering and absorption of molecules and particles in the atmosphere. The attenuation occurs two times, as the radiation is transmitted through the atmosphere which is on the way into the atmosphere and on the way back to the receiver.

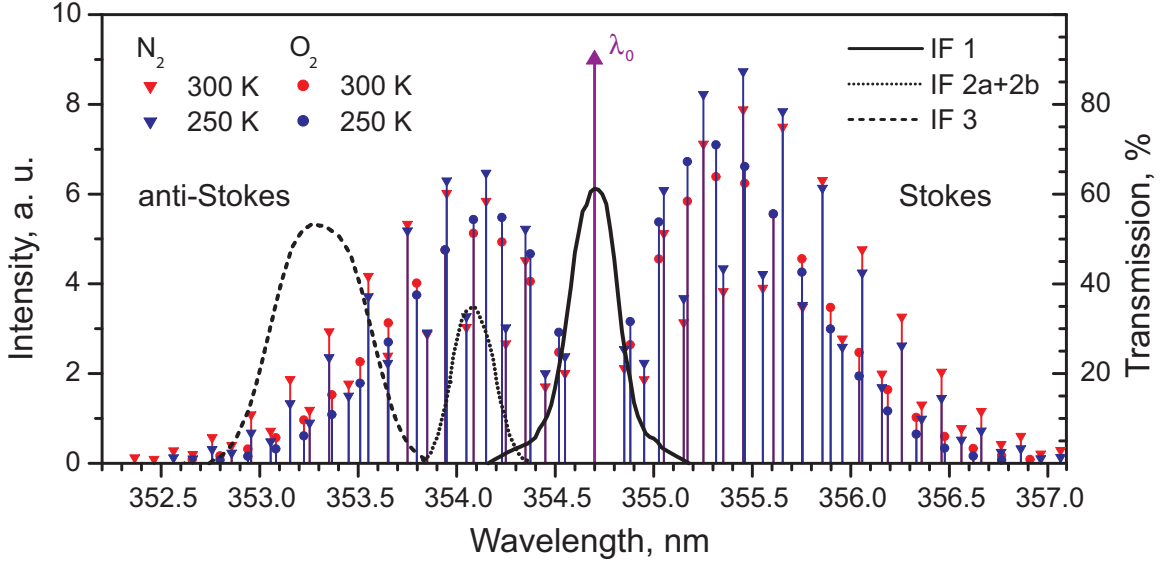


Figure 2.2: Pure RR spectrum of N_2 and O_2 with atmospheric content of 0.781 and 0.209, respectively, calculated for atmospheric temperatures of 250 K and 300 K. The exciting laser wavelength of 354.7 nm is denoted by λ_0 . The transmission curves of the narrow-band multi-cavity interference filters are shown in the configuration used nearly exclusively in the UHOH RR lidar (see Sect. 4.2.2).

For the detection of a Raman signal $P_{\lambda_R}(R)$, the lidar equation reads

$$P_{\lambda_R}(R) = P_0 \frac{c\tau}{2} \frac{O(R)}{R^2} A_T \eta_{\lambda_R} \beta_{\lambda_R}(R) \exp \left[- \int_0^R (\alpha_{\lambda_0}(R') + \alpha_{\lambda_R}(R')) dR' \right]. \quad (2.4.2)$$

The backscattered light is attenuated at the Raman shifted wavelength λ_R in this case. η_{λ_R} is the system efficiency at that wavelength. The molecular backscatter coefficient $\beta_{\lambda_R}(R)$ is specific for the Raman scattering process. It reads

$$\beta_{\lambda}(R) = \sum_i \beta_{\lambda,i}(R) = \sum_i N_i(R) \left(\frac{d\sigma}{d\Omega} \right)_i^\pi, \quad (2.4.3)$$

with the differential backscatter cross section $\left(\frac{d\sigma}{d\Omega} \right)_i^\pi$. i denotes the atmospheric constituent, e.g. N_2 or O_2 , and N_i is the number density of the corresponding molecule. Equation (2.4.1) contains two parameters describing optical particle properties. These are the particle backscatter coefficient $\beta_{\text{par}}(\lambda_0)$ and the particle extinction coefficient $\alpha_{\text{par}}(\lambda_0)$. By detecting a Raman signal and one elastic signal, both of the parameters can be determined separately. In contrast to the conventional Raman method (Ansmann et al., 1992) that uses the Stokes-vibration Raman signal of N_2 or O_2 , the RR technique provides two temperature-dependent molecular signals with opposite temperature dependency. A weighted sum of both signals yields a temperature-independent reference signal P_{ref} which is used for calculating β_{par} and α_{par} (Behrendt et al., 2002).

The advantage here is the much higher signal intensity that is available compared to the vibrational signal of, e.g., N_2 or O_2 . Given that the Raman wavelength is within a few nanometers apart the laser wavelength, consequently, the differences in atmospheric transmission and a wavelength dependence of the particle extinction are negligible. The particle backscatter coefficient hence can be calculated by

$$\beta_{\lambda_0}^{\text{par}}(R) = -\beta_{\lambda_0}^{\text{mol}}(R) + (\beta_{\lambda_0}^{\text{par}}(R_0) + \beta_{\lambda_0}^{\text{mol}}(R_0)) \frac{P_{\lambda_R}(R_0)P_{\lambda_0}(R)N(R)}{P_{\lambda_R}(R)P_{\lambda_0}(R_0)N(R_0)} \quad (2.4.4)$$

and the particle extinction coefficient yields

$$\alpha_{\lambda_0}^{\text{par}}(R) = \frac{1}{2} \frac{d}{dz} \left(\ln \frac{N(R)}{P_{\lambda_R}(R)R^2} \right) - \alpha_{\lambda_0}^{\text{mol}}(R). \quad (2.4.5)$$

The number concentration N of the molecules is given by the temperature measurement of the lidar or alternatively can be calculated from a standard atmosphere or a radiosonde if available. For the calculation of the backscatter coefficient, a reference level R_0 is chosen where $\beta_{\lambda_0}^{\text{par}}(R_0) \ll \beta_{\lambda_0}^{\text{mol}}(R_0)$ (Ansmann et al., 1992). This thesis does not deal with the detailed analysis of optical particle properties, e.g.: the lidar ratio which is just the ratio of particle extinction and backscatter coefficient. This part of the work was carried out by Pal (2009).

Chapter 3

Atmospheric temperature measurements by remote sensing

Different passive and active remote sensing techniques for range-resolved temperature measurements are used today. Passive remote sensing instruments consist of a receiver which measures brightness temperatures at suitable wavelengths in the microwave or infrared region. They provide integral measurements which need special retrieval algorithms and a priori information to derive a profile of the parameter of interest. Such passive techniques are widely in use for satellite-based, airborne and ground-based measurements. Active remote sensing instruments make use of acoustic or electromagnetic pulses that are transmitted into the atmosphere. The backscattered signals are detected range-resolved by a receiver on the ground.

Lidar as an active remote sensing instrument allows range-resolved temperature measurements by different techniques (see Behrendt (2005) for a review). The integration technique is technically the most simple method. It needs just one elastic backscatter signal and makes use of the assumption that the lidar signal is proportional to the molecular number density in the atmosphere if the observed height region is free from particles (Chanin and Hauchecorne, 1984). The temperature is derived assuming hydrostatic equilibrium. A similar technique exists with the Raman-integration technique which uses a Raman shifted wavelength instead (Strauch et al., 1971; Keckhut et al., 1990). Both techniques yields only stratospheric and mesospheric temperature measurements.

The RR technique is the most widely used lidar technique for atmospheric temperature profiling in the troposphere. The use of the temperature dependence of the pure RR spectra for tropospheric temperature profiling was introduced by Cooney (1972). By extracting two portions out of the RR spectrum with different temperature dependency, it gives a direct measure of temperature. A high suppression of the elastically scattered light in the detection channels is necessary. Theoretical calculations showed that for a primary wavelength of 532 nm at least 7 orders of magnitude of suppression relative to the Cabannes line have to be achieved for undisturbed temperature measurements (Behrendt, 2000).

First experimental results were presented by Cooney and Pina (1976). They measured the temperature distribution in the height region between 600 and 1100 m above ground level (AGL) with measurement uncertainties of up to 4 K at 1100 m AGL. The radiation source used in this experiment was a ruby laser. In this concept, a beam splitter and narrow-band interference filters were used to extract the RR signals from the lidar return. A different receiver setup for detecting the RR signals was suggested by Arshinov et al. (1983). It is based on a grating monochromator. According to laboratory tests, this concept allows a suppression of up to 8 orders of magnitude of the Mie scattering. Due to the low efficiency of the gratings of about 1%, the first

measurements which were performed at a wavelength of 510 nm with a temporal resolution of 20 minutes and range resolution of 30 m yielded uncertainties of about 1.5 K at 1 km altitude. Further developments of commercially available high-power Nd:YAG lasers and better optical components that became available resulted in a higher system performance. Several ground-based systems exist today, e.g.: at Observatory of Haute Provence, France (Nedeljkovic et al., 1993), at Pennsylvania State University, PA, USA (Philbrick, 1994), at Institute for Tropospheric Research (IfT), Leipzig, Germany (Mattis et al., 2002), at GKSS Research Center Geesthacht, Germany (Behrendt and Reichardt, 2000), at the RASC (Radio Science Center for Space and Atmosphere) middle and upper radar observatory, Shigaraki, Japan (Behrendt et al., 2002) and at National Aeronautics and Space Administration, Goddard Space Flight Center (NASA GSFC), Greenbelt, MD, USA (Di Girolamo et al., 2004).

Behrendt and Reichardt (2000) introduced a sequential mounting of the receiving channels in the polychromator which yields high efficiency when separating the signals as well as a high suppression of elastically scattered light of 7 orders of magnitude (Behrendt, 2000). This system was operated at a wavelength of 532 nm. The atmospheric temperature was measured with uncertainties of less than 1 K up to 18 km AGL within an one-hour measurement interval and with an averaging window length of 960 m. With the availability of better interference filters from Barr Associates, MA, USA, afterwards, measurements from 2–20 km AGL were achieved applying a temporal and spatial average of 7 minute and 360 m, respectively, with temperature uncertainties less than 2 K (Behrendt et al., 2004a).

Behrendt and Weitkamp (2000) showed that the choice of a wavelength of 355 nm is advantageous for temperature measurements within the lower troposphere. Lower transmission values of about 15% compared to interference filters in the visible wavelength region made the use of 532 nm more suitable for measurements in the upper atmosphere. However, RR lidar systems mainly were operated in the visible domain at the frequency doubled wavelength of Nd:YAG of 532 nm so far because the higher laser power that is available at this wavelength and the better transmission of optical components, e.g. interference filters, which allowed for several years a higher receiver efficiency compared to UV wavelengths. Attempts were made also to use an UV wavelength for the lidar transmitter in the solar-blind region (Zeyn et al., 1996) but the first successful measurements in the UV were reported by Di Girolamo et al. (2004) using the frequency-tripled radiation of Nd:YAG laser of 355 nm and interference filters. Nighttime measurements extending up to 15 km AGL with a vertical resolution of 600 m and 90 minutes integration time showed statistical uncertainties of 1.5 K.

First daytime measurements with RR lidar were presented by using narrow-band interference filters and a primary wavelength of 532 nm by Behrendt et al. (2002) yielding uncertainties of less than 1 K up to heights of 7 km for an one hour measurement interval and a signal smoothing with a window length of 900 m. Di Girolamo et al. (2004) presented a measurement example in the early evening using the frequency tripled wavelength of Nd:YAG of 355 nm. An integration time of 90 minutes and a range resolution of 600 m yielded uncertainties of about 2 K up to 14 km AGL. The deviations with respect to a radiosounding were less than 3 K. Arshinov et al. (2005)

demonstrated daytime temperature profiling in the visible with gratings combined with a Fabry-Perot interferometer as a comb-filter. An one hour measurement period and a differential smoothing between 60 m and 500 m up to 11 km AGL yielded measurement uncertainties of about 2 K at 9 km altitude.

Due to technical improvements in manufacturing interference filters, filter transmissions with values of as high as 70% have been achieved in the UV wavelength region lately (Radlach et al., 2008a). Thus, a better performance within the whole troposphere is expected for RR lidar systems operated at 355 nm. Furthermore, the use of a wavelength in the UV has several other advantages. Firstly, the molecular backscatter is proportional to λ^{-4} . Therefore, the backscatter due to molecules is about 5 times higher at 355 nm compared to 532 nm. Secondly, the daytime measurement capability is enhanced as the solar background at 355 nm is lower because much of the light in the UV is attenuated by molecular extinction. Finally, 355 nm can become eye-safe for ranges beyond a few hundred meters from the lidar (see Sect. 4.2.1).

Behrendt et al. (2004b) used experimental data acquired with a primary wavelength of 532 nm to simulate the performance of RR temperature measurements with a primary wavelength of 355 nm. It was shown that a measurement time of just 40 s and 400 m range resolution will yield uncertainties of less than 1 K within 3 km above ground considering a laser power of 15 W and a telescope with primary mirror diameter of 40 cm. The accuracy of such a temperature lidar was expected to be high enough to allow 3-dimensional mapping of the temperature field in the PBL and lower troposphere.

The UHOH RR lidar is equipped with a scanner which benefits from sliding contacts that allow a non-stop movement. The same type of scanner is used in the Raman-shifted Eye-safe Aerosol Lidar (REAL) (Mayor and Spuler, 2004; Spuler and Mayor, 2005). Other scanning Raman lidar systems, e.g., at IfT (Althausen et al., 2000) and NASA GSFC (Whiteman et al., 2006), have been made available for temperature measurements just recently. These systems were used for the measurement of slant profiles in principle. The UHOH RR lidar showed to be capable of measuring temperature fields in an elevation scan mode (Radlach et al., 2008a,b).

A different lidar technique for tropospheric temperature profiling, the DIAL (differential absorption lidar) technique, was suggested by Mason (1975). The DIAL principle is based on emitting two consecutive laser pulses with different wavelengths. One wavelength is tuned to the absorption line of the gas of interest (on-line) and the other one is tuned to a region of lower absorption (off-line) which most suitably is very close to the on-line wavelength, so that the optical properties of the atmosphere are otherwise the same. The only attempt to measure temperature using DIAL was presented by Theopold and Bösenberg (1993). For these measurements, the temperature dependency of the absorption coefficient of O₂ in the near infrared was used. Systematic errors of up to 10 K for a 30 minutes measurement period were observed at a height of 1 km above ground which were too large for practical use. The transmitter and receiver development is challenging due to the height- and temperature-dependent width of the absorption line. Wulfmeyer (1998) presented a narrow-band transmitter concept which was expected to allow DIAL temperature measurements with uncertainties of less than 1 K throughout the troposphere. Nevertheless, no further attempts were published so

far.

The only lidar besides RR lidar by which tropospheric temperature measurements with reasonable results could be achieved so far is HSRL (high spectral resolution lidar) (Eloranta, 2005). The HSRL ratio technique resolves the temperature dependent width of the Cabannes line (more precisely, of the Brillouin band) which is Doppler broadened (Schwiesow and Lading, 1981; Shimizu et al., 1983). An important part in the application of HSRL for temperature profiling is the suppression of scattering due to aerosols and cloud particles (Mie scattering). This was achieved by the use of absorption cells like atomic blocking filters (Shimizu et al., 1983) or iodine vapor filters (Hair et al., 2001) which were tuned to the laser wavelength by adjusting the temperature of the cell. Two filters of different width extract the molecular backscatter while suppressing the Mie-scattered light. The ratio of the signals is a function of atmospheric temperature. For calculating the atmospheric temperature, the pressure at a certain range has to be known. From this height onwards temperature follows from the ratio of the two molecular signals. The profiles of air pressure and density can be calculated additionally by an iterative process assuming hydrostatic equilibrium.

For a 1-h measurement interval and 300 m range resolution a temperature measurement up to 15 km with resulting temperature uncertainties of more than 5 K was presented (Hair et al., 2001). Deficiencies in the system stability led to an offset of up to 10 K with respect to the temperature profile of a radiosonde using an injection-seeded Nd:YAG laser with a primary wavelength of 532 nm.

Just recently, a HSRL was developed that makes use of Fabry-Perot etalons to extract two molecular signals and one Mie signal (Hua et al., 2005a). The molecular signals are detected at two positions on one wing of the Cabannes line (Filter 1: ≈ 0.42 pm apart the laser wavelength, filter width (full width at half maximum, FWHM) ≈ 0.12 pm, transmission of 60%; Filter 2: ≈ 1.47 pm apart the laser wavelength, filter width (FWHM) ≈ 0.25 pm, transmission of 80%). The laser emits light at the frequency tripled wavelength of Nd:YAG which is frequency stabilized by an injection-seeder. A feedback loop was installed which reduced wavelength drifts of the laser.

Temperature profiles up to 4 km AGL with uncertainties of up to 2 K were presented acquiring data for 12 minutes with 60 m range resolution (Hua et al., 2005b). Despite the narrow-band detection, a daytime measurement showed uncertainties of up to 3 K for a similar measurement interval and 180 m range resolution. The system performance was limited by Mie scattering (Hua et al., 2005b).

Compared to the RR technique, HSRL poses much higher demands with respect to the stability of the system and the high rejection of the Mie scattering. In principle HSRL is capable of mapping the temperature field during day- and nighttime due to the narrow-band detection and the strong signals that can be extracted from the Cabannes line. Nevertheless, the stability of the system over several hours is limited.

RASS (radio acoustic sounding system) is an active remote sensing technique which is based on the detection of a density wave created by an acoustic pulse sent into the atmosphere (North et al., 1973). The temperature information is derived from the temperature dependency of the speed of sound. Such systems usually are combined with a radar (radio detection and ranging) or a sodar (sound detection and ranging).

This allows the simultaneous measurement of the wind velocity which can be used to correct the acoustic velocity measurement for air motion (Angevine et al., 1993b). Temperature profiles measured within 30 s and a range resolution of 100 m yielded measurement uncertainties of about 0.5 K up to 1000 m AGL (Angevine and Ecklund, 1994). Additional errors due to turbulence in the atmosphere have a contribution of about 0.1 K to the temperature measurement. In combination with wind measurements also heat-flux measurements can be performed (Angevine et al., 1993a). The range of RASS is restricted to the lower troposphere because of acoustical absorption. Variations in the atmospheric water vapor field lead to measurement inaccuracies due to variations of the refraction index of air. This error can be reduced by a correction with an independent measurement of the vertical humidity distribution (Westwater et al., 1999). Very large systems like the MU (middle and upper atmosphere) radar at RASC are capable of measuring temperature throughout the whole troposphere, e.g., within 30 minutes and a range resolution of 300 m yielding temperature errors of less than about 1 K (Onishi et al., 2002). Due to the noise that is produced by RASS, the deployment is restricted to non-populated areas.

Infrared and microwave radiometry are passive remote sensing techniques to retrieve temperature profiles. The principle of radiometric profiling is based on the measurement of radiation (brightness temperatures) generated at different atmospheric levels. The principal source of thermal radiation and absorption that is used for microwave temperature retrievals is oxygen. Modern microwave radiometers use up to 9 channels, mapping brightness temperatures in the 50–60 GHz frequency range (Löhnert et al., 2004). The radiometer accuracy is limited by bias errors due to the calibration and long-term receiver gain drifts accounting for an error of about 1 K (Crewell et al., 2001).

For a physically consistent retrieval algorithm, a forward model is applied which calculates brightness temperatures at the frequencies of the radiometer from a given atmospheric state. The atmospheric state usually is given by a numerical weather prediction model output (Cimini et al., 2006; Löhnert et al., 2007b) or by radiosonde profiles (Knappe et al., 2008). For the calculation of brightness temperatures from the atmospheric state, a gas absorption model is assumed introducing retrieval uncertainties of up to 1–2 K (Cimini et al., 2006). An inversion algorithm is used to estimate the atmospheric state from the radiometer measurements. The inversion yields non-unique solutions because the observations are affected by measurement errors. In order to restrict the number of possible solutions, a priori information and critical assumptions on the radiometer measurement errors are required. A suitable a priori information is given by the closest radiosonde observation (Löhnert et al., 2004) available. One dimensional variational assimilation techniques (Cimini et al., 2006; Löhnert et al., 2004, 2007b) are used to interpolate between radiometer measurements and a priori data. The temperature measurement accuracy is described by the rms (root-mean-square) deviation of the radiometer retrieval from a radiosonde or, if available, a radiosonde climatology.

Multi-channel radiometric profilers that are available commercially today retrieve temperature with rms errors of better than 1.5 K up to 3 km altitude (Cimini et al., 2006).

The vertical resolution decreases from ground to 3 km linearly from 250 m to 1 km. Above 3 km height, the retrieval accuracy and resolution degrade rapidly due to the low sensitivity of the radiometer channels. The minimum temporal resolution depends on the time the microwave radiometer takes to measure the brightness temperatures in each channel. For vertical temperature retrievals this is 1 s while the data is integrated for, e.g., 1 minute to 15 minutes for retrievals up to 2 km AGL and resulting measurement errors of about 1 K (Pospichal and Crewell, 2007; Knuppe et al., 2008). Longer integration times of, e.g., 4 hours allow retrievals up to 10 km AGL with rms errors of about 1 K (Löhnert et al., 2004).

The structure of inversion layers at the top of the PBL as well as in the free troposphere can not be resolved in detail by microwave radiometer due to the decreasing vertical resolution yielding temperature differences of several Kelvins (Ware et al., 2003; Knuppe et al., 2008) compared to radiosondes. Comparisons between microwave radiometer and tower measurements, with 10 minutes temporal average covering 13 days (in total 1455 cases), yielded rms error of about 0.6 K at 100 m AGL Löhnert et al. (2007b). Nevertheless, rms errors of up to 2 K were observed as well for several individual cases. During variable cloud conditions, the observed brightness temperatures can vary by several Kelvins. This reduces the retrieval accuracy significantly (Ware et al., 2003). Thus, the height and the composition (water and/or ice) of the clouds have to be determined with additional instrumentation, e.g., by a combination of cloud radar and ceilometer, which needs to be included in the inversion algorithm for an improved retrieval (Löhnert et al., 2007a,b).

The improvement of the resolution in the first few hundred meters AGL by measuring brightness temperatures at different elevation angles using scanning radiometric profilers is limited because the retrieval algorithm assumes homogenous stratification in the atmosphere (Cimini et al., 2006) which is — strictly speaking — only justified in homogeneous terrain at night. This assumption can easily yield retrieval errors, also due to the non-applicability of existing gas absorption models as shown in Cimini et al. (2006) and Löhnert et al. (2007b).

AERI (atmospheric emitted radiance interferometer) (Revercomb et al., 2003) is an infrared radiometer producing radiances in the 3–20- μm region. The source that is used for infrared temperature retrievals is carbon dioxide. AERI data are limited to altitudes below 3 km height due to the strength of the infrared signal at the surface (Feltz et al., 2003). AERI performs a self calibration every 10 minutes which accounts for temperature drifts of the system. An inversion algorithm uses a combination of statistical climatological, satellite, and numerical weather prediction model data. The vertical resolution of AERI degrades from 100 m near the surface to 250 m at 3 km altitude while the rms accuracy is about 1 K. The temporal resolution of AERI is restricted by the time the system produces radiances at one-wavenumber resolution from 3 to 20 μm which takes about 10 minutes. During cloudy conditions, retrievals are limited up to the cloud base.

Satellite-based radiometer (Qu et al., 2006) like, e.g., AIRS (Atmospheric Infrared Sounder), IASI (Infrared Atmospheric Sounding Interferometer) and ATMS (Advanced Technology Microwave Sounder) cover only the stratosphere and upper troposphere.

They are limited by a relatively coarse vertical resolution and by the presence of optically thick clouds and, therefore, are not suitable for high resolved temperature measurements in the troposphere.

Chapter 4

System setup

4.1 Filter optimization

This chapter provides an overview of the simulations that were performed to reach the optimal parameters for the narrow-band interference filters used to extract the signals out of the anti-Stokes branch of the pure RR spectrum. The concept of the simulations is explained in Sect. 4.1.1 followed by the results in Section 4.1.2. The curves of the manufactured filters were used to calculate the optimum setup for daytime temperature measurements in the lower troposphere. Section 4.1.3 concludes the findings of the simulations and compares the shape of the different filter curves used for the calculations.

4.1.1 Basic concept

Detailed simulations were performed for investigating most suitable filter parameters to extract the RR signals out of the backscattered light. In the past, similar studies were carried out to quantify, e.g., systematic influences on the calibration function (Nedeljkovic et al., 1993) or to determine best performance of the filters for stratospheric (Behrendt, 2000) temperature measurements. In contrast, the simulations performed within this thesis aim at optimum performance in the troposphere with special emphasis on the lower troposphere and in the presence of a daylight background. Furthermore, a sophisticated analytical function was used to approximate the shape of multi-cavity interference filters (see Appendix A.1).

The statistical temperature uncertainty ΔT was calculated for different central wavelengths (CWLs) and filter widths (FWHM) $\Delta\lambda_{\text{FWHM}}$ at different atmospheric temperatures T . For the calculations, the RR lines of N_2 and O_2 were taken into account. The ratio Q of the pure RR signals P_{RR1} and P_{RR2} is a measure of temperature. If system efficiency, overlap function and atmospheric transmission are equal for both signals, it gives

$$Q = \frac{\sum_{i=\text{O}_2, \text{N}_2} \sum_{J_i} \tau_{\text{RR1}}(J_i) \beta_i^{\text{RR}}(J_i)}{\sum_{i=\text{O}_2, \text{N}_2} \sum_{J_i} \tau_{\text{RR2}}(J_i) \beta_i^{\text{RR}}(J_i)}, \quad (4.1.1)$$

with τ_{RR1} and τ_{RR2} the filter transmission at the wavelength of the RR line J_i for the corresponding channel and the RR backscatter coefficient β_i^{RR} for the corresponding molecule i .

The 1- σ statistical temperature uncertainty is calculated with

$$\Delta T = \frac{\partial T}{\partial Q} \Delta Q. \quad (4.1.2)$$

The uncertainty of Q applying error propagation is

$$\begin{aligned} \Delta Q &= \sqrt{\left(\frac{\partial Q}{\partial P_{\text{RR1}}} \Delta P_{\text{RR1}}\right)^2 + \left(\frac{\partial Q}{\partial P_{\text{RR2}}} \Delta P_{\text{RR2}}\right)^2} \\ &= Q \sqrt{\left(\frac{\Delta P_{\text{RR1}}}{P_{\text{RR1}}}\right)^2 + \left(\frac{\Delta P_{\text{RR2}}}{P_{\text{RR2}}}\right)^2}. \end{aligned} \quad (4.1.3)$$

The lidar signals were simulated according to Eq. (2.4.1) and are thus available in the quantity of photon counts. Therefore, the statistical uncertainty ΔP is based on Poisson statistic and calculated with

$$\Delta P = \sqrt{P}. \quad (4.1.4)$$

The background corrected signal P results in

$$P = P' - P_{\text{B}}, \quad (4.1.5)$$

with P_{B} being the background signal and P' the measured signal. Applying Eqs. (4.1.4) and (4.1.5) to Eq. (4.1.3) yields

$$\Delta Q = Q \sqrt{\frac{P_{\text{RR1}} + 2P_{\text{B1}}}{P_{\text{RR1}}^2} + \frac{P_{\text{RR2}} + 2P_{\text{B2}}}{P_{\text{RR2}}^2}}. \quad (4.1.6)$$

For investigating statistical temperature uncertainties in dependence on the filter width and CWL, the differential quotient in Eq. (4.1.2) can be approximated by means of the slope of $Q(T)$. Thus, ΔT can then be calculated with (Behrendt et al., 2004a)

$$\Delta T \approx \frac{(T_1 - T_2)}{(Q_1 - Q_2)} Q \sqrt{\frac{P_{\text{RR1}} + 2P_{\text{B1}}}{P_{\text{RR1}}^2} + \frac{P_{\text{RR2}} + 2P_{\text{B2}}}{P_{\text{RR2}}^2}}. \quad (4.1.7)$$

As illustrated in Fig. 4.1, the filters central wavelengths λ_{CWL1} and λ_{CWL2} were changed within a defined range. At each position the temperature uncertainty was calculated by Eq. (4.1.7). The uncertainties are smallest for high intensities of the signals P_{RR1} and P_{RR2} and small differential quotient $\partial T/\partial Q$. Small $\partial T/\partial Q$ is equivalent to high temperature sensitivity of the ratio Q . The single RR lines show high temperature dependencies for the higher rotational quantum states that on the other hand result in lower signal intensities. Thus, a trade-off has to be found at which both the temperature sensitivity is maximum and the signal intensity is high, in order to find a global minimum of the temperature uncertainty ΔT . Figure 4.2 shows the two corresponding signals P_{RR1} and P_{RR2} and their ratio plotted versus temperature.

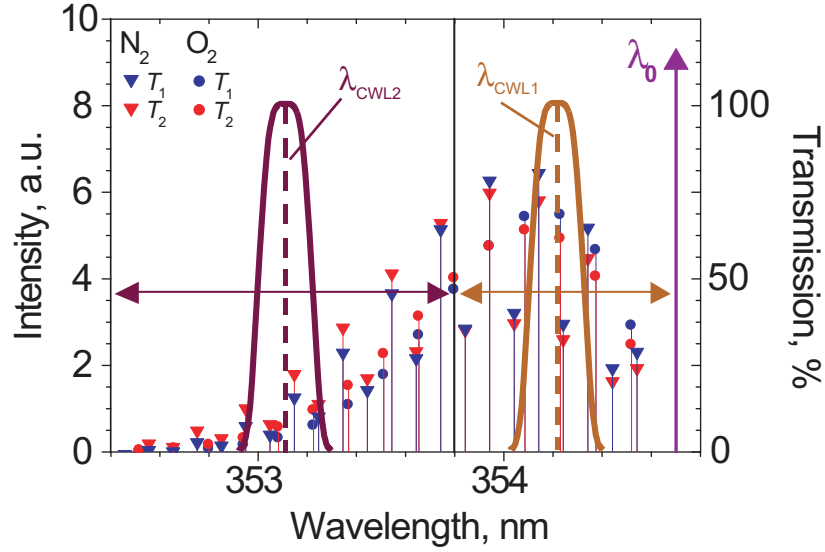


Figure 4.1: Anti-Stokes branch of the pure RR spectrum of nitrogen and oxygen for temperatures of $T_1 = 300$ K and $T_2 = 250$ K. The transmission curve of two idealized filters with a peak transmission of 100% at the CWL λ_{CWL} and a FWHM of 0.2 nm are overlaid with the spectrum. λ_0 denotes the exciting wavelength of the laser. Horizontal arrows mark the range in which the filters CWL were changed in the simulations.

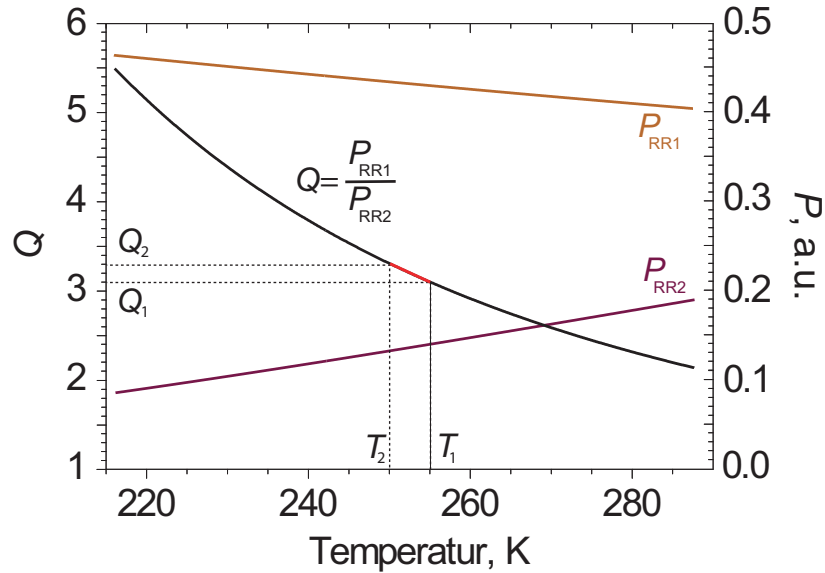


Figure 4.2: Ratio Q of the RR signals P_{RR1} and P_{RR2} plotted versus temperature for the filters shown in Fig. 4.1. Q_1 and Q_2 are the ratios for the two RR signals at temperature T_1 and T_2 , respectively. The red line marks the slope of $Q(T)$ between $T_1 = 250$ K and $T_2 = 255$ K.

For simulating daylight conditions, a background signal per 0.1 nm of the spectrum was added to the signal. This signal was scaled with a factor S relative to the intensity of the strongest RR line in the anti-Stokes branch. The background of each channel was calculated for the respective filter width $\Delta\lambda_{\text{FWHM}}$. The background signal P_{B} was calculated with

$$P_{\text{B}} = S \frac{\Delta\lambda_{\text{FWHM}}}{0.1 \text{ nm}} P_{\text{J}}^{\text{max}}, \quad (4.1.8)$$

with $P_{\text{J}}^{\text{max}}$ being the intensity of the strongest RR line in the anti-Stokes branch and the filter width $\Delta\lambda_{\text{FWHM}}$. A comparison of a measured background during daytime with the simulated background signal of Eq. (4.1.8) is presented in Appendix A.1, Fig. A.3. Hereinafter, $\Delta\lambda_{\text{FWHM1}}$ corresponds to the filter that extracts the RR signals close to the laser wavelength in the channel RR1 and $\Delta\lambda_{\text{FWHM2}}$ to the filter that extracts the RR signals of higher rotational quantum states in the channel RR2.

4.1.2 Filter optimization results

For selecting the most suitable filter parameters in terms of filter width $\Delta\lambda_{\text{FWHM}}$, a Gaussian curve was used in a first step to simulate the extraction of the signals out of the anti-Stokes branch. Besides the main findings, more detailed results can be found in Appendix A.1. The simulations were performed without and with applying a background signal of $S = 1$ (see Eq. (4.1.8)). The requirement of blocking the elastically scattered light up to 7 orders of magnitude (Behrendt, 2005) at λ_{CWL} was also taken into account. The key findings of these calculations confirm that similar filter parameters as shown by Behrendt et al. (2004a), where several RR lines are extracted in each channel, with $\Delta\lambda_{\text{FWHM1}} = 0.3 \text{ nm}$ and $\Delta\lambda_{\text{FWHM2}} = 0.5 \text{ nm}$ are desirable. The signal intensities are increased in such a way that makes a broader pair of filters superior to filters as narrow as $\Delta\lambda_{\text{FWHM}} = 0.05 \text{ nm}$. A broader bandwidth than 0.5 nm showed no further advantages. A pair of filters with $\Delta\lambda_{\text{FWHM1}} = 0.3 \text{ nm}$ and $\Delta\lambda_{\text{FWHM2}} = 0.8 \text{ nm}$ resulted in statistical temperature uncertainties that are decreased by not more than 10% compared to the filter pair of choice with and without a background signal. But, filters broader than those with $\Delta\lambda_{\text{FWHM1}} = 0.3 \text{ nm}$ and $\Delta\lambda_{\text{FWHM2}} = 0.5 \text{ nm}$ do not allow a sufficiently high suppression of the elastic scattered light at the ideal CWL.

In the second step, filter curves with bandwidths of 0.3 nm for the first RR channel and 0.5 nm for the second RR channel were used. The filter curves were provided by Barr Associates, MA, USA, and included a realistic shape and transmission. In an iterative process, the CWL was optimized for low ΔT considering a suppression of at least 7 orders of magnitude of the elastically scattered light in the RR channels (Behrendt, 2000, 2005). The results are detailed in Appendix A.2. Finally, the filters were ordered for an angle of incidence (AOI) of 5° for optimum CWL in order to allow the sequential mounting and wavelength tuning by decreasing or increasing the AOI.

In the last step, simulations were performed to find the optimum setup with the transmission curves of the manufactured filters. The filter curves are shown in Fig. 2.2. A divergent illumination of 1° (full angle) and the overlapping of consecutive filters were taken into account. The calculations for atmospheric temperatures of

$(T_1, T_2) = (300 \text{ K}, 305 \text{ K})$, $(T_1, T_2) = (270 \text{ K}, 275 \text{ K})$ and $(T_1, T_2) = (220 \text{ K}, 225 \text{ K})$ are shown without and with a background signal of $S = 1$ (see Eq. (4.1.8)) in Figs. 4.3a–c and 4.3d–f, respectively. The most suitable combinations for which ΔT becomes smallest are summarized in Table 4.1. The ideal λ_{CWL2} changes towards longer wavelengths for decreasing temperatures. Applying a background signal of $S = 1$, λ_{CWL2} is shifted towards longer wavelengths by approximately 0.3 nm. It is noteworthy that a further increase of the intensity of the background, i.e. $S \gg 1$, has no significant effect on the optimal CWL's.

In conclusion, Figs. 4.3a–c and 4.3d–f show that λ_{CWL1} can be fixed at one position while with λ_{CWL2} the system efficiency can be improved by selecting the filter's AOI, e.g., $\lambda_{\text{CWL2}} = 353.25 \text{ nm}$ yields temperature uncertainties which are decreased by $\approx 30\%$ compared to $\lambda_{\text{CWL2}} = 353.05 \text{ nm}$ at temperatures of 220 K. This can be achieved without any further adjustments of the other channels because RR2 is the last in the sequence (see Sect. 4.2.2).

The position of the filters that were used during the COPS campaign in 2007 are indicated as white rectangles in Figs. 4.3a–c and 4.3d–f. It was necessary to use a smaller λ_{CWL1} of 354.1 nm due to insufficient suppression of the elastic scattered light at the optimum position of 354.25 nm. λ_{CWL2} was chosen as 353.25 nm to minimize uncertainties for daytime measurements. For temperatures of 300 K and 270 K, this led to an increase of statistical temperature uncertainties of 33% and 27%, respectively, without and about 10% with a daylight background of $S = 1$. Despite this enhancement of statistical temperature uncertainties in case of zero background, it should be mentioned that this case characterizes nighttime conditions. Thus, the interpretation should not mislead as ΔT at night is rather small. At lower temperatures of 220 K the uncertainties are increased by about 22%. White diamonds in Figs. 4.3a–f indicate a slightly altered setup which was used during the first test measurements at UHOH (see Chapter 6) to yield high temperature sensitivity at low altitudes (temperatures of $\approx 270\text{--}300 \text{ K}$) at day- and nighttime. Here IF 3 was set to an AOI of 6° . For temperatures of 270–300 K ΔT does not differ much compared to the setup that was used during the COPS campaign assuming a background signal of $S = 1$, whereas ΔT is increased by 50% for the white diamonds for temperatures of 220 K. On the other hand,

Table 4.1: Optimum position for the manufactured filters at different atmospheric temperatures without and with a background ($S = 0$ and $S = 1$, respectively).

Temperature	Background level $S = 0$			Background level $S = 1$		
	CWL1	CWL2	ΔT , a.u.	CWL1	CWL2	ΔT , a.u.
220 K	354.34 nm	353.07 nm	1	354.30 nm	353.33 nm	1
270 K	354.31 nm	352.91 nm	1	354.26 nm	353.20 nm	1
300 K	354.26 nm	352.79 nm	1	354.21 nm	353.08 nm	1

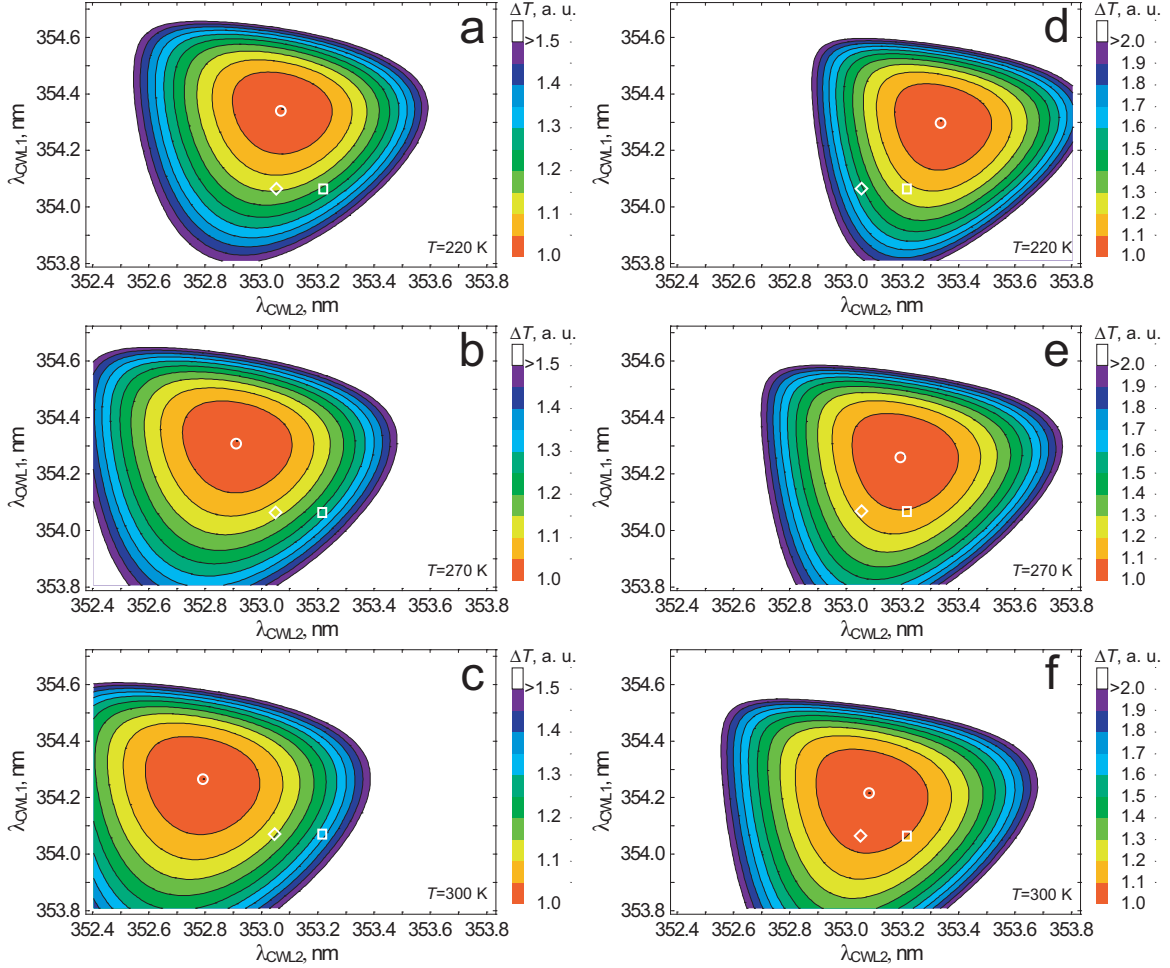


Figure 4.3: Results of the optimization calculations for the parameters of the RR channel filters: Calculated statistical temperature uncertainty ΔT versus filter CWLs λ_{CWL1} and λ_{CWL2} for the filters shown in Fig. 2.2. (a) $(T_1, T_2) = (220 \text{ K}, 225 \text{ K})$, (b) $(T_1, T_2) = (270 \text{ K}, 275 \text{ K})$ and (c) $(T_1, T_2) = (300 \text{ K}, 305 \text{ K})$. (d–f) same as (a–c) but with a background signal of the same intensity as the strongest RR line in the anti-Stokes branch added to the signals. A laser wavelength of 354.7 nm was used for the calculations. Calculation step width was 0.01 nm. Values for ΔT are scaled relatively to the minimum (white circle) of each plot. White rectangles mark the final setup in the polychromator during the COPS campaign. White diamonds show the setup during the first test measurements where IF3 was set to an AOI of 6° which corresponds to $\lambda_{\text{CWL2}} = 353.05 \text{ nm}$. The color scale of ΔT is plotted on the right.

Table 4.2: Temperature uncertainties at different atmospheric temperatures of the two settings as shown in Figs. 4.3 relative to the optimum position of the filters that is shown in Table 4.1.

Setting	Temperature	$\Delta T/\Delta T_{\min}$	
		Background level $S = 0$	Background level $S = 1$
◇	220 K	1.14	1.52
	270 K	1.13	1.18
	300 K	1.15	1.08
□	220 K	1.22	1.23
	270 K	1.27	1.11
	300 K	1.33	1.1

if no background signal is assumed, the COPS setup shows uncertainties that are up to 15% larger than those for the white diamonds. Nevertheless, a smaller AOI for IF3 is better as the signal intensities are increased in the channel RR2 which is beneficial for daytime measurements. The two different settings of the interference filters that were used in the lidar polychromator, together with the temperature uncertainty relative to the optimum filter position according to Figs. 4.3 are summarized in Table 4.2.

4.1.3 Discussion and conclusion

In summary, it can be stated that beneficial filter parameters at λ_0 feature values of $\text{FWHM} > 0.1$ nm. This allows more than one RR line to be extracted in each channel which in turn improves the signal statistics. On the other hand, in case of the filter that extracts RR lines close to λ_0 , the filter width should not exceed 0.3 nm in order to achieve a high suppression at λ_0 and to allow a sufficient wavelength tuning capability for adjusting the CWL to gain a high temperature sensitivity. The requirements for the filter at λ_{CWL2} are not strict, but if the bandwidth is chosen too broad, the daytime performance suffers because the optimum CWL is shifted towards shorter wavelengths, where the single RR lines become weaker due to a smaller backscatter cross section (see Eq. (2.4.3) and Fig. 2.2). The weak RR lines do not contribute to an improved signal statistics.

A general reason to favor filters with $\Delta\lambda_{\text{FWHM}} > 0.05$ nm is that transmission values in the UV for very narrow filters with FWHM of 0.05 nm are feasible with around 15–20% at date (Barr Associates), whereas filters with $\text{FWHM} > 0.3$ nm can be manufactured with a transmission higher than 60% (Radlach et al., 2008a).

Figure 4.4 shows the impact of divergent illumination on a filter with FWHM of 0.05 nm. The effective FWHM is more than 4 times larger and the effective peak transmission is reduced to one quarter assuming a divergence of 1° (full angle) in the polychromator. Whereas for a divergence of 0.4° (full angle), the effective FWHM is

still more than 2 times larger and the effective peak transmission is reduced by 50%. Figures 4.5a,b compare filter curves with FWHM of 0.3 nm and 0.5 nm that were used for the two RR channels during the simulations shown in Appendices A.1, A.2 and in Sect. 4.1.2. The modified Gaussian curve (see Eq. (A.1.1)) that was used to approximate multi-cavity interference filters matches the simulated filter curves quite well. The application of such a Gaussian curve allows a more detailed investigation of suitable filter parameters than possible by a rectangular filter which was used in Behrendt (2000).

The statistical measurement uncertainty for different atmospheric temperatures for the filter pairs used in this thesis and by the Raman lidar of the University of Basilicata, Potenza, Italy (UNIBAS) (these filters were used with the NASA GSFC Scanning Raman Lidar previously) (Di Girolamo et al., 2004) extracting RR signals in the UV from the anti-Stokes branch with filter bandwidths of $\Delta\lambda_{\text{FWHM1}} = 0.2$ nm and $\Delta\lambda_{\text{FWHM2}} = 1.0$ nm at $\lambda_{\text{CWL1}} = 354.3$ nm and $\lambda_{\text{CWL2}} = 352.9$ nm, respectively, are compared in Fig. 4.6. The CWL of the filters applied within this work were optimized in order to achieve low statistical temperature uncertainties during daytime.

If a background signal with scaling factor $S = 1$ is applied, ΔT shows an increase by a factor of up to 2.6–4 for the RR lidar of UNIBAS whereas ΔT is increased by a factor of 2–2.5 for the UHOH system for temperatures from 300–220 K, respectively, compared to the case with zero background ($S = 0$). ΔT increases uniformly continuous for increasing temperatures. The filter pair used by Di Girolamo et al. (2004) shows approximately constant ΔT for the temperature range from 220–300 K taking the background signal into account.

If a higher suppression at $\lambda_{\text{CWL1}} = 354.3$ nm could be achieved by the respective interference filter of the UHOH lidar, ΔT decreases by 20–30% and 10–15% for $S = 0$ and $S = 1$, respectively, over the full temperature range investigated here. Further advancements in manufacturing narrow-band interference filters can be expected to achieve a higher suppression of the elastic scattered light even close to the laser wavelength. If no background signal is present, the statistical temperature uncertainties between the setup used in the UNIBAS (black dotted line) and the UHOH lidar (green dotted line) are quite similar for low atmospheric temperatures ($T \approx 220$ K). For temperatures of 300 K, ΔT is increased by about 20% for the UHOH filter pair. A similar nighttime performance as for the UNIBAS filter setup can be achieved when $\lambda_{\text{CWL2}} = 353.05$ nm is chosen. Considering only the performance of the interference filters, even the shifted CWL (out of the optimum), which shows high elastic signal suppression, results in up to 30% improvement for daytime conditions compared to the previous system at 355 nm of Di Girolamo et al. (2004).

4.2 The scanning rotational Raman lidar of University of Hohenheim

The development of a scanning RR lidar at UHOH was successfully achieved in the framework of this thesis. It is an upgrade of the eye-safe scanning aerosol lidar that was designed in summer 2005 (Pal et al., 2006) for aerosol measurements close to a livestock farm (Pal, 2009; Lammel et al., 2007). To achieve scanning measurements at

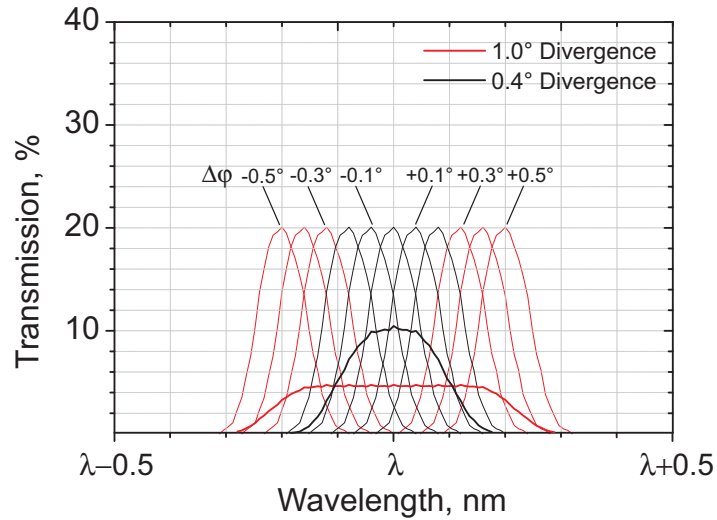


Figure 4.4: Effects of non-parallel illumination onto a filter with $\Delta\lambda_{\text{FWHM}} = 0.05$ nm at $\lambda = 354.35$ nm.

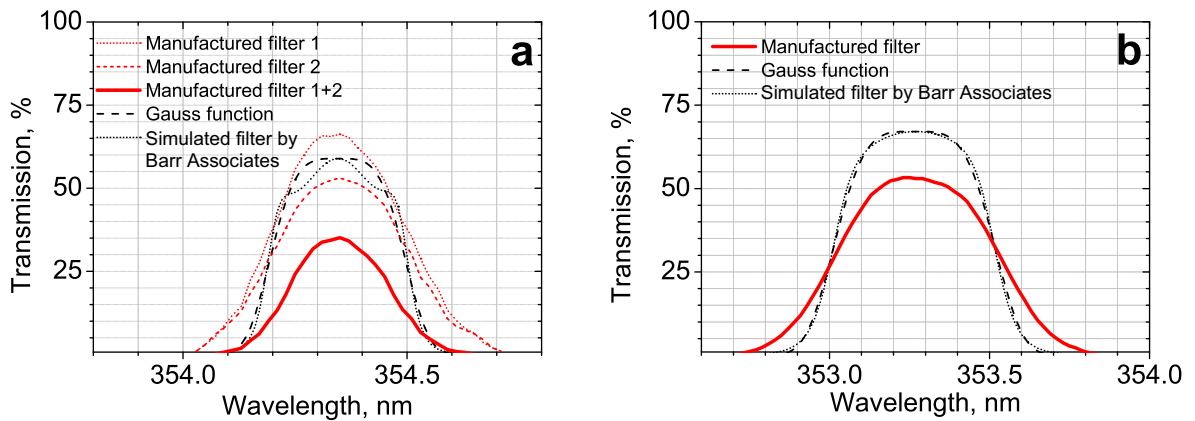


Figure 4.5: Transmission curves of the filters used for the simulations in Appendices. A.1 and B and Section 4.1.2. (a) FWHM of 0.3 nm, CWL of 354.35 nm and (b) FWHM of 0.5 nm, CWL of 353.25 nm. The transmission of the Gauss filters were normalized relatively to the peak transmission of the corresponding simulated filter.

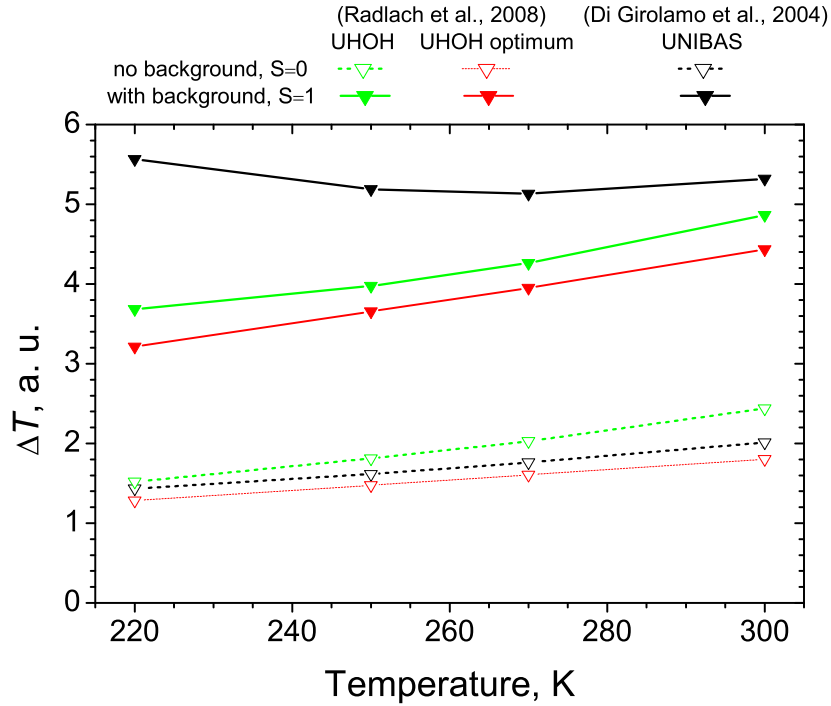


Figure 4.6: Comparison of the interference filters used in the UHOH and the UNIBAS lidar system. The setup “UHOH optimum” includes $\lambda_{\text{CWL1}} = 354.3$ nm. For the UHOH filters the curves from Fig. 2.2 were used and for the UNIBAS filters a Gaussian curve with the transmission, CWL and FWHM as described in Di Girolamo et al. (2004) were used. Statistical temperature uncertainties are shown for different atmospheric temperatures with and without a background level of $S = 1$ and $S = 0$, respectively. Note that in this comparison no parameters regarding the system efficiency or the laser power are included.

any location of interest the lidar was installed in a container that is fixed on a truck.

4.2.1 Transmitter setup

This section gives an overview of the transmitters that were used during 2006 and 2007. The setup of the scanning lidar system is shown schematically in Fig. 4.7. The laser transmitter is a Nd:YAG laser by Spectra-Physics. For the field experiment COPS the injection-seeded Nd:YAG laser GCR 290-50 by Spectra-Physics was used instead of the older model GCR5-30 that was used in 2006. The main difference between both lasers is that the GCR 290-50 is equipped with an injection-seeder which allows single-mode operation. This features a line width of 0.01 cm^{-1} at the fundamental wavelength of Nd:YAG of 1064 nm, whereas the unseeded laser GCR5-30 has a line width of 1 cm^{-1} (Lightwave, 1994). The specifications of both lasers are detailed in Table 4.3. The Nd:YAG lasers emit radiation at 1064 nm. By use of two non-linear crystals that are build into a temperature stabilized box — the harmonic generator

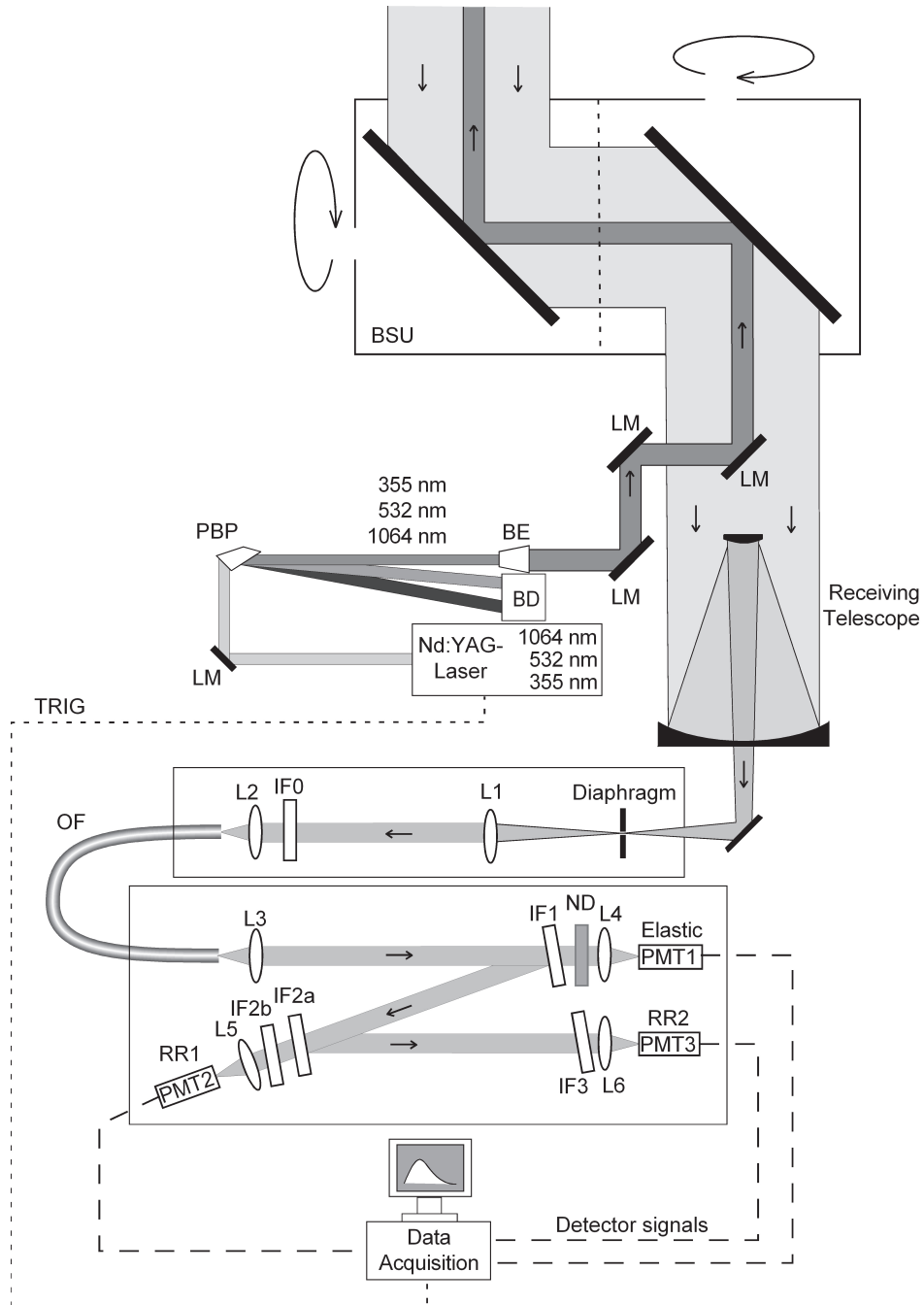


Figure 4.7: Schematic setup of the UHOH scanning RR lidar system. BD: beam dump, BE: beam expander, BSU: Scanner (beam steering unit), IF0–IF3: interference filters, L1–L6: lenses, LM: laser mirror, ND: neutral density filter, OF: optical fiber, PBP: Pellin-Broca prism, PMT1–PMT3: photomultiplier tubes, TRIG: trigger signal.

Table 4.3: Laser specifications. Everything but the pulse energy and divergence (except for GCR 290-50) is taken from the manufacturer manuals.

Laser Type	Spectra-Physics GCR5-30 Flash-lamp-pumped frequency tripled Nd:YAG laser	Spectra-Physics GCR 290-50 Flash-lamp-pumped frequency tripled Nd:YAG laser with injection-seeder
Wavelengths	1064/532/355	1064/532/355
Pulse repetition rate	30 Hz	50 Hz
Pulse energy at 355 nm	≈ 300 mJ	≈ 200 mJ
Mean power at 355 nm	≈ 9 W	≈ 10 W
Pulse duration	5 ns	5 ns
Spectral line width	≤ 1 cm ⁻¹	0.01 cm ⁻¹
Divergence	<1.4 mrad	<0.5 mrad
Beam profile	circular	circular
Beam diameter	10 mm	10 mm

— the fundamental frequency is doubled and tripled. This additionally leads to the simultaneous emission at 532 nm and 355 nm. The harmonic generator crystals are tunable with respect to their angle relative to the laser beam propagation and thus allow to set the output power at the three wavelengths. The output at 355 nm is optimized for a maximum output power being in case of the GCR5-30 about 9 W (30 Hz, 300 mJ pulse energy) and in case of the GCR 290-50 about 10 W (50 Hz, 200 mJ pulse energy).

The laser radiation at 355 nm is separated from the radiation at 532 nm and 1064 nm with a Pellin-Broca prism. The latter two wavelengths are eliminated in a beam dump. The light at 355 nm on the laser output is p-polarized. This ensures an almost lossless diffraction at the incident and the exit surface of the Pellin-Broca prism used at Brewster's angle. Special care has to be taken to make the system eye-safe because it is equipped with a scanner and, thus, allows the operator to point the beam into any direction of interest. According to regulations for eye-safety of the German Employer's Liability Insurance Association (Präventionsrecht-digital GbR), the energy density limit is 47 J m⁻² for a radiation source with pulse length of 5 ns at 355 nm. Figure 4.8 shows the energy density at a given beam diameter for both lasers. According to this figure, the necessary beam diameter has to be at least 14 cm in order to protect the eye's retina. For the UHOH lidar, the laser beam is expanded by a factor of 6.5. The beam divergence for the expanded beam of the GCR5-30 laser is about 0.2 mrad and eye-safety is reached in a distance of 400 m from the lidar telescope. The lower beam divergence of about 0.1 mrad for the GCR 290-50 yields eye-safety in a distance of 600 m. In these calculations the hot spots of the top-head beam profile, which was mapped using a CCD camera, were taken into account.

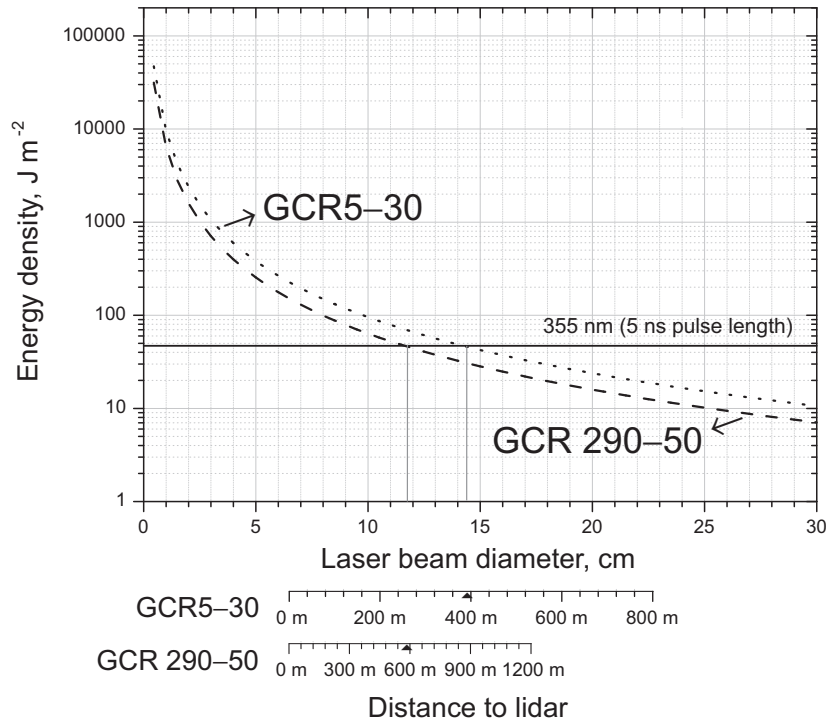


Figure 4.8: Energy density plot for different pulse energies at a laser wavelength of 355 nm with a pulse length of 5 ns. The radiation is eye-safe for an energy density of less than 47 J m^{-2} . The distance to the lidar where the beam becomes eye-safe is shown on the axes below for the two lasers GCR5-30 and GCR 290-50 that were used.

4.2.2 Receiver setup

The UHOH RR lidar uses a coaxial setup. The outgoing laser beam and the receiver have the same optical axis as schematically depicted in Fig. 4.7. The roof-mounted beam steering unit was manufactured by the workshop of the National Center for Atmospheric Research in Boulder, CO, USA. It benefits from sliding contacts that allow a non-stop movement of the scanner. The same type of scanner is used in the Raman-shifted Eye-safe Aerosol Lidar (REAL) (Mayor and Spuler, 2004; Spuler and Mayor, 2005). The two large octahedral mirrors of the scanner unit, which have a size of $61 \times 43 \text{ cm}$ ($24 \times 17 \text{ inches}$), point the laser beam into any direction of interest. The backscattered light from the atmosphere passes the same scanner mirrors and is then directed towards a Ritchey-Chretien type telescope. This telescope has a primary mirror diameter of 40 cm and an effective focal length of about 4 m. An adjustable field stop is positioned in the focus of the telescope, followed by a lens that collimates the light and a broadband interference filter IF0 with a FWHM of 8 nm. This filter is used for blocking the atmospheric background by a factor of 10^{-5} outside the transmission band while the elastic and the RR signals are transmitted. After this filter the light is focussed into an optical fiber that guides it into the polychromator. A lens collimates the light before it is separated into the channels. The polychromator has a cascade

Table 4.4: Filter parameters.

2006	IF0	IF1	IF2a	IF2b	IF3
AOI, deg	0.0	5.6	6.5	6.5	5.0
CWL, nm	353.65	354.66	354.05	354.05	353.25
FWHM, nm	8.5	0.29	0.32	0.33	0.52
Peak transmission	0.56	0.62	0.53	0.65	0.52
Reflectivity at 354.66 nm		< 0.1			
Transmission at 354.66 nm	0.56	0.62	< 10^{-3}	< 10^{-3}	< 10^{-6}
2007					
AOI, deg	0.0	5.3	6.3	6.3	5.0
CWL, nm	353.65	354.73	354.1	354.1	353.25

structure which was first introduced by Behrendt (2000). This setup makes use of narrow-band multi-cavity interference filters that are used at a small AOI which has some important advantages to conventional setups. First, the CWL of each filter can be tuned by selecting the tilting angle. Second, a high efficiency is gained when separating the received light by a sequential mount of the channels. Finally, a very high suppression of at least 7 orders of magnitude of the elastically scattered light in the RR channels can be achieved. The transmission band of IF2 is very close to the laser wavelength. Thus, two filters are used for the first RR channel. As shown in Table 2, one order of magnitude of the suppression of the elastically scattered light is already obtained at IF1 which reflects less than 10% at the laser wavelength. The filter parameters used in combination with the Spectra-Physics GCR5-30 laser in 2006 and with the GCR 290-50 in 2007 are summarized in Table 4.4. The interference filters, as used in 2007, are shown in Fig. 2.2 together with the RR spectrum of N₂ and O₂. The dependence of the filter's CWL versus the AOI is shown in Fig. 4.9.

The AOI of IF1 for which the transmission at the laser wavelength of the GCR5-30 is maximum was measured experimentally in 2006 and resulted an AOI of 5.6° (corresponds to $\lambda_0 = 354.66$ nm). The wavelength of the GCR 290-50 was measured with a pulsed wavemeter which was not available earlier. This measurement resulted in $\lambda_0 = 354.73$ nm (AOI = 5.3° of IF1).

The data acquisition is performed with a 3-channel transient recorder obtained from Licel GmbH, Germany. The data of each channel are recorded as three signals: with 3.75 m resolution up to a range of 15.36 km (4096 range bins) in analog and photon-counting mode and simultaneously in photon-counting mode with 37.5 m resolution up to a range of 76.8 km (2048 range bins). This concept allows for using the analog signals in the near range where the photon-counting signals are saturated and the photon-counting signals in the far range where the signal-to-noise ratio (SNR) of the analog signal is low. During post-processing it is possible to combine the analog and the photon-counting data to get a single profile (Licel GmbH; Behrendt et al., 2004a;

Table 4.5: Technical data of the receiver part.

Telescope	Geometry	Ritchey-Chretien type
	Primary mirror diameter	415 mm, parabolic
	Secondary mirror diameter	150 mm, parabolic
	Focal length	4082 mm
	Field stop diameter	3 mm (selectable)
	Field of view	0.75 mrad
Detectors	Model	Hamamatsu
	Type	R7400-U02 (elastic channel) R1924P (RR channels)
Data acquisition system	Model	3-channel Licel Transient recorder
	Type (before summer 2007)	TR40-40 (a+p) + opt-PR 2.5-20 (p)
	Repetition Frequency	1.2 kHz
	Type (since summer 2007)	TR40-80 (a+p) + opt-PR 2.5-20 (p)
	Repetition Frequency	0.6 kHz
	Height resolution (max)	3.75 m (TR40-40/80) 37.5 m (opt-PR 2.5-20)
	Memory depth	4096/8192 (TR40-40/80) 2048 (opt-PR 2.5-20)

Whiteman et al., 2006; Pety and Turner, 2006). The memory of the transient recorder was doubled for all three channels in 2007 (8192 range bins). This allowed to acquire the data during the COPS campaign in higher resolution up to a range of 30.72 km. The technical details of the components of the receiver part are given in Table 4.5.

The system performance for all measurements carried out 2006 suffered because of a degradation of the protected silver coating, that was applied to the three consecutive laser bending mirrors and the two scanner mirrors (see Fig. 4.7). The outgoing laser power was measured after each of the three bending mirrors and the last scanner mirror with the pyroelectric sensor LM-P10i of Coherent GmbH, Germany. The total efficiency of the transmitting optics was measured to be 30% (Radlach et al., 2008b) in s-polarization. By turning the last scanner mirror by 90°, which sets the pointing direction of the laser beam from vertical to horizontal, the plane of incidence changes with respect to the polarization of the laser beam. Due to the fact that the mirrors showed worse reflectivity for p-polarized light, the total efficiency was decreased to 13%. The product of the effective laser output power, the effective telescope area and an estimation of the system efficiency gives the power-aperture-efficiency product (PAEP).

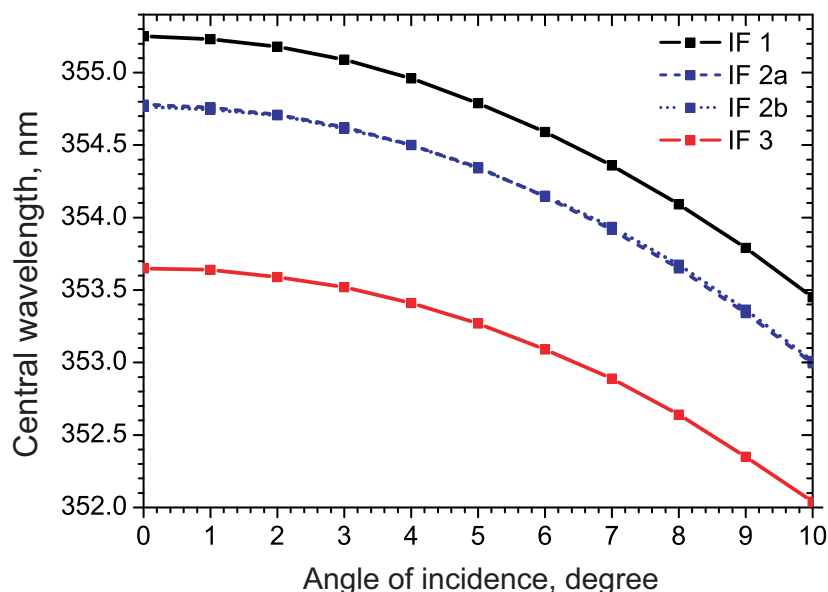


Figure 4.9: CWL versus AOI for the interference filters in Table 4.4. The measurement was performed by Barr.

The PAEP was about 4.5 mW m^{-2} and 1.5 mW m^{-2} if the plane of incidence of the mirrors is perpendicular with respect to the polarization of the laser beam and if the last mirror is turned by 90° , respectively. The PAEP was estimated for the full system including all optical components but the narrow-band interference filters IF1–IF3 which have peak transmissions of 0.62, 0.34 and 0.52 for the elastic, RR1 and RR2 channel, respectively. This shortcoming was overcome after the PRINCE campaign by recoating the two large scanner mirrors as well as the three bending mirrors so that the measurements during COPS in 2007 show a higher performance. An estimation of the PAEP yields 100 mW m^{-2} independent of the movement of the scanner in any direction. Furthermore, losses created by the fiber that was used to couple the backscattered light into the polychromator were removed by taking out the optical fiber (see Fig. 4.7) in mid of July 2007. Thus, an estimation of the PAEP yields approximately 125 mW m^{-2} .

Chapter 5

Data analysis

For a comprehensive understanding of the lidar data it is important to analyze systematic and statistical uncertainties. The latter can be assessed by assuming the photon-counting signals to be Poisson distributed and calculating the $1\text{-}\sigma$ statistical temperature uncertainties with Eq. (4.1.2). Measurements uncertainties of analog data are, e.g., deduced by a spectral analysis of a time series which is discussed in Sect. 8.4. Another option is provided by an algorithm that allows for merging the analog data with the photon-counting data by creating virtual count rates from the analog data (Licel GmbH, 2008; Behrendt et al., 2004a; Whiteman et al., 2006; Pety and Turner, 2006). These count rates can then be used to calculate the $1\text{-}\sigma$ statistical temperature uncertainties with Eq. (4.1.2).

In Section 5.1 a measurement example is presented as well as a description of the lidar calibration. Systematic error sources are discussed in Sect. 5.2.

5.1 Lidar calibration

An example of the measurement obtained on 10 July 2006 between 20:00 and 21:00 UTC is shown in Fig. 5.1. The data were acquired during the measurement campaign PRINCE. The lidar was deployed on top of the mountain Hornisgrinde, Germany, in the Northern Black Forest, at an altitude of 1161 m ASL. The two RR signals P_{RR1} and P_{RR2} are plotted in Fig. 5.1a. Here, the photon-counting signals and the analog signals for the two RR channels were merged in a range between 2 and 3 km AGL. The photon-counting data were affected by dead-time effects in the lowermost 2 km which were corrected prior to the combination of the analog and the photon-counting signals (Licel GmbH). During the COPS campaign, the range where both the analog signals and the dead-time corrected photon-counting signals respond linearly was found at higher altitudes of 3 to 4 km AGL because of higher signal intensities compared to PRINCE. A suitable dead-time correction scheme is found by describing the receiver as a paralyzable system (Behrendt et al., 2002). The measured count rate N therefore yields

$$N = N_c \exp(-N_c \tau) , \quad (5.1.1)$$

with the dead-time corrected count rate N_c and the dead-time τ of the corresponding receiver channel (Evans, 1955). In case of the detectors used for the RR channels RR1 and RR2 the dead-times are $\tau = 5.55$ ns, whereas for the photomultiplier in the elastic channel the dead-time is $\tau = 4.1$ ns. These values were measured by Licel GmbH. The different dead-times are caused by the geometry of the photomultiplier tubes. N_c is calculated by an iterative approach. Eventually, the dead-time corrected

photon-counting signal and the corresponding analog signal can be combined for each channel to achieve a single signal. This ensures the coverage of the lidar signals' full dynamic range. Turning analog signals into virtual count rates allows the application of Eq. (4.1.6) and Eq. (4.1.2) in order to calculate the statistical temperature uncertainties. An algorithm is described in detail by Licel GmbH (2008). If not otherwise mentioned, the RR signals were always treated as described here. The data of the elastic backscatter never required a combination of the analog and photon-counting signals because the high signal intensities yielded a low SNR throughout the whole troposphere.

For the calibration of the lidar, usually a vertical measurement is chosen covering a large temperature range. Solving Eq. (4.1.1) yields the functional relation between temperature T and the ratio Q of the two RR signals. Assuming that exactly one RR line is extracted in each channel the exact solution for the ratio $Q(T, R)$ is

$$Q(T, R) = \exp\left(\frac{A}{T(R)} + B\right). \quad (5.1.2)$$

Inverting Eq. (5.1.2) yields

$$T(R) = \frac{A}{\ln[Q(T, R)] - B}, \quad (5.1.3)$$

with the calibration constants A and B . When the involved temperature range is not too large, Eq. (5.1.2) is also an useful approximation if several RR lines have to be considered in each channel (Arshinov et al., 1983; Di Girolamo et al., 2004; Radlach et al., 2006). An even better approach, however, is to use the higher-order approximation, when several RR lines are extracted in each channel (Behrendt and Reichardt, 2000) which is

$$Q(T, R) = \exp\left(\frac{a'}{T(R)^2} + \frac{b'}{T(R)} + c'\right). \quad (5.1.4)$$

Solving Eq. (5.1.4) for T yields

$$T(R) = \frac{-2a'}{b' - \sqrt{b'^2 - 4a'(c' - \ln[Q(T, R)])}}, \quad (5.1.5)$$

with the calibration constants a' , b' and c' disregarding the physically illogical solution. Besides the functional relation between T and Q , also other attempts were made to yield a more accurate approximation (e.g. by Nedeljkovic et al. (1993)). Nevertheless, for a system that extracts several RR lines in the receiving channels, it was shown that the ansatz in Eq. (5.1.4) is superior (Behrendt, 2000, 2005) which, therefore, should be used when a large temperature range has to be covered (Behrendt and Reichardt, 2000).

The lidar has to be calibrated in order to obtain absolute temperature. A temperature measurement of a reference temperature sounding is used that resembles the lidar measurement in space and time.

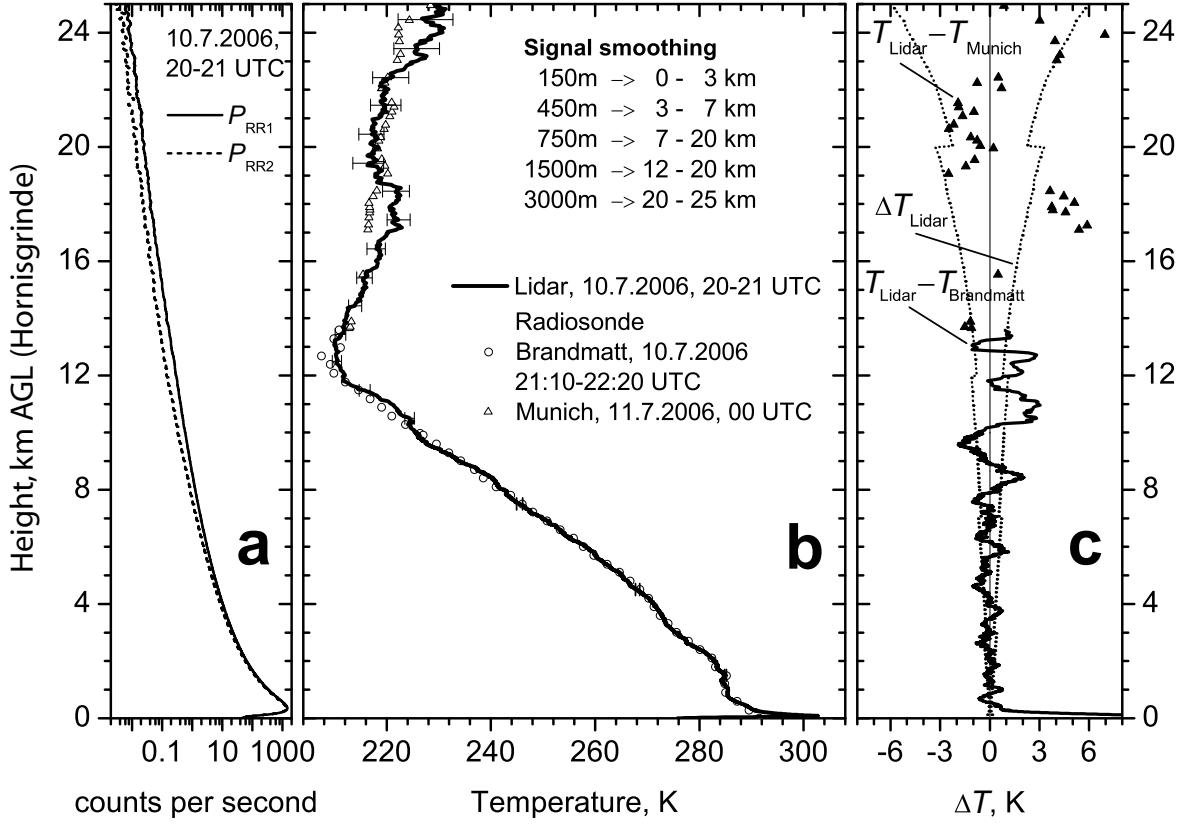


Figure 5.1: Measurement of the UHOH RR lidar on 10 July 2006 on Hornisgrinde (1161 m ASL) in the Northern Black Forrest, Germany. **(a)** Measured signals with a raw resolution of 3.75 m and **(b)** lidar and radiosonde temperature profiles. The lidar signals were smoothed with a moving average of the indicated window lengths. Error bars give the statistical temperature uncertainty. **(c)** Difference between lidar and radiosonde measurements and 1- σ temperature uncertainty of the lidar measurement.

The lidar temperature measurements presented in this thesis were calibrated according to Eq. (5.1.4). To determine the constants a' , b' and c' , the ratio of the two RR signals $Q(T, z)$ was plotted versus the temperature $T(z)$ of the reference sensor for each point in height z . A suitable temporal average as well as an appropriate range resolution was chosen for the calibrations taking into account the requirement of high SNR and good comparability of the lidar data with the reference. The calibration constants were determined by fitting Eq. (5.1.4) to the scatter-plot. The calibration of the data on 10 July 2006 is shown in Fig. 5.2. The Levenberg-Marquardt algorithm (Press et al., 1992) was used to optimize a' , b' and c' by iteratively minimizing

$$\chi^2 = \sum_{i=1}^N \frac{[Q(i) - Q_{Fit}(i)]^2}{[\omega(i)]^2}, \quad \text{with } \omega(i) = \Delta Q(i). \quad (5.1.6)$$

N is the number of data points which are weighted with their statistical uncertainties

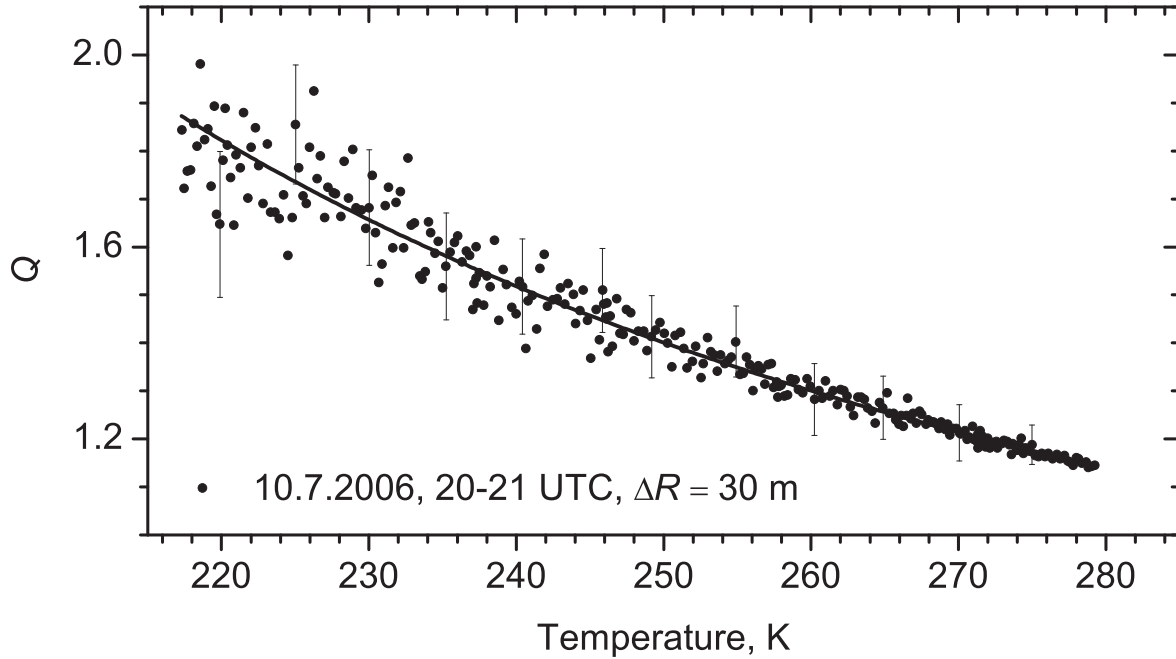


Figure 5.2: Experimental calibration of the RR temperature measurement on 10 July 2006 during the one hour measurement shown in Figs. 5.1. The spatial resolution of the lidar measurement is 30 m. Black dots show the ratio of RR1 and RR2 plotted versus the radiosonde temperature. The solid line is the result applying Eq. (5.1.4) to the scatter plot. Error bars show the statistical uncertainties of Q .

by $\omega(i)$. $\Delta Q(i)$ is calculated by Eq. (4.1.6).

Figure 5.1b shows the temperature profile obtained with lidar and radiosonde launched at Brandmatt(48.61°N, 8.11°E, 675 m ASL), Germany, in a distance of 3 km west of the lidar site. The sonde was used for calibrating the lidar between 2.5 km and 11 km AGL (relative to Hornisgrinde). The 00-UTC sounding from the station of the German Weather Service (DWD) in Munich, Germany (48.25°N, 11.55°E, 489 m ASL, WMO station number: 10868) was used to compare the temperature profile from 12 km to 25 km AGL. The temperature differences to the radiosonde are of similar value like the statistical temperature uncertainties ΔT of the lidar measurement. On that day, a high pressure system predominated over Central Europe providing very stable atmospheric conditions. The horizontal wind speed throughout the troposphere was moderate with 2–9 m/s. The drift of the radiosonde was rather small: Up to 12 km AGL (relative to Hornisgrinde) the sonde was within a radius of 10 km to the lidar site. The statistical temperature uncertainty of the lidar as well as the differences to the temperature measured by the radiosondes are shown in Fig. 5.1c. The $1\text{-}\sigma$ statistical temperature uncertainty of the lidar measurement was less than 1 K throughout the whole troposphere, which extended up to 13 km AGL. Below 600 m, the lidar profile was distorted due to different overlap in the RR channels.

5.2 Analysis of systematic errors

This section quantifies systematic error sources. Section 5.2.1 investigates wavelength drift and the unseeded operation of the laser. Changes of ambient conditions (temperature and humidity) in the container are discussed in Sect. 5.2.2. A theoretical calibration function that applies to the system setup during 2006 (compare Sect. 4.2) is used as the reference for this analysis. Insufficient blocking of elastically scattered light in the Raman channels results in a signal enhancement due to leakage of elastically scattered light. This error source is quantified in Section 5.2.3 by a measurement example.

5.2.1 Stability of calibration function: laser drift

The influence of the radiation source on the calibration includes wavelength drift and random wavelength changes from shot to shot. In principle, the latter one is only observed during unseeded operation. The unseeded laser linewidth is about 1 cm^{-1} at the fundamental wavelength of the Nd:YAG laser (Lightwave, 1994). The wavelength range for unseeded operation at the frequency-tripled wavelength was determined to be about 0.01 nm during an one hour measurement with the pulsed Wavelength Meter WS Ultimate of HighFinesse GmbH, Germany.

Figure 5.3 shows the results of the simulations considering a changing laser wavelength. With respect to the laser wavelength λ_0 of 354.73 nm, the gradual wavelength shift of $\pm 5 \text{ pm}$ is as large as the wavelength range for the unseeded operation of the laser which was used in the UHOH RR lidar (see Table 4.3, Sect. 4.2.1). This shows the lower and upper limits where changes of the calibration function by the laser itself can be theoretically expected. Constant gradual wavelength shifts occur on a much smaller scale between the longitudinal laser modes being strongly linked to temperature changes.

The fundamental wavelength of the laser depends on the Nd:YAG crystal temperature. It was shown that the wavenumber changes linearly by about $0.04 \text{ cm}^{-1} \text{ K}^{-1}$ towards longer wavelengths for increasing temperatures (Marling, 1978). This corresponds to a wavelength shift of about 5 pm/K. For the frequency-tripled wavelength, the shift then is about +0.5 pm/K for increasing temperatures. In fact, the Nd:YAG crystals are internally water cooled keeping the crystals constant at a temperature of about 27 °C. The temperature was measured to increase by 2 K at most during the first 2 hours of the laser operation. This yields a wavelength shift of approximately 1 pm towards longer wavelengths which was also confirmed by measurements with the pulsed wavemeter. The temperature deviations are summarized and shown in Fig. 5.4. Systematic effects of less than 0.1 K are expected due to temperature instabilities of the Nd:YAG laser crystals.

Wavelength shifts during unseeded operation of the laser introduce larger uncertainties of the calibration function. Wavelength measurements showed that the laser kept a constant wavelength over several minutes being stable within 1 pm, before it switched back to a random wavelength change. Gradual shifts of 6–8 pm were observed in

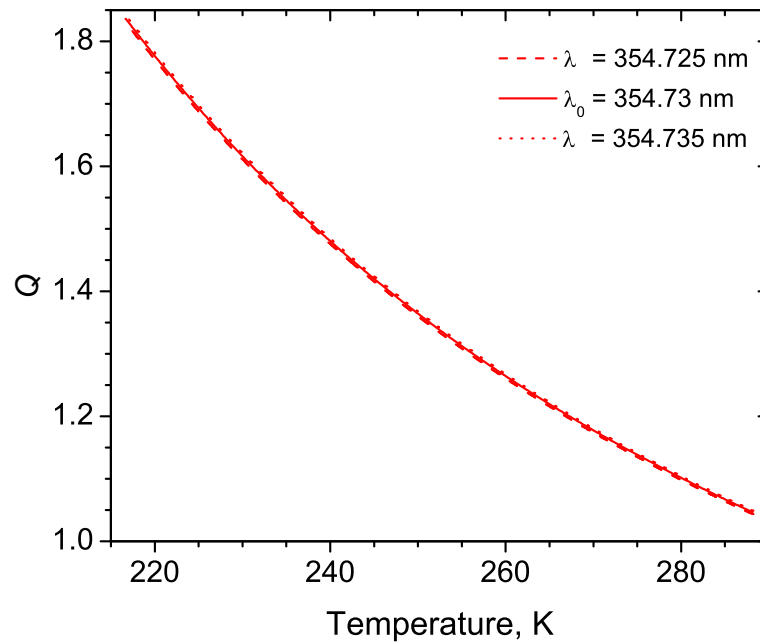


Figure 5.3: Simulation of the calibration function taking into account a wavelength shift of ± 5 pm.

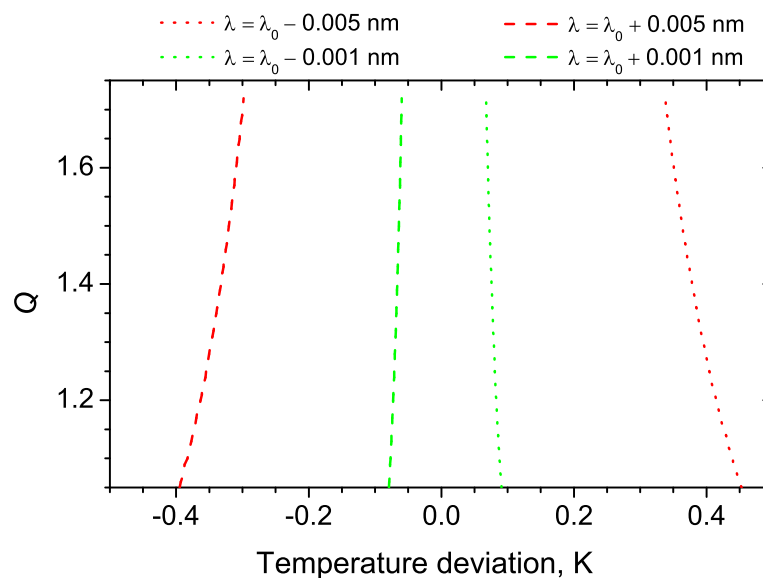


Figure 5.4: Temperature deviation of the calibrations function according to Fig. 5.3 with respect to the laser wavelength of $\lambda_0 = 354.73$ nm. A wavelength change of ± 0.005 nm applies to the unseeded laser. A long term drift of $+0.001$ nm is related to a warm up by 2 K of the laser crystals.

between the “stable” intervals. This is approximately similar to the unseeded linewidth of Nd:YAG which is expected to cause a shift of the calibration function (and as a consequence a shift of the temperature profiles) of up to 1 K.

5.2.2 Stability of calibration function: ambient conditions

Changes of the ambient conditions (temperature and humidity) in the container have an effect on the spectral characteristics of the narrow-band interference filters that are used in the polychromator. The filters used within this work (see Fig. 2.2 and Table 4.4) are specified with a temperature drift of 1.5 pm/K (Barr Associates). The CWL’s are shifted towards longer or shorter wavelengths for a positive or negative temperature change, respectively. The influences on the calibration function are shown in Fig. 5.5 for temperature changes of ± 5 K. Figure 5.6 shows the temperature deviations. Considering a temperature increase by 5 K in the polychromator relative to an initial temperature of 293 K, which is the worst case scenario, the calibration function undergoes a shift of about 3–4 K towards higher temperatures. A negative displacement of 3.5–4.5 K is expected for lower ambient temperatures of 288 K.

Variations of the ambient humidity are also considered to have an effect on the calibration. This was investigated by Behrendt (2000) for an RR lidar operating at a wavelength of 532 nm. Exposure of a film to the atmosphere usually results in a shift of the film characteristics towards longer wavelengths (Macleod, 1986) because of humidity uptake. However, humidity variations are expected to be rather low allowing the ambience to be air-conditioned.

In summary, a systematic error due to a temperature increase of 5 K in the polychromator box are expected to shift the calibration by up to +4 K with respect to an ambient temperature of 20 °C. An unseeded laser, in addition, contributes with a shift of about ± 0.4 K. As a result, this gives a range of about 3.6–4.3 K which the calibration function can be displaced, e.g., within a time interval of several hours while warming occurs. The displacement of the calibration function for a seeded laser is negligible allowing the laser a sufficient time to reach a constant temperature.

The calibration of the UHOH RR lidar was stable within ± 1 K for constant ambient conditions. Parallel displacements of the calibration function of about +5 K occurred on days with strong insolation affecting the spectral characteristics of the interference filters but also the alignment of the system and consequently the overlap due to thermal expansion, e.g.: of the framework, the breadboards and the optical mounts. A constant shift of the calibration function causes a constant shift of the temperature profile. When the offset between individual calibration functions is taken into account, e.g., by comparisons with radiosondes that were available during both campaigns, the lidar still can be calibrated with good accuracy.

For the future it is planned to cover the scanner exit with a quartz plate allowing a better temperature stability in the container even under unfavorable ambient conditions. Furthermore, it is desirable to have an actively temperature stabilized polychromator of better than 0.2 K yielding a stable calibration with a systematic error smaller than 0.1 K.

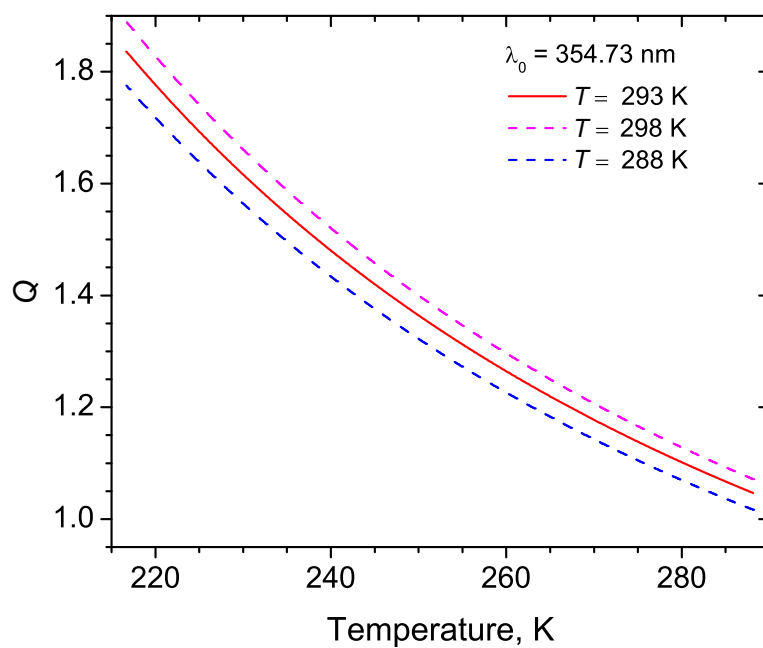


Figure 5.5: Simulation of the calibration function for changing temperatures in the polychromator box of $\Delta T = \pm 5$ K considering an ambient temperature of $T = 20^\circ\text{C}$.

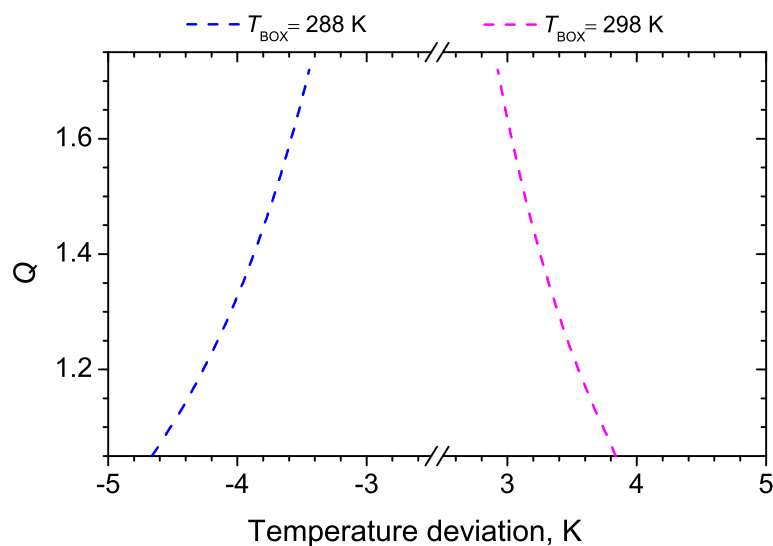


Figure 5.6: Temperature deviation of the calibrations function according to Fig. 5.5.

5.2.3 Leakage of elastic signal into the inelastic channels

An insufficient suppression of the elastically scattered light in the RR channels results in a signal enhancement due to spurious light. The signal of the first RR channel was extracted at a wavelength of 354.1 nm during COPS being close to the wavelength of the laser at 354.73 nm. Thus, the first RR channel is most prone to leakage. In fact, for the interference filters described in Table 4.4 noticeable deviations due to leakage of, e.g., 9.2 K was observed for backscatter ratios of 27 as occurring in optically thick clouds. Figure 5.7a shows the lidar signals measured during a 30 minutes interval on 14 June 2007. During the whole period, a stratus cloud persisted at an altitude between 4 and 4.5 km AGL. The signal of RR1 was slightly enhanced in the presence of this cloud.

Figure 5.7b shows the temperature profiles applying the uncorrected signal and the corrected signal of RR1 for the calculation of T . The backscatter ratio R is given by

$$R = \frac{\beta_{\text{par}} + \beta_{\text{mol}}}{\beta_{\text{mol}}}, \quad (5.2.1)$$

$$R - 1 = \frac{\beta_{\text{par}}}{\beta_{\text{mol}}}, \quad (5.2.2)$$

with β_{par} to be the particle backscatter coefficient (see Eq. (2.4.4)) and β_{mol} the molecular backscatter coefficient. In this thesis R is measured only at the laser wavelength of 355 nm.

The signal of RR1 can be corrected by finding the amount of leakage κ . The corrected signal P_{RR1} is calculated with

$$P_{\text{RR1}} = P_{\text{RR1}}^{\text{leakage}} - P_{\text{elastic}}/\kappa. \quad (5.2.3)$$

Therefore, the ratio Q of the two RR signals reads (Behrendt et al., 2002)

$$Q = \frac{P_{\text{RR1}}^{\text{leakage}} - P_{\text{elastic}}/\kappa}{P_{\text{RR2}}}. \quad (5.2.4)$$

κ is found by computing the temperature for different values of κ . The value for which the profile fits best to a temperature profile of a radiosonde measurement that is close in time and space is then used to correct for elastic signal intrusion. κ is height-independent and constant for the same receiver setup.

This procedure was performed for the lidar temperature profile shown in Fig. 5.7b. The corrected signal P_{RR1} is shown in Fig. 5.7a (solid blue line). Figure 5.7c displays the uncertainty arising from statistical noise of the lidar signals and from the leakage of spurious elastic light.

Stronger backscatter ratios of up to 27 between 4 and 4.7 km AGL marked the cloud region. Backscatter ratios of up to 1.4 indicated aerosol layers below the cloud. The differences between the uncorrected and the corrected temperature profile provide the systematic error for leakage of the elastic signal. It can be seen in Fig. 5.7c that this difference was about 0.2 K for the aerosol layer with $R = 1.4$. Inside the cloud the

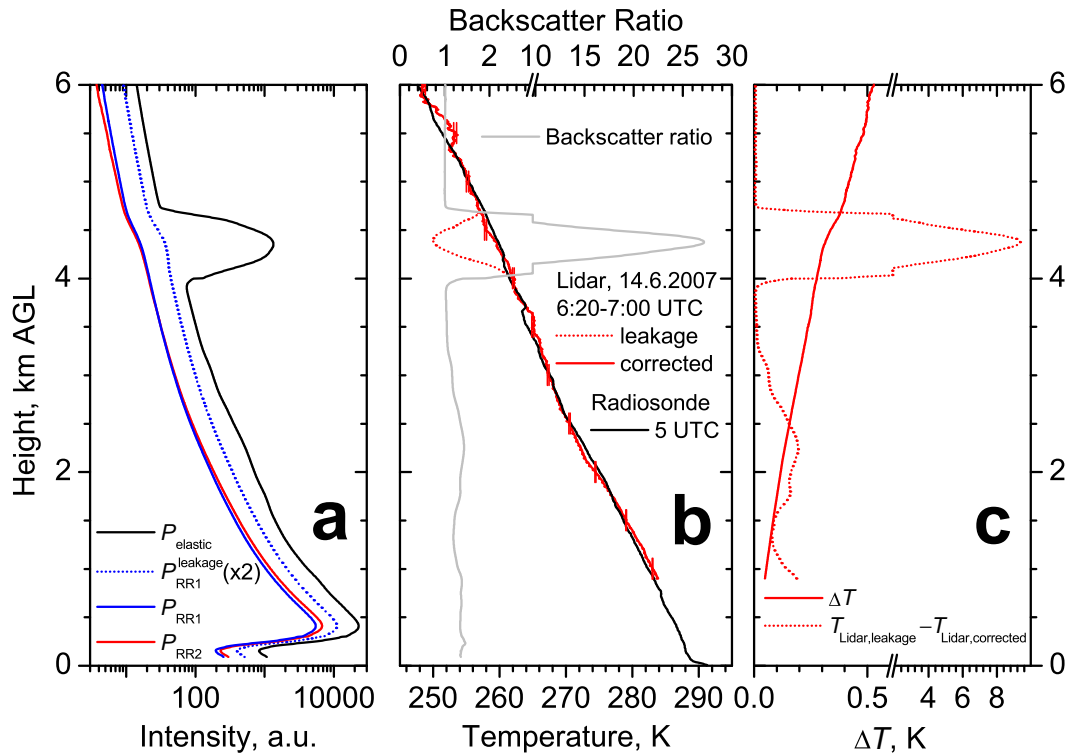


Figure 5.7: (a) Lidar signals of the elastic channel and the two RR channels measured on 14 June 2007 from 6:20–7:00 UTC on Hornisgrinde. RR1 is plotted before and after correcting for elastic signal intrusion. The signals were smoothed with a moving average of 150 m. A cloud deck was present at an altitude between 4 and 5 km AGL which led to a signal enhancement in the first RR channel. (b) Temperature profiles of the lidar calculated using the uncorrected and the corrected signal of RR1 as shown in (a) and the radiosonde launched at 5:00 UTC from Hornisgrinde. Large particle backscatter ratio of up to 27 marked the cloud layer. (c) Temperature differences between the corrected and the uncorrected lidar temperature profile and statistical temperature uncertainty.

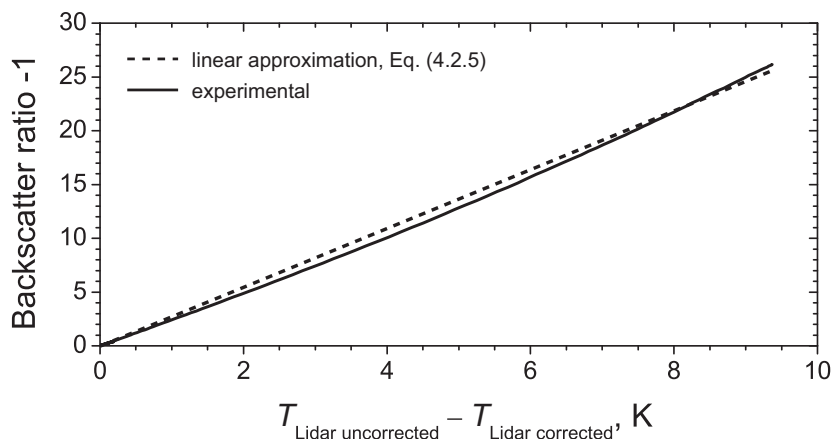


Figure 5.8: Backscatter ratio plotted versus the systematic temperature uncertainties of the lidar data. The result of the linear approximation of Eq. (5.2.5) is shown for comparison.

leakage caused an error of about 9.2 K. The dependence of the systematic temperature uncertainty due to leakage of elastic light on the backscatter ratio is shown in Fig. 5.8. The systematic error is roughly proportional to the amount of leakage and can be calculated with

$$(\Delta T)_{\text{leakage}} \approx -0.37 (R - 1) . \quad (5.2.5)$$

Backscatter ratios of aerosols were observed as large as $R = 1.5$ during the campaigns in 2006 and 2007. Thus, the uncorrected temperature profile within dense aerosol layers appears to be colder by approximately 0.2 K being mostly smaller than the uncertainties caused by statistical noise. An estimation of the precision of this correction scheme results in a statistical error of $(\Delta T)_{\text{leakage}}$ of smaller than 0.04 K, considering the statistical error of the backscatter ratio to be $\Delta R = 0.1$. It should be noted that no external information is necessary for this correction, as R is measured at the same time with the UHOH Raman lidar.

To achieve a sufficient high suppression at the laser wavelength in the first Raman channel, a decrease of the CWL of at least 0.15 nm would be necessary. This in turn increases the statistical temperature uncertainties by more than 25% for both daytime and nighttime measurements. The temperature uncertainty scales with the integration time Δt , the range resolution ΔR , the system efficiency η and the laser power P_0 according to

$$\Delta T \propto \Delta t^{-1/2} \Delta R^{-1/2} \eta^{-1/2} P_0^{-1/2} . \quad (5.2.6)$$

An increase by, e.g., 25% of ΔT , therefore, requires Δt to be longer by a factor of 1.5 or otherwise a decrease of the range resolution by a factor of 1.5 in order to achieve the same statistical uncertainties with the filter position set to a shorter CWL.

Chapter 6

Test measurements at University of Hohenheim

The temperature channels were incorporated into the receiver of the lidar in January 2006. The first temperature measurements were carried out at the campus of UHOH in March 2006. These measurements demonstrated the capability of the UHOH RR lidar to measure temperature in the UV with high accuracy and previously unachieved resolution during daytime. The interference filter IF3 was fixed at an AOI of 6° to yield high temperature sensitivity in low altitudes (temperatures of ≈ 275 K) during day- and nighttime. For the measurement examples presented in the following chapters, the AOI was set to 5° in order to increase the SNR in the presence of a strong daylight background (see Sect. 4.1.2).

Stuttgart is located in the vicinity of the low mountain range of the Swabian Jura. The measurement site at the university is situated at an altitude of 390 m ASL.

A daytime measurement was performed on 27 March 2006. The data were acquired at noon between 11:53 and 12:13 UTC with a vertical resolution of 60 m and a temporal resolution of 60 seconds. Figure 6.1 shows the elevation of the Sun on 27 March 2006 for Stuttgart during the course of the day. The elevation was approximately 42° during the lidar measurement. A nearby radiosonde ascent from Stuttgart-Schnarrenberg (13 km north to the lidar site) was used to calibrate the lidar. The radiosonde was launched at 12:00 UTC. The mean temperature profile measured by the RR lidar during the 20 minutes interval as well as that of the radiosonde are plotted in Fig. 6.2a. A moving average with a window length of 120 m below and 600 m above 1.5 km AGL was applied to the lidar data. The deviations between the lidar profile and the radiosonde as well as the statistical temperature uncertainty of the lidar profile are shown in Fig. 6.2b. Except for heights below 1 km AGL, the deviations were always smaller than the $1\text{-}\sigma$ statistical uncertainties of the lidar profile in this case.

This day was a rather sunny and warm day with shallow convective clouds developing at the PBL top during the late morning. Different insolation and orographic effects influenced the developing PBL which led to the observed differences between lidar and radiosonde. The $1\text{-}\sigma$ statistical temperature uncertainties did not exceed 3 K up to 5 km altitude AGL and were less than 1 K up to 3 km AGL. Figure 6.3 shows the temperature time-height cross section of 60-s temperature profiles. The lidar profile of 11:56 UTC is shown on the right side, with the radiosonde measurements illustrated as black circles. The statistical temperature uncertainties were not exceeding 1 K up to 1 km AGL and were well below 3 K up to 2 km height.

Figures 6.3a–c show the time-height cross section of the gradient of the logarithm of the range-corrected elastically scattered light, the particle backscatter coefficient and the temperature gradient dT/dz , respectively. In a well-mixed PBL, as presented here, the developing turbulence tends to mix heat, moisture, and momentum uniformly in the

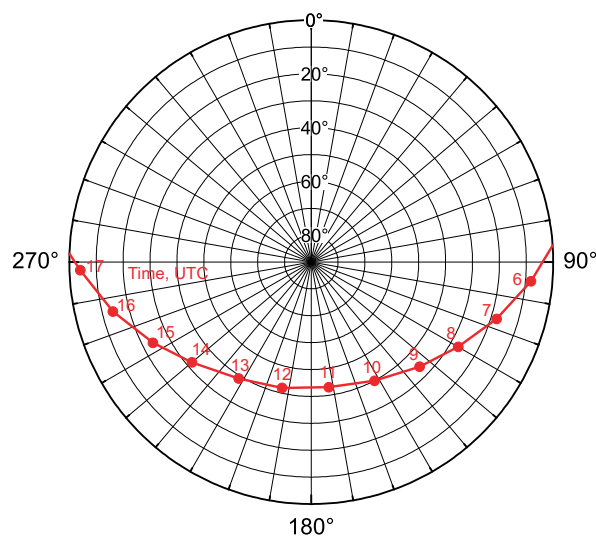


Figure 6.1: Elevation of the Sun on 27 March 2006 at Stuttgart during the course of the day. Circles indicate the elevation and radial lines the azimuthal angle of the Sun. The time of day is indicated in UTC.

vertical. Therefore, the aerosols act as tracers. With the assumption that the aerosol content is high in the PBL and low in the free troposphere, the top of the PBL can be determined by means of the logarithm of the range-corrected elastically backscattered signal which is located at the height where the gradient is smallest (dotted line) (Senff and Peters, 1994). The PBL top varied between 1.7 and 2 km AGL during the measurement period. This was also confirmed by the particle backscatter coefficient showing large aerosol backscatter due to humidity growth between heights of 1.5 and 1.8 km AGL. The top of the PBL can also be found by searching for the average height of the lowest inversion layer or lid which acts as a cap for the convection, such as shown in Fig. 6.3c. Values of the vertical temperature gradient between -2 and -6 K/km marked a stable region (solid line) correlating with the PBL top derived by the aerosol data (dotted line). Larger differences were found between 11:55 and 12:00 UTC, where the PBL top was as low as 1.5 km AGL according to the temperature gradient. In Fig. 6.3a, the minimum of the gradient of the logarithm of the range-corrected elastic signal is found at altitudes between 1.7 and 1.8 km AGL at the same time, but a region with neutral values was present down to 1.5 km AGL. The time lag is due to a temporal average of the temperature data of 5 minutes. This was necessary to reduce the statistical uncertainties of dT/dz . The statistical uncertainties of the temperature gradient were smaller than 0.5 K/km for heights up to 1 km AGL and smaller than 1.4 K/km below 2 km altitude applying a moving average of 480 m. The mean PBL height derived by the aerosol data and temperature gradient were about 1800 m and 1810 m, respectively.

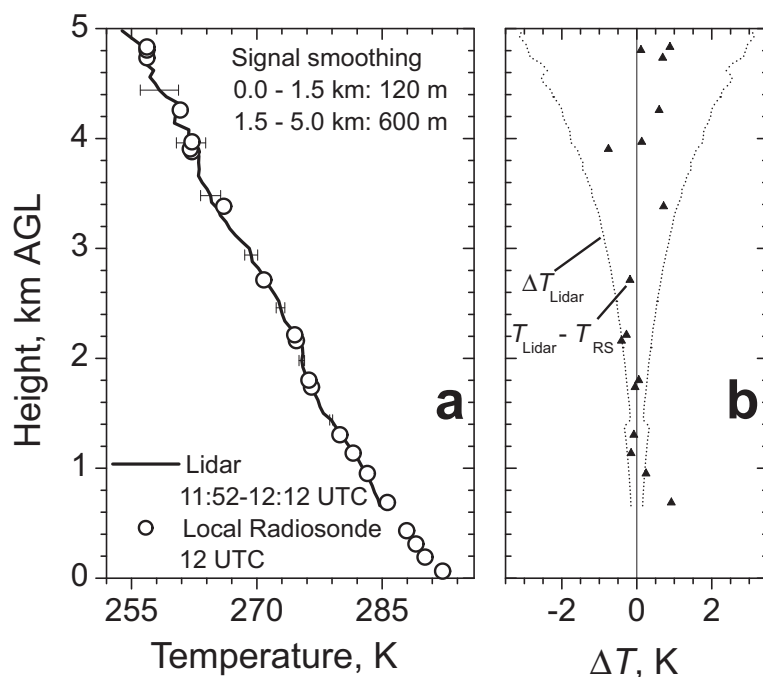


Figure 6.2: (a) Lidar and radiosonde temperature profiles measured on 27 March 2006 at UHOH. Lidar signals were smoothed with a moving average of the indicated window lengths. Error bars show the statistical uncertainty of the lidar profile. (b) Difference between lidar and radiosonde temperature and $1-\sigma$ temperature uncertainty of the lidar profile.

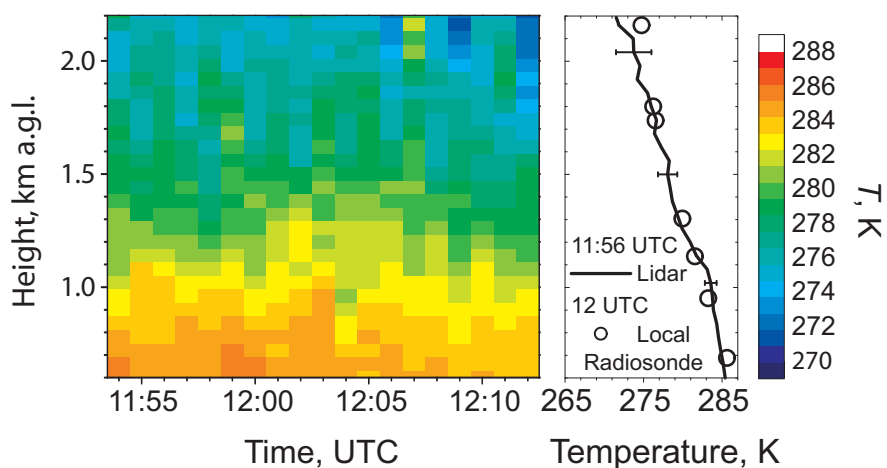


Figure 6.3: Left: Time-height cross section of 60-s temperature profiles between 11:53 and 12:13 UTC on 27 March 2006 at UHOH (Stuttgart, Germany). Right: Lidar profile with error bars from 11:56 UTC and local radiosonde. The lidar signals were smoothed with a moving average of 240 m.

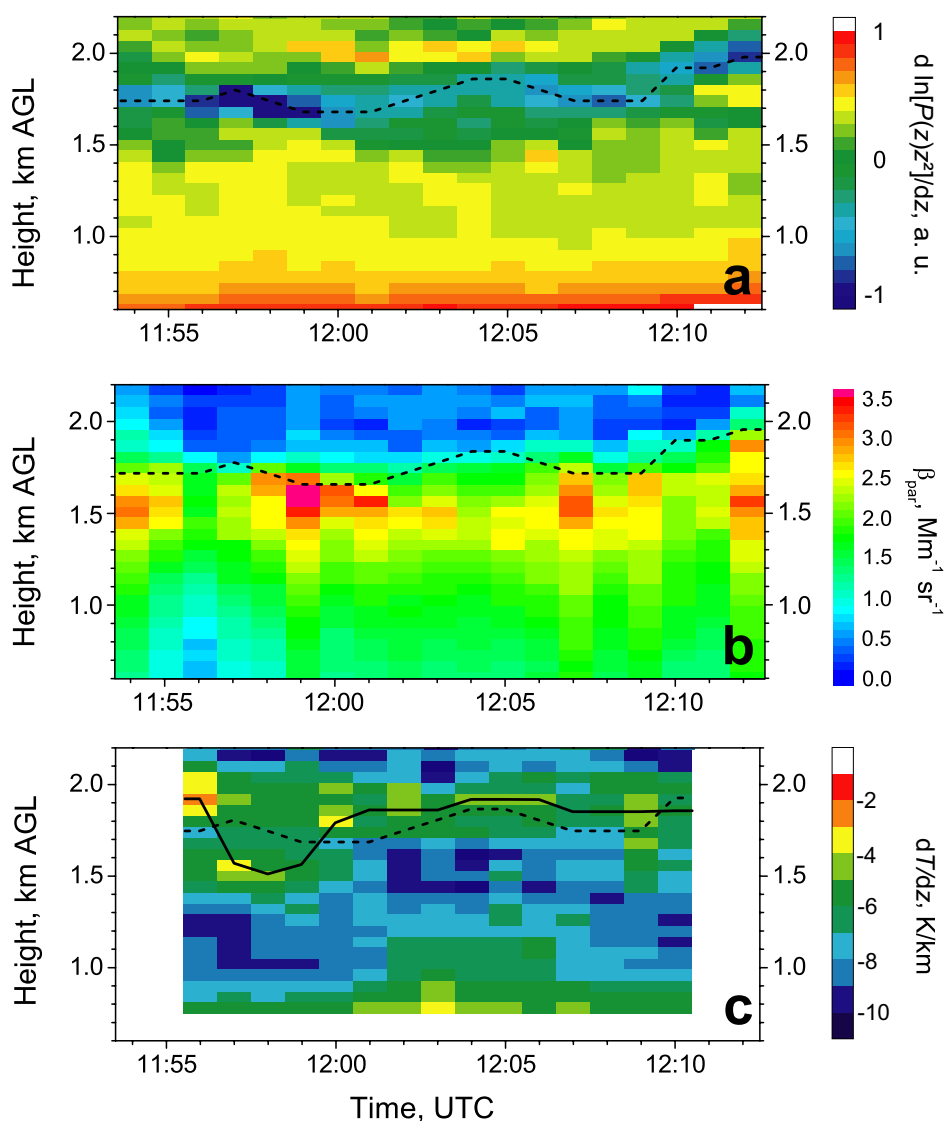


Figure 6.4: Time-height cross section of (a) the logarithm of the range-corrected elastic signal (b) the particle backscatter coefficient at 355 nm and (c) the temperature gradient on 27 March 2006 at UHOH (Stuttgart, Germany). The spatial resolution is 60 m and temporal resolution is 60 seconds. For calculating the gradient in (c), a moving average in time and range over 5 minutes and 480 m, respectively, was applied to the lidar data. The dotted line marks the PBL top derived by (a). The height where the temperature lid was strongest is assigned by the solid line.

Chapter 7

Temperature measurements during the field campaign PRINCE in July 2006

7.1 The PRINCE campaign

In the frame of the virtual institute COSI-TRACKS, the joint measurement program PRINCE of the participating institutions IMK-FZK, IPA-DLR, IPA (Mainz) and IPM was conducted from 10–21 July 2006. This campaign took place in the Northern Black Forest, Germany.

The aim of the campaign was to measure the atmospheric conditions before, during and after a convective event on days showing high potential for convection initiation (CI) in the Northern Black Forest. Therefore, observations of the evolution of the PBL and the air flow in the vicinity of the mountain peak Hornisgrinde were important objectives for investigating their influences on convection and their potential interaction. The development of secondary circulation systems during daytime were found to be an important trigger mechanism for convection in complex terrain (Barthlott et al., 2006; Richard et al., 2007; Rotach and Zardi, 2007; Rotunno and Houze, 2007). Detailed investigations of the temporal evolution and spatial variation of the PBL were performed in that region by airborne and ground-based in-situ measurements and radiosoundings (Kobmann et al., 1998; Kalthoff et al., 1998; Kobmann et al., 1999). During PRINCE, a unique setup of remote sensing instruments with scanning capability for the 3-dimensional observation of the atmosphere was deployed on top of Hornisgrinde (1161 m ASL) which is the highest mountain in that region. The scanning RR lidar of UHOH was collocated with a scanning Doppler wind lidar (Wieser, 2005) and a scanning cloud radar (Handwerker and G6rsdorf, 2006a,b).

Figure 7.1 shows the measurement site on top of the mountain. Below, the cross section from west to east through the lidar site on top of Hornisgrinde is shown. The terrain rises over a distance of 8 km, from the Rhine Valley to the west with an elevation of 150 m ASL, up to 1160 m ASL which is the mountain peak Hornisgrinde. To the east, ridges and valleys are characterizing the Black Forest. A radiosonde station was installed in a nearby valley in Brandmatt (48.61°N, 8.11°E, 675 m ASL) about 3 km to the west of the lidar site. Sondes of the type Graw DFM97 were launched regularly during intensive observation periods (IOP's).

Mobile teams launched drop-up sondes (Kottmeier et al., 2001) at assigned locations, in the direct proximity of convective cells covering the vertical structure directly in the area of interest. Additionally, different flight patterns were performed by the research aircraft DO-128 (Corsmeier et al., 2001) of the Technical University of Braunschweig, Germany, which was equipped with various meteorological sensors. The campaign also focussed on combining the data of remote sensing instruments in complex terrain to

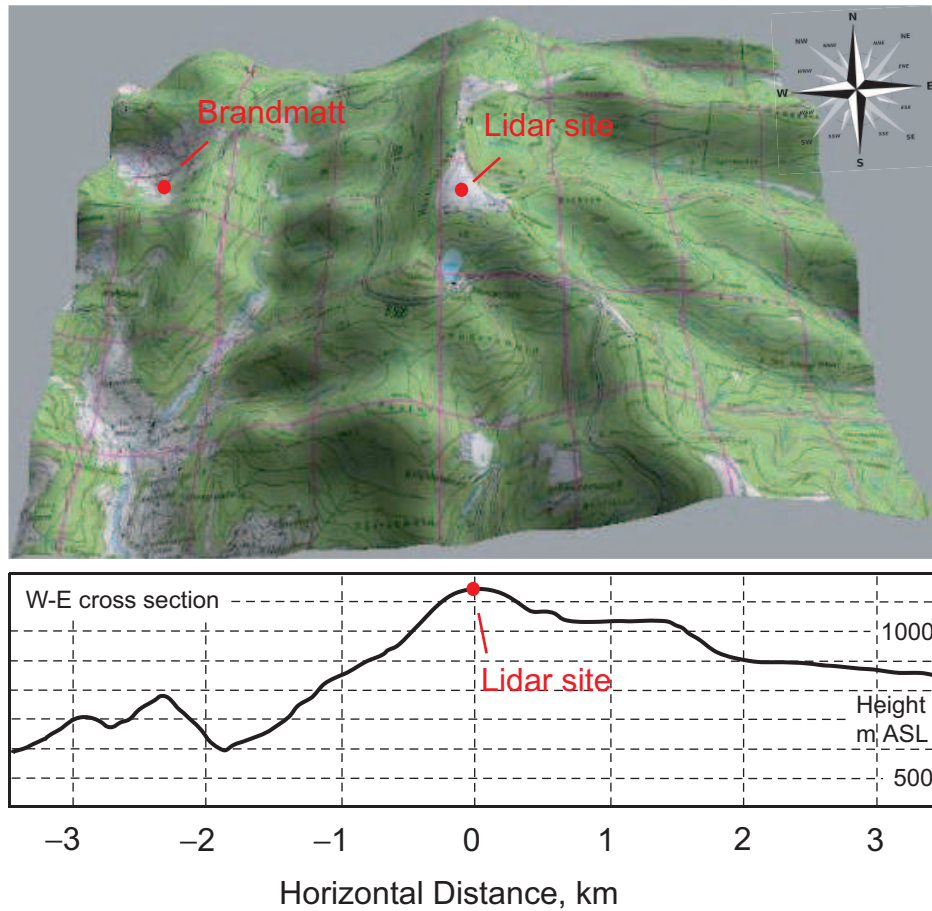


Figure 7.1: Overview of the measurement site in the Northern Black Forest region and cross section along a west-east transect through the lidar site on Hornisgrinde (1161 m ASL). The cartography is from Top25 View (digital maps by courtesy of Landesvermessungsamt Baden-Württemberg, Bundesamt für Kartographie und Geodäsie, Germany).

study convection. The UHOH RR lidar was operated during 125 hours on 13 consecutive days. An overview of the measurements that were performed during PRINCE is shown in Appendix B.1.

A case study of 12 July 2006 is presented by Groenemeijer et al. (2008). On this day, deep convection was initiated 15 km to the east of Hornisgrinde. Vertical temperature measurements of the RR lidar helped to understand why convection was inhibited above Hornisgrinde during the whole day. This example demonstrated the advantages of multi-sensor measurements in order to gain a comprehensive picture of the processes occurring in complex terrain. The performance of three convective-resolving models for this scenario has been published recently by Trentmann et al. (2008).

The system performance for all measurements performed in 2006 suffered because of a degradation of the protected silver coating that was applied to the three consecutive bending mirrors and the two scanner mirrors (see Sect. 4.2.2). On other days, the

system efficiency was much higher because the scanner mirrors as well as the three laser bending mirrors prior to the scanner were recoated after the PRINCE campaign.

7.2 Vertical temperature measurements

A nighttime measurement on 10 July 2006 is shown in Fig. 5.1b. The lidar signals were acquired for half an hour after sunset from 20:00–21:00 UTC. This day was characterized by a stable stratification of the atmosphere caused by a high pressure system that dominated over Central Europe on that day. A large-scale downward motion led to an adiabatic heating of the air in the atmosphere and, thus, more or less strong temperature lids — regions of stable stratified air — developed in the lower troposphere.

Figure 7.2 shows the lowest 4 km of the lidar temperature profile measured from 20:00–21:00 UTC in the evening on that day. Three well pronounced lids were observed by the lidar within the lowest 2 km AGL. It is noteworthy that for the calibration of the lidar data only the signals above 2 km were used here. Therefore, the observed differences between lidar and radiosonde between 1 and 2 km AGL are considered to be a real atmospheric feature. The temperature gradients derived from lidar temperature measurements and radiosonde are shown in Fig. 7.3. Up to the altitude of 3.5 km ASL, the radiosonde showed similar structures as the lidar measurement from 20:00–21:00 UTC. The lid, measured by the radiosonde at 1.2 km AGL, appeared to be about 200 m lower in the lidar measurement. The amplitude in the lidar profile was slightly smaller because of spatial and temporal averaged lidar signals. The lidar measurement from 21:00–22:00 UTC corresponds to the vertical measurement of the scan data presented in Sect. 7.3. The two lidar measurements showed changes in stratification in the lower troposphere above Hornsgrinde below an altitude of 3 km ASL.

The latter lidar profile yielded a very different picture of the atmosphere, albeit the radiosonde launched at 21:10 UTC is closer in time. The radiosonde only performs single point measurements along its ascent which are usually affected by drift with the wind, whereas the lidar measures a profile along the laser beam. Thus, different air volumes were probed. The two temperature lids that were measured by the lidar between 20:00 and 21:00 UTC at heights of 1 km and 1.6 km AGL completely merged to one layer. The observed differences can not be explained by the different smoothing length of 300 m that was applied to the lidar data measured between 21:00 and 22:00 UTC. Thus, warmer air was present from 21:00–22:00 UTC with a vertical extension of 600 m and a peak temperature gradient of about 5 K/km which marked a well pronounced inversion layer. The statistical uncertainty of the temperature gradient within the warm layer was smaller than 1 K/km.

7.3 Scanning temperature measurements during the night of 10 July 2006

For the first time, the lidar allows scanning measurements in order to investigate the variability of the temperature field.

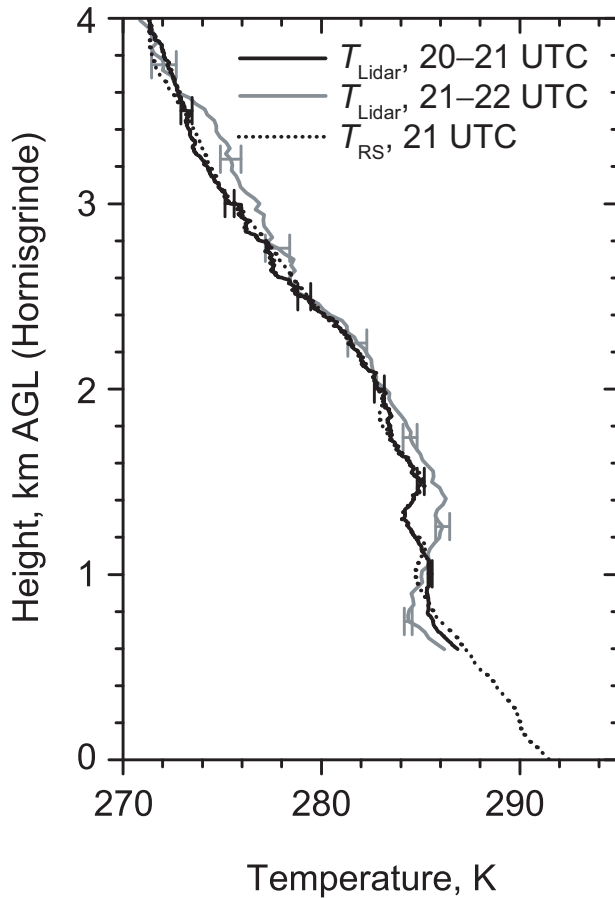


Figure 7.2: Temperature profiles of lidar and radiosonde (launched at 21:10 UTC from Brandmatt) measured on 10 July 2006 on Hornisgrinde. The lidar profile measured from 20:00–21:00 UTC is a section of the profile shown in Fig. 5.1b. A moving average of 150 m below and 450 m above 3 km altitude was applied to the lidar data. The lidar profile measured between 21:00 and 22:00 UTC corresponds to the vertical lidar measurement from Fig. 7.5a ($\Delta t = 6$ minutes). Here, a moving average of 300 m up to a height of 1.5 km AGL and 600 m and 1200 m below and above a height of 3 km AGL was applied to the lidar data.

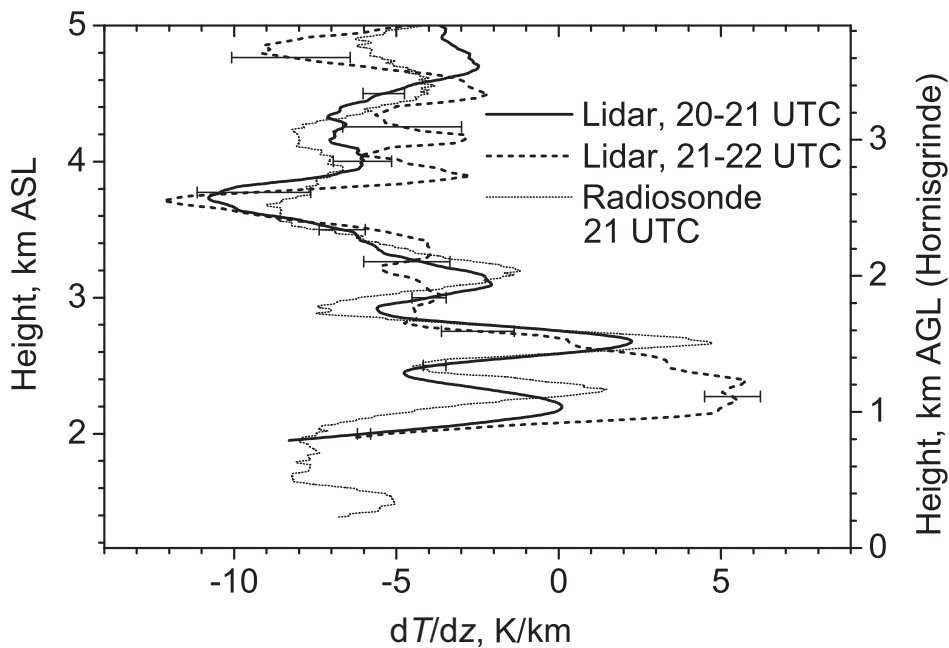


Figure 7.3: Temperature gradients on 10 July 2006 of the lidar temperature profile measured from 20:00–21:00 UTC ($\Delta t = 60$ minutes), the vertical lidar measurement from Fig. 7.5a ($\Delta t = 6$ minutes) and the radiosonde that was launched at 21:10 UTC from Brandmatt.

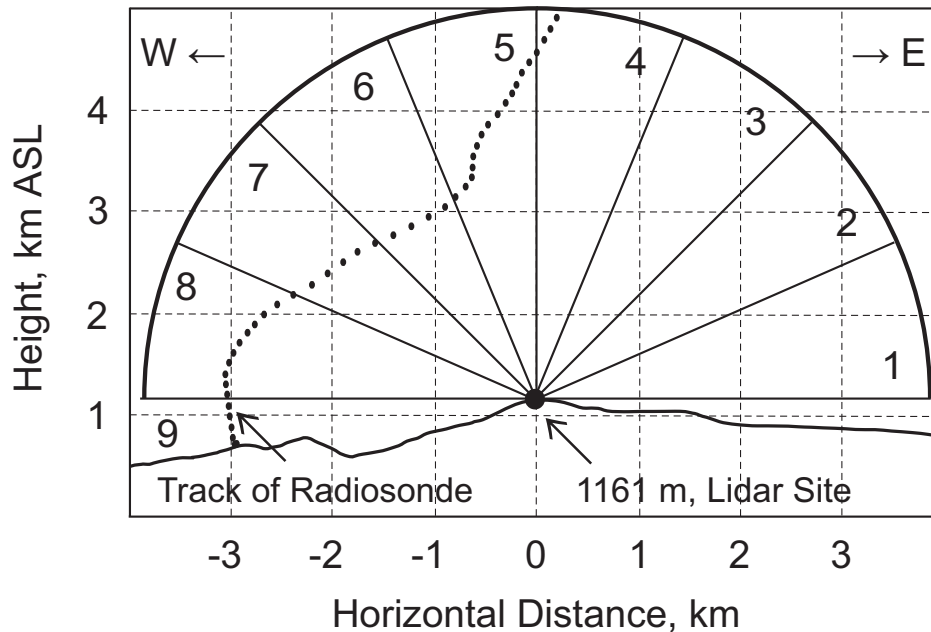


Figure 7.4: Scan pattern and W-E cross section through the lidar site. Numbers from 1–9 denote directions in which the profiles were measured. The track of the radiosonde (launched at 21:10 UTC from Brandmatt) transposed to this plane is illustrated by the dotted line.

A zonal-RHI-scan (RHI, Range-Height-Indicator) according to the scan pattern shown in Fig. 7.4 was carried out on 10 July 2006. With a constant elevation step of 22.5° , the lidar collected data between 21:00 and 22:00 UTC at nine different elevation angles. During this time, the laser beam was pointed to each direction for 1 minute. One full RHI-scan took approximately 10 minutes including the time when no data were acquired owing to the limitations of the data acquisition system. Within the measurement period, six RHI-scans were performed. Finally, the scans were summed up and a moving average was applied to the data with a window length of 300 m until a range of 1.5 km, 600 m below and 1200 m above 3 km range to improve the signal statistics. For the calculation of temperature profiles, the same calibration constants were used as determined by the measurement as shown in Fig. 5.1b on that day. The temperature field is shown in Fig. 7.5a. This figure shows that 1–1.5 km west of the mountain peak a region of constant temperature with $T \approx 287$ K was present which yielded steep horizontal temperature gradients. To the east, warm air was present at about 2.5 km ASL which marked a well pronounced inversion layer that is seen in the vertical temperature profiles shown in Fig 7.2 as well. Figure 7.5b shows the temperature gradient along the line of sight calculated from the temperature data. The inversion at around 2–2.5 km ASL did not exist only to the east of the mountain but also to the west, where the gradient was relatively less strong. The dotted line marks the peak value of dT/dR within that region. Westerly winds persisted on this day as was observed by the nearby radiosonde measurements. The airflow was weak-to-moderate with 2–9 m/s

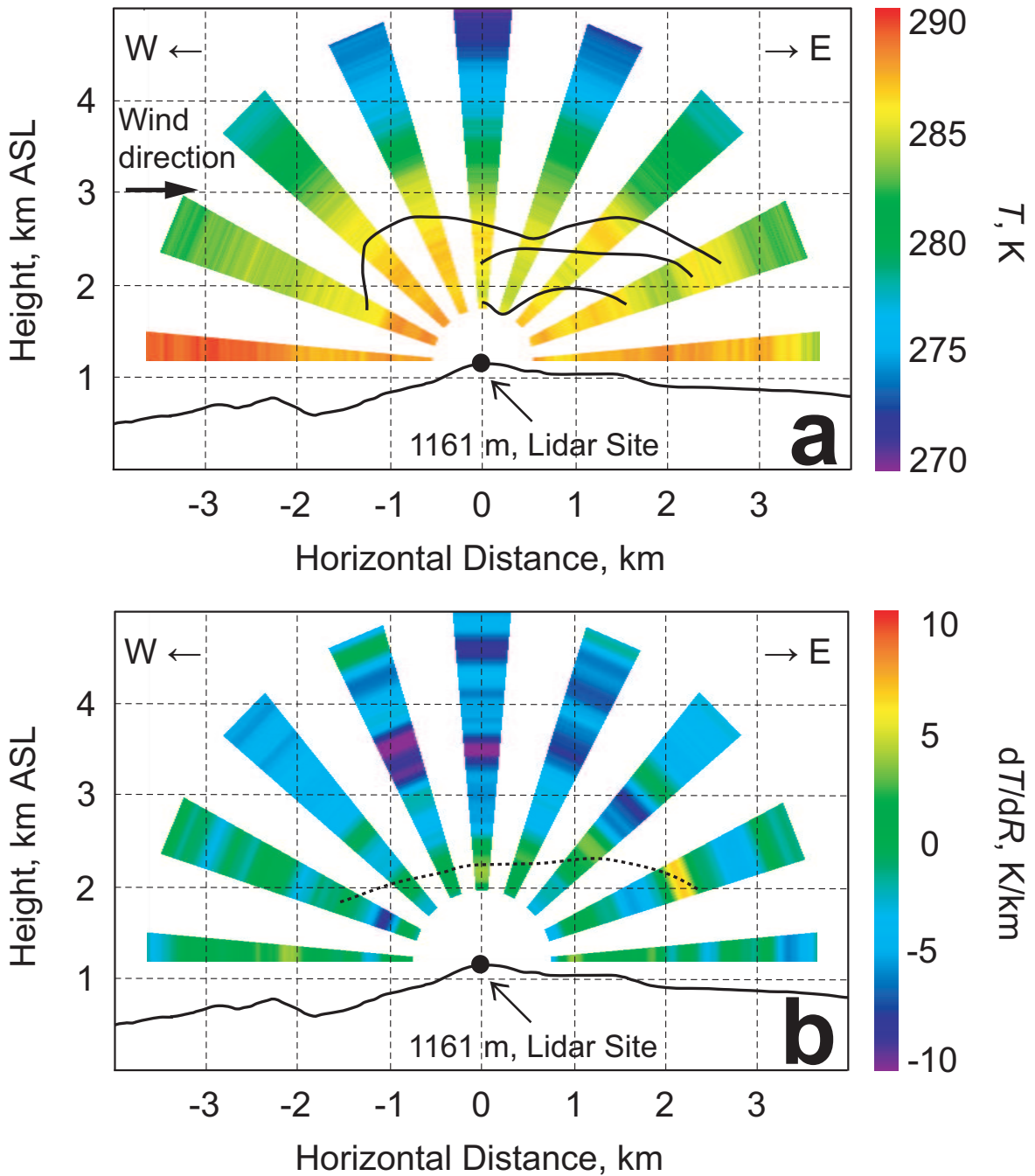


Figure 7.5: (a) Temperature field and (b) field of the temperature gradient along the line of sight on Hornisgrinde on 10 July 2006 measured between 21:00 and 22:00 UTC. 6 consecutive scans were summed up which provides a temporal resolution of 6 minutes for each profile. A moving average of 300 m until 1.5 km range, 600 m and 1200 m below and above 3 km range, respectively, was applied to the lidar signals. Solid lines in (a) mark the 285-K isotherm and the dotted line in (c) assigns a region where the temperature gradient was enhanced showing an inversion layer.

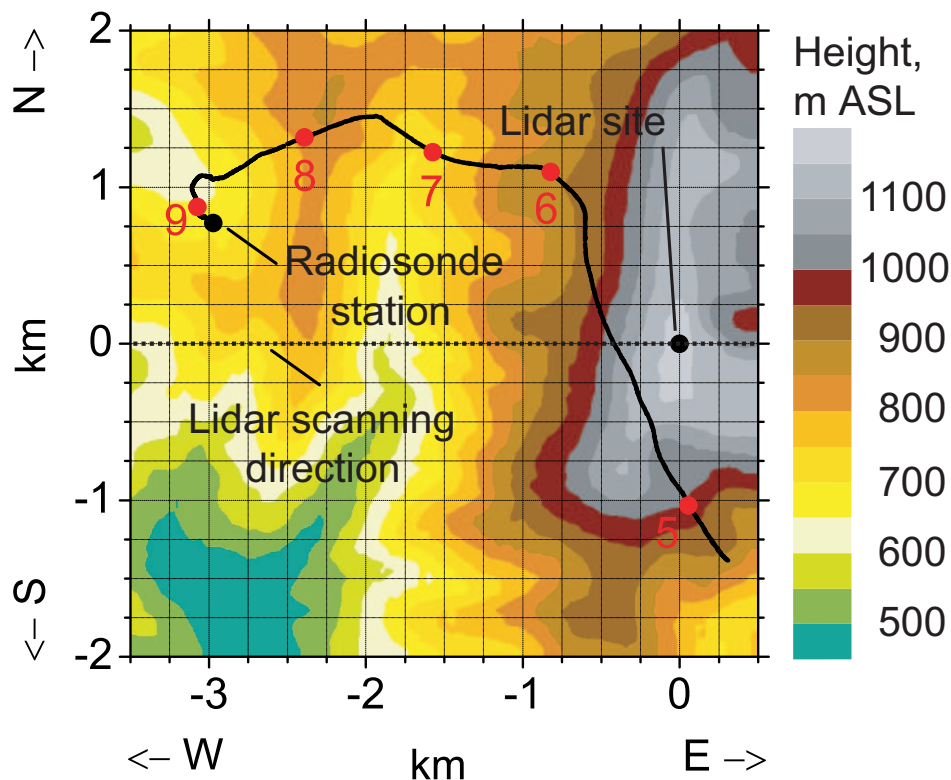


Figure 7.6: Orography and overlay of the radiosonde track transposed to the horizontal plane. Height intersections where the lidar measured at the same height as the radiosonde are marked by red circles with the corresponding profile number according to Fig. 7.4. Information of the topography by courtesy of Landesvermessungsamt Baden-Württemberg, Bundesamt für Kartographie und Geodäsie, Germany.

throughout the whole troposphere. The air approaching from the Rhine Valley to the mountain ridge was forced to move upward on the western slope of Hornisgrinde. Due to the stable stratification, the upward motion was blocked at around 2–2.3 km ASL; the height of the lowest temperature lid (see Fig. 7.3). Similar structures were observed by aircraft measurements in Koßmann et al. (1999). Figures 7.5a,b show that the inversion layer above Hornisgrinde was lifted, whereas farther east an increase in the vertical extent of the inversion was observed. The sequence of stable and more unstable regions that developed to the east are indication of gravity waves that might have been triggered by the stable stratification and the presence of a westerly wind in the lower troposphere.

The track of the radiosonde in the west-east cross section is illustrated in Fig. 7.4 (dotted line). 21:20 UTC onwards, it reached the altitude of 5 km ASL after 25 minutes. Figure 7.6 shows a projection on the horizontal plane of the flight track with an overlay of the surrounding orography. The red dots indicate the position during the ascent where the radiosonde measured at the corresponding height intersection of the lidar profile (red number). The sonde drifted primarily eastward up to a height of

Table 7.1: Lidar temperature versus radiosonde at height intersections for the measurement example shown in Fig. 7.5a.

Scan number	Spatial distance of measurement points lidar–radiosonde	T_{RS}	T_{Lidar}	ΔT_{Lidar}	$T_{\text{Lidar}} - T_{\text{RS}}$
5	1.0 km	273.3 K	274.0 K	0.6 K	0.7 K
6	1.1 km	283.0 K	284.7 K	0.5 K	1.7 K
7	1.2 km	284.5 K	285.2 K	0.5 K	0.7 K
8	1.2 km	284.7 K	283.9 K	0.7 K	0.8 K
9	0.9 km	290.1 K	288.9 K	0.7 K	1.6 K

3 km ASL which was close to the point indicated by 6 in Fig. 7.6. At this altitude, a pronounced wind shift occurred causing the sonde to be drifted away southeastward until the end of the track. The single temperature profiles measured by the lidar are shown in Fig. 7.7. The points where the radiosonde intersected the height level of the corresponding lidar profile are marked with black circles.

Table 7.1 summarizes the intersecting points. The lidar temperature measurement and the snap shot of the radiosonde were in good agreement within the statistical uncertainties. At the intersecting points of profiles 6 and 9, the deviations were larger than the uncertainties of the lidar data. At the height intersection with profile 9, the lidar probed a volume about 900 m south of the radiosonde as can be seen in Fig. 7.6. This explains the observed differences due to the different elevations of the orography. At the intersecting point with lidar profile 6, the radiosonde entered a height level where the wind direction changed. Wind shifts in the free troposphere are normally accompanied by temperature changes since different air masses are present. Lidar profile 6 shows a significant break at about 3.2 km ASL which marks a sharp boundary between warm air close to the mountain and colder tropospheric air.

Profiles 3–5 support the aforementioned statement that a strong temperature inversion developed on the lee side of the mountain at around 2–2.5 km ASL which was not well pronounced in profiles 6 and 7 to the west of the mountain.

7.4 Performance during PRINCE

Figure 7.8 displays the temperature uncertainties for all lidar profiles of the scanning measurements shown in Fig. 7.5a. ΔT was always smaller than 1.1 K. An increase of up to 60% was observed for lower elevation angles. This was caused by a polarization-dependent reflection of the laser beam at the scanner mirrors (see Sect. 4.2.2).

The measurement time that is required to achieve a $1-\sigma$ statistical temperature uncertainty of less than 1 K at a certain height with range resolution Δz is shown in

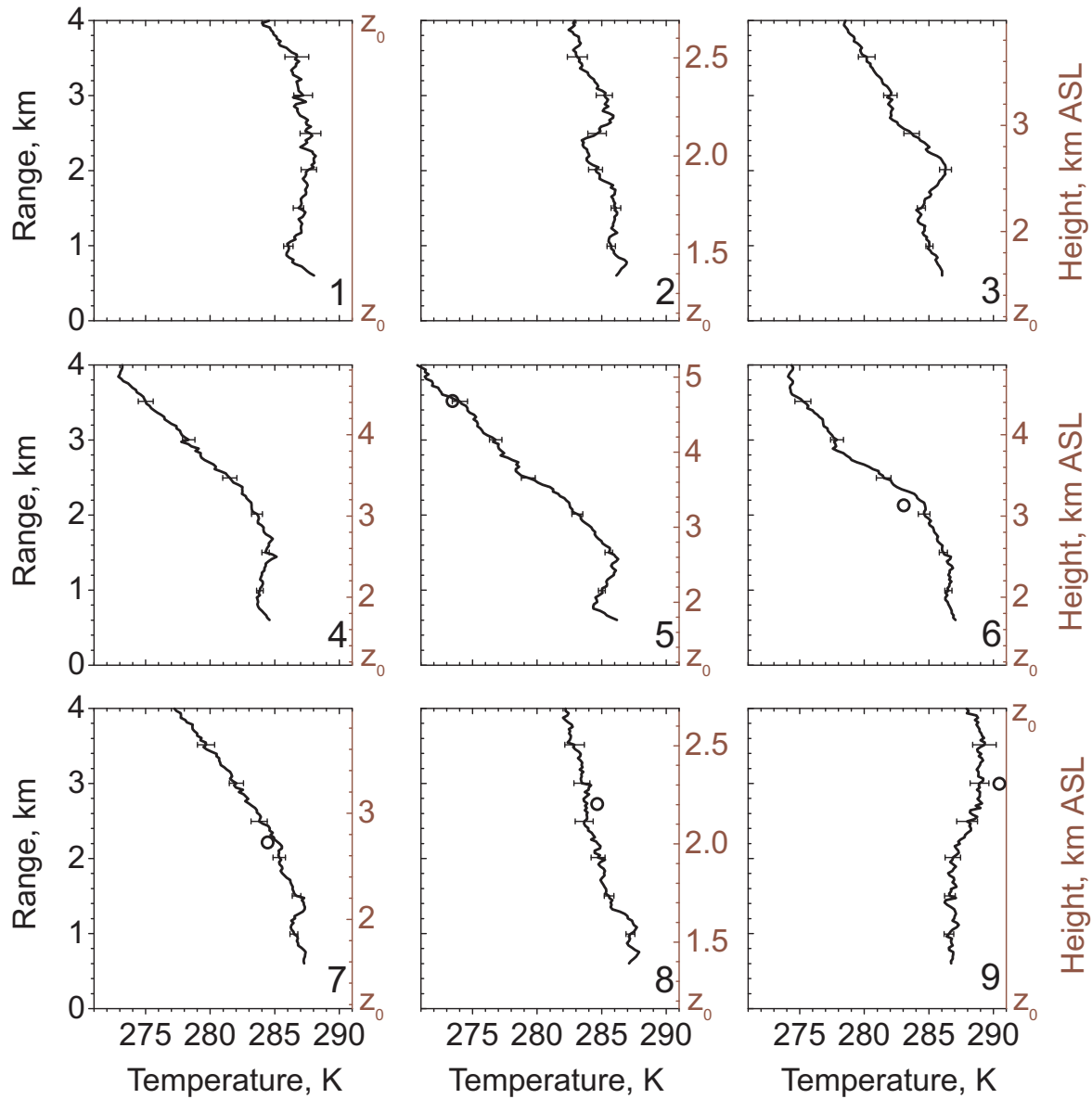


Figure 7.7: Temperature profiles for each scan direction measured on 10 July 2006 from 21:00–22:00 UTC. The single profiles correspond to the data shown in Fig. 7.5a. Error bars show the statistical temperature uncertainty of the lidar measurement. Black circles denote the temperature measured by radiosonde at the corresponding height intersections. z_0 marks the height of the lidar site of 1161 m ASL. Numbers 1–9 correspond to the elevation angles of each profile according to Fig. 7.4.

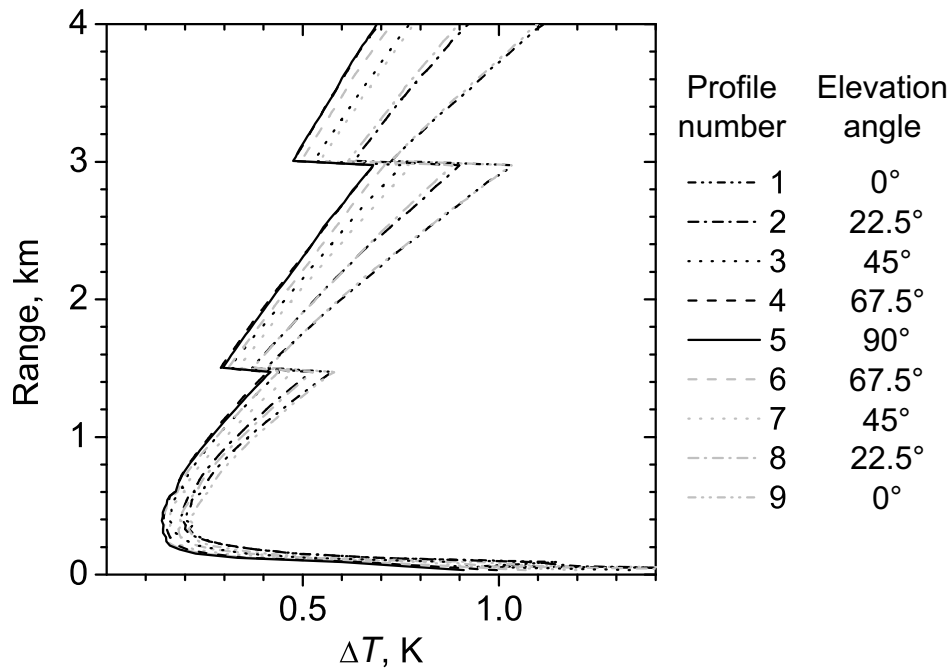


Figure 7.8: Temperature uncertainty of the lidar profiles shown in Fig. 7.7. The numbers 1–9 correspond to the elevation of the profiles shown in Fig. 7.4. The steps at 1.5 km and 3 km range are due to the changing window length of the moving average.

Fig. 7.9. The lidar measurement of 27 March 2006 (Section 6) and 10 July 2006 (Section 7.2) were used to assess the daytime and nighttime performance, respectively. The performance for daytime conditions showed that an integration time of 3 minutes and a range resolution of 300 m were necessary to cover the PBL extending up to 1.5 km AGL. Daytime temperature measurements in the lower troposphere up to 3 km altitude AGL were successfully carried out with a range resolution of 600 m and a temporal resolution of 10 minutes. During nighttime an integration time of one hour and a range resolution of 600 m were needed to yield statistical temperature uncertainties smaller than 1 K throughout the troposphere. Data acquired with a range resolution of 300 m and a temporal resolution of 10 minutes yielded ΔT smaller than 1 K in the lowest 4 km AGL.

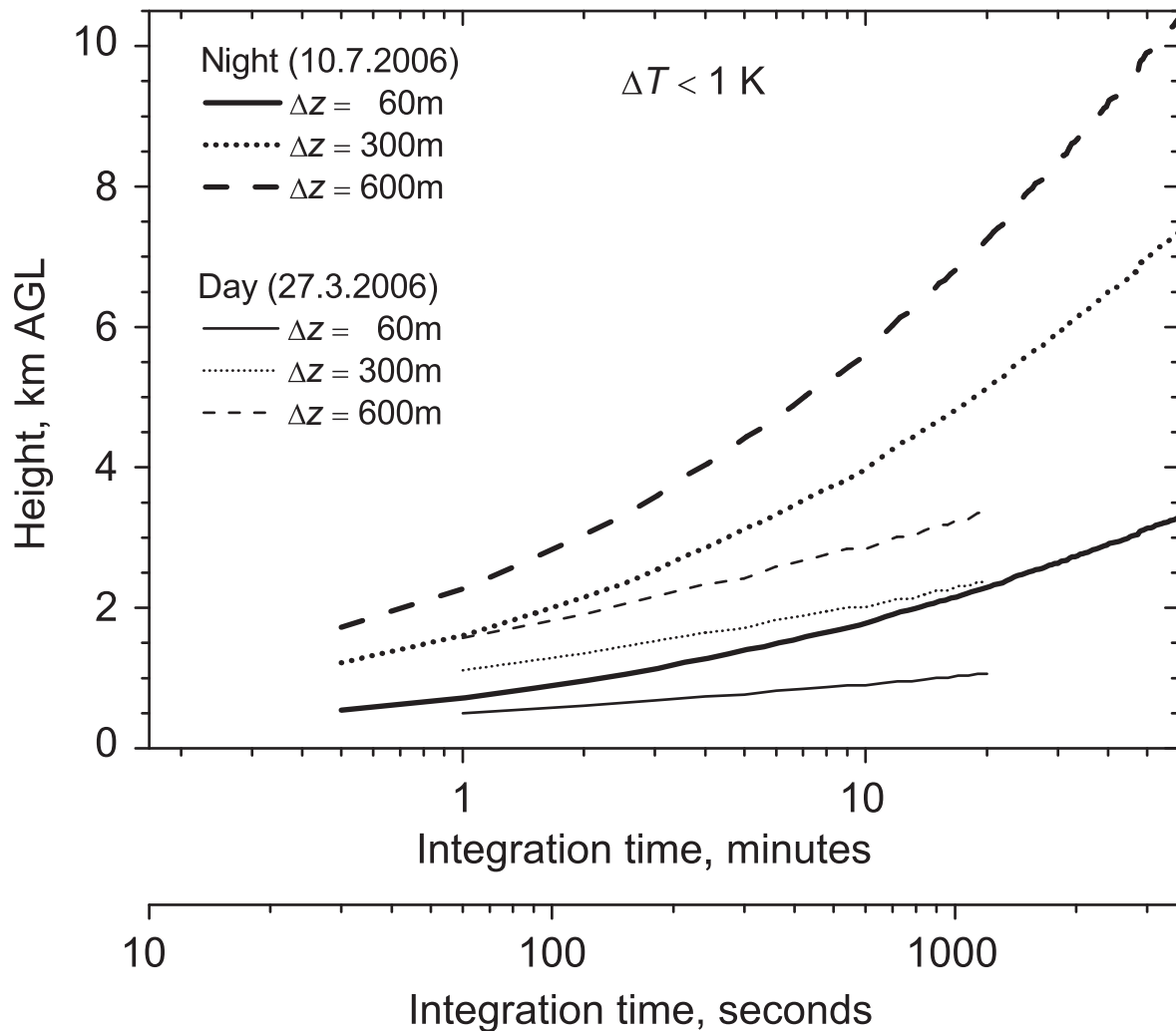


Figure 7.9: Required measurement time to achieve a $1-\sigma$ statistical uncertainty of less than 1 K for different range resolutions. The data of 27 March 2006 (Section 6) and 10 July 2006 (Section 7.2) were used to assess the daytime and nighttime performance, respectively.

Chapter 8

Temperature measurements during the field campaign COPS in summer 2007

The RR lidar was deployed during the field experiment COPS in summer 2007 on Hornisgrinde in the Northern Black Forest, Germany. Section 8.1 briefly describes the campaign and the experimental setup. Section 8.2 shows a measurement example for scanning measurements of temperature in daytime and discusses the meteorological aspects. Statistical temperature uncertainties in dependence on the elevation angle of the Sun are analyzed in Sect. 8.3.1. Section 8.3.2 summarizes the performance of the UHOH RR lidar during the COPS campaign compared to the previous deployment. Finally, in Sect. 8.4 a spectral analysis of a temperature time series with a temporal resolution and range resolution of 10 s and 37.5 m, respectively, is performed.

8.1 COPS

The field campaign COPS took place from 1 June 2007 until 31 August 2007 in the southwestern part of Germany. The COPS region stretches from the Swabian Jura over the Black Forest to the Rhine Valley and the Vosges mountains in eastern France. COPS (Wulfmeyer et al., 2008a) is part of the German Priority Program “Praecipitationis Quantitativae Predictio” and is endorsed as World Weather Research Program Research and Development Project. It is the overarching objective of COPS to advance the quality of forecasts of orographically-induced convective precipitation by 4D observations and modeling of its life cycle.

A large suite of state-of-the-art remote sensing systems — ground-based as well as airborne — were combined with in-situ instruments. The ground-based remote sensing instruments of COPS were collocated at five so-called supersites. This allowed to derive synergetic data products such as relative humidity, equivalent potential temperature, latent and sensible heat fluxes, which are considered to be highly beneficial to advance CI studies (Behrendt et al., 2008; Pal et al., 2008). The measurement strategies involved lidar systems as key instruments to provide high resolution data of atmospheric humidity, temperature, wind, and aerosols until convection was initiated and the subsequent rain began.

Figure 8.1 shows a map of the Northern Black Forest where a transect of three supersites was established during COPS. Yet another supersite was located in the French Vosges mountains and one more to the east of the Black Forest near Stuttgart, Germany. The UHOH RR lidar was deployed on the mountain Hornisgrinde which was called supersite H. This site was located in between the two neighboring supersites in the Rhine Valley (R) and the Murg Valley (M) being 11 km to the west-northwest and 16 km to the east-southeast to supersite H, respectively. On top of Hornisgrinde, the same instrumental

setup was realized as during the PRINCE campaign (see Sect. 7.1). In addition, the scanning water vapor DIAL of UHOH (Schiller, 2009; Wulfmeyer et al., 2008b; Behrendt et al., 2008), the scanning microwave radiometer of IMAA-CNR (Istituto di Metodologie per l'Analisi Ambientale–Consiglio Nazionale delle Ricerche), Potenza, Italy (Cimini et al., 2006), the S-band Transportable Atmospheric Radar (TARA) (Heijnen et al., 2000) of IRCTR (International Research Center for Telecommunications-transmission and Radar), Delft, Netherlands and a container for in-situ aerosol measurements of the University of Manchester, UK. Furthermore, in-situ sensors such as energy balance stations, automatic weather stations and soil moisture sensors were installed.

A number of different measurement strategies were operated on Hornisgrinde with respect to the ambient weather condition and mission plans (Wulfmeyer et al., 2007). An overview of the operations performed with the UHOH RR lidar during COPS is given in Appendix B.2. In principal, three different scan modes were operated: fixed vertical pointing, continuous RHI scans at one predefined azimuth angle and a combination of vertical pointing and RHI scans. The scans of the instruments on Hornisgrinde were coordinated along the axis of the supersites R–H–M. This is shown schematically in Fig. 8.1. A radiosonde station was deployed on Hornisgrinde from 10 June 2007 to 31 August 2007. Radiosondes were launched every 3 hours during IOPs. Sondes of the type RS-80 (only in June) and RS-92 (July and August) by Vaisala, were used. Ascents of 175 collocated radiosondes are available for comparisons with lidar measurements and microwave radiometer. During COPS, the RR lidar was operated during 250 hours on 27 IOP days.

The efficiency of the UHOH RR lidar was improved compared to the previous field campaigns. The power efficiency product was increased by a factor of up to 80 (see Sect. 4.2.2). For the first time, scanning temperature measurements during daytime could be performed due to the significant enhancement of the SNR.

8.2 Daytime scanning measurements on 25 August 2007

Figure 8.2 shows the scan pattern that was performed during COPS along the axis of the three supersites R–H–M at an azimuth angle of 291° with respect to north. Compared to the relatively coarse scan pattern that was performed during the PRINCE campaign (see Fig. 7.4) the beam was pointed at 21 angles (9° steps between individual profiles). During the Sun passage, the pattern was reduced to protect the detectors in the receiver against direct solar radiation. At each direction, the data were collected for 13 seconds. A total time of about 5 minutes was needed for one scan including the time when no data could be acquired owing to the limitations of the data acquisition system. Besides the measurement of the temperature field, where several scans have to be summed up in order to increase the signal statistics, it was possible to observe the aerosol for each scan.

During IOP 18b on 25 August 2007, the lidar performed scans following Fig. 8.2 from 9:00–17:00 UTC. The weather conditions over Central Europe were characterized by a weakening upper level trough and associated high pressure influence on the ground.

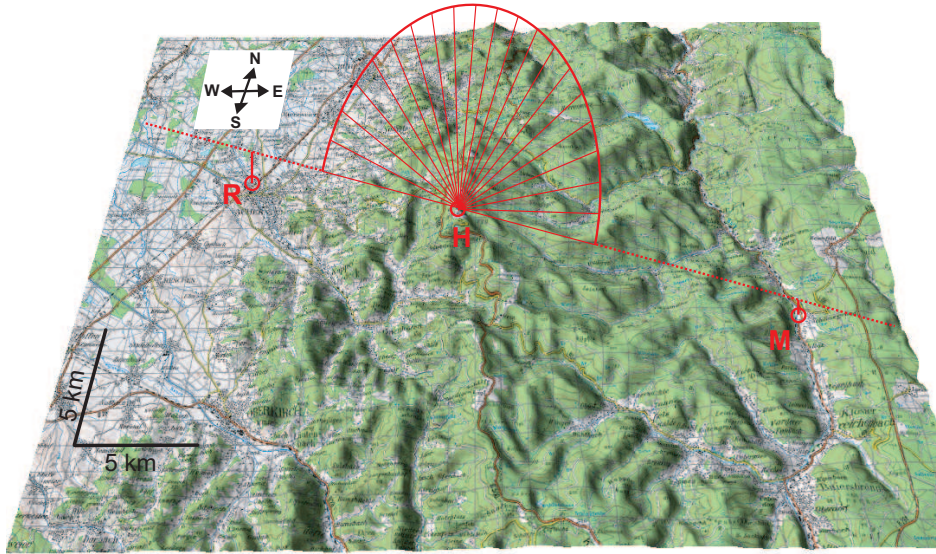


Figure 8.1: Map of part of the COPS region in the Northern Black Forest, Germany. The three COPS Supersites Rhine Valley (R), Hornisgrinde (H) and Murg Valley (M) are marked. The red line marks the azimuth angle at which RHI scans on Hornisgrinde were coordinated with other instruments at the site. The width of the mesh (gray lines) overlaid to the map is 1 km. The cartography is from Top25 View (digital maps by courtesy of Landesvermessungsamt Baden-Württemberg, Bundesamt für Kartographie und Geodäsie, Germany).

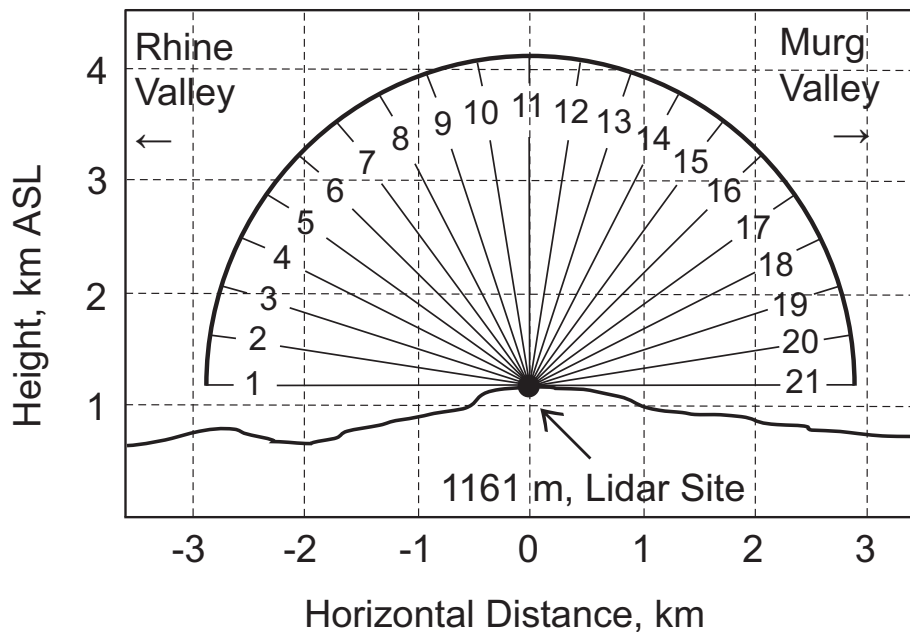


Figure 8.2: Scan pattern and cross section through the lidar site on supersite H at an azimuth angle of 291° (see Fig. 8.1). Numbers from 1–21 denote the pointing direction for each profile.

Therefore, subsidence in the upper and middle troposphere was expected. Shallow convection was triggered over the Black Forest during the day. The measurement site on Hornisgrinde was covered with clouds until 12:00 UTC. During the late afternoon, the clouds dissolved first towards the west (Rhine Valley) and until the early evening also towards the east (Murg Valley). Three consecutive scans, similar to the scan sketch in Fig. 8.2, of potential temperature are shown in Figs. 8.3a–c. The particle backscatter coefficient and the gradient of potential temperature are shown in Figs. 8.4a–f. Each scan covers about one hour of measurement consisting of 13 and 9 raw scans in case of Figs. 8.3a,c, Figs. 8.4a,c,d,f and in case of Fig. 8.3b, Figs. 8.4b,e, respectively. In each direction, the data were acquired for 13 s with a range resolution of 37.5 m. For the averaged scans, this resulted an effective measurement time of 169 s (Figs. 8.3a,b and Figs. 8.4a,c,d,f) and 117 s (Fig. 8.3b and Figs. 8.4b,e) for each profile. For the temperature data, a moving average of 300 m was applied to the signals. The vertical lidar data of the scan (profile 11 in Fig. 8.2) measured between 16:00 and 17:05 UTC and the radiosonde launched at 17:00 UTC were used to calibrate the lidar. The same calibration constants were applied to the scan measured in the period 14:55–16:00 UTC. A slightly modified calibration was used for the period 13:50–14:55 UTC to correct for a small offset of about 1 K.

A function to correct the overlap for ranges < 1.5 km AGL was applied to the lidar data from 13:50–17:05 UTC. Further details about the correction are described in Sect. 8.3.1. Figures 8.3a–c show the potential temperature θ and Figs. 8.4d–f the gradient of the potential temperature $d\theta/dz$. The potential temperature is defined by

$$\theta = T \left(\frac{1000}{p} \right)^{R_L/c_p}, \quad (8.2.1)$$

with temperature T , pressure p , the gas constant for ambient air R_L and the specific heat of ambient air at constant pressure c_p . θ is a conserved quantity for dry-adiabatic processes. In the atmosphere, θ is constant with height within well-mixed layers where temperature lapse rates of $-1\text{K}/100\text{m}$ are present. θ is also invariant for descending or ascending air parcels that undergo dry-adiabatic warming or cooling, respectively.

The particle backscatter coefficient in Figs. 8.4a–c was calculated by a technique that is used for scanning Raman lidar. For each scan the reference height was found at a certain range in the vertical or close to vertical where $\beta_{\text{par}} \approx 0$ (compare Sect. 2.4, Eq. (2.4.4)). In the measurement example presented here, the reference level was found at a height of 3.5 km AGL. This information then could be used to iteratively calculate β_{par} for lower elevation angles without the necessity to find the reference level again (Pal, 2009).

The particle backscatter coefficient in Fig. 8.4a showed large values of $> 4 \text{ Mm}^{-1} \text{ sr}^{-1}$ towards the east of Hornisgrinde (white color, right side of the image) in the first one hour period marking dense cumulus clouds at 2 km ASL. Backscatter ratios of up to 50 were observed in the region of the cloud causing strong signal extinction. Due to large uncertainties, the temperature data beyond 1 km range are not reliable.

The clouds developed east of Hornisgrinde at the top of an aerosol layer. This aerosol layer is seen in Fig. 8.4a (left part of the picture) to the west of the mountain peak where

no clouds occurred. This layer was associated with the PBL extending to about 2 km ASL close to the mountain peak. Figure 8.4d shows higher positive values of $d\theta/dz$ at the top of the aerosol layer which became weaker towards the mountain ridge. Atop, a more unstable region was observed, followed by a stable layer with $d\theta/dz \approx 0.6$ K/100m between 2.7 and 3 km ASL. Due to higher statistical temperature uncertainties, the gradient became increasingly noisy above 3 km ASL. A well defined zone with potential temperatures around 305–307 K stretched downward from about 2.5 km west of the mountain peak as shown in Fig. 8.3a. Values of potential temperature supported that warmer air was present within this zone suggesting that air from altitudes of about 2 km ASL was mixed downward to lower levels.

In the second period (Fig. 8.3b and Figs. 8.4b,e), the clouds to the east disappeared slowly and the height of the PBL decreased following the topography west of Hornisgrinde. This suggested the transition towards a more stable PBL. θ and $d\theta/dz$ were influenced by a stronger extinction for profiles 13–19 (see Fig. 8.2) at heights of about 2 km ASL causing unreliable temperature information in that region.

In Fig. 8.4b, a thin layer with enhanced backscatter coefficients due to advected aerosol particles is seen at 3.3 km ASL. This layer was not observed before in Fig. 8.4a. A strong gradient of potential temperature was predominant above this aerosol layer. $d\theta/dz$ shows a stable layer at around 2.5–3 km ASL with 0.4–0.6 K/100 m.

Between 16:00 and 17:05 UTC, the aerosol layer became more distinct with β_{par} up to $2.5 \text{ Mm}^{-1} \text{ sr}^{-1}$ at 2.5–3.5 km ASL as shown in Fig. 8.4c. The PBL top further subsided to the east as well as to the west of Hornisgrinde. $d\theta/dz$ became weaker at 3 km ASL compared to Fig. 8.4e and showed values of around 0.4 K/100 m above Hornisgrinde likely due to a cooling of the ambient air caused by the advected aerosol layer. The radiosounding at 17:00 UTC, shown in Fig. 8.5c, showed relative humidity of about 75% between 2.4 and 3.4 km ASL, exactly at the height of the aerosol layer. The wind direction turned from southwest to west and the wind speed increased slightly from 3–5 m/s to about 7 m/s between 2.5 and 3 km ASL as illustrated by the measurements of the radiosonde in Fig. 8.3a (right side). Above that strong aerosol layer, the lidar measurements showed a temperature lid between 3.5 and 4 km ASL with $d\theta/dz$ close to 1 K/100 m being observed during the previous period too. The lid appeared to be constant in height in the vicinity of the mountain ridge.

Within a range of 1–1.5 km to the west of the mountain peak, the θ -field of the lidar measurement indicated a region with values of about 302–304 K, where the potential temperature was considerably colder than to the east of the mountain peak. Here, a warm θ -tongue stretched downward with potential temperatures of about 306 K indicating downward mixing of air.

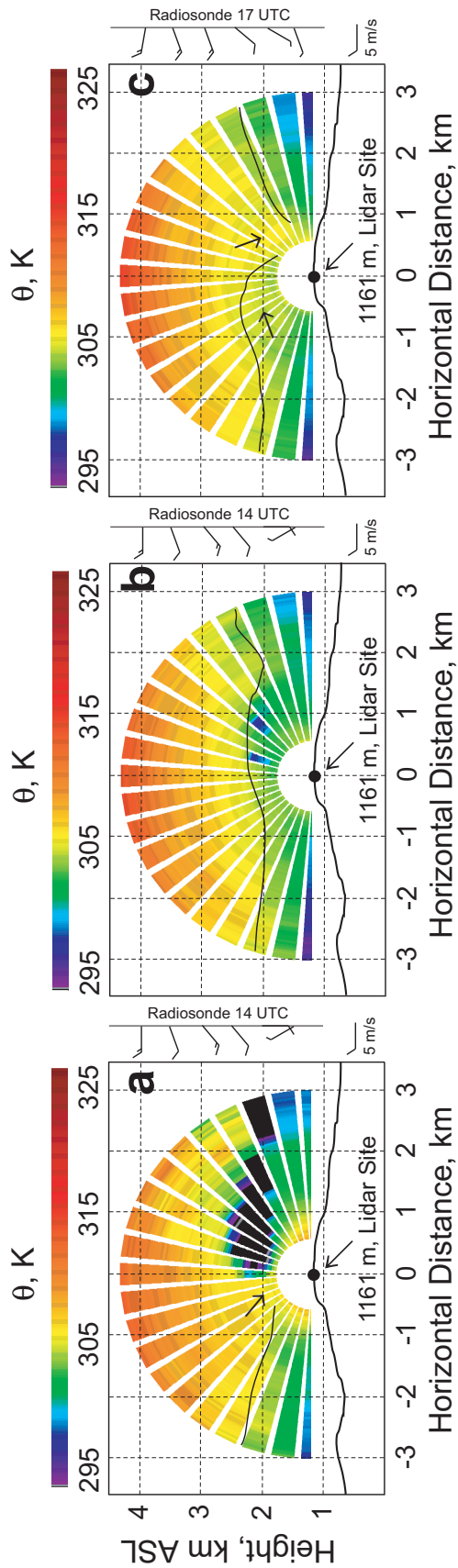


Figure 8.3: Field of potential temperature measured at 21 elevation angles on Hornsgrinde on 25 August 2007. The data were acquired from (a) 13:50–14:55 UTC, (b) 14:55–16:00 UTC and (c) 16:00–17:05 UTC. In case of (a) and (c) 13 and for (b) 9 consecutive raw-data scans were averaged giving an averaging time of 169 s and 117 s for each profile, respectively. The range resolution is 37.5 m. A moving average of 300 m was applied to the data. The plane in which the RHI-scan was performed was orientated towards the neighboring COPS Supersites (azimuth = 291°, see Fig. 8.1). The wind was measured by the radiosonde launched at 14:00 UTC (a, b) and 17:00 UTC (c). The black line marks the 305 K isentropic surface. Black and blue regions in (a) and (b) at around 2 km ASL are undependable temperature data due to clouds.

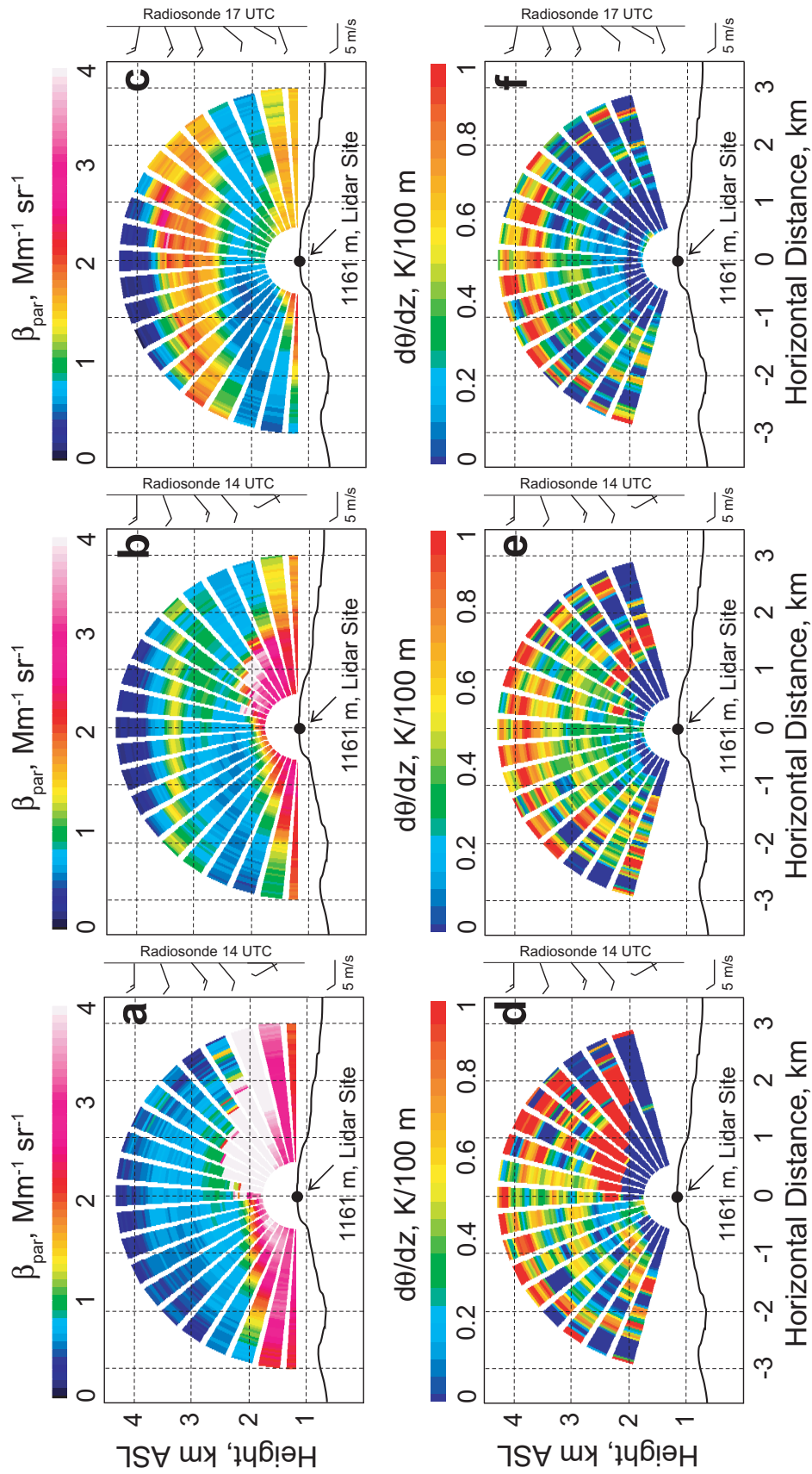


Figure 8.4: Same as Fig. 8.3a-c but with field of (a-c) particle backscatter coefficient and (d-f) gradient of potential temperature. White colors in (a) and (b) at around 2 km ASL show clouds which yielded unreliable gradients in (d) and (f).

8.3 Performance

8.3.1 Statistical temperature uncertainties in dependence on the solar elevation angle

Figure 8.5a shows the temperature profile measured at an elevation angle of 72° (profile number 9 in Fig. 8.2) versus the radiosonde launched at 14:00 UTC from Hornisgrinde. The solar background is expected to be highest for the case where the distance of the pointing direction of the lidar is closest to the actual position of the Sun. The angle δ (in radians) between two points on a sphere is

$$\delta = \arccos[\cos(\epsilon) \cos(\alpha) \cos(\phi - \beta) + \sin(\alpha) \sin(\epsilon)], \quad (8.3.1)$$

with the angles α and β , the elevation and the azimuth of the Sun, and ϵ and ϕ , the elevation and the azimuth of the scanner, respectively. The azimuth angle is given with respect to north and ranges between 0 and 2π . The elevation angle ranges between 0 and π whereas zenith is at $\pi/2$. According to Fig. 8.6, the mean angular distance to the Sun for a scanner elevation of 72° at azimuth of 291° was about 45° . The closest point to the Sun was found for an elevation of the scanner of 45° (profile number 6, Fig. 8.2) where the angular distance to the Sun was 40° .

Below 2 km ASL, the lidar profile in Fig. 8.5a showed temperatures that were up to 2 K warmer than the radiosonde. While the radiosonde drifted towards east, it penetrated the outer region of a cumulus cloud at around 600 m AGL which was confirmed by observation. Because of shadowing effects below dense clouds and evaporation of the cloud droplets in the cloud's outer region, the environment was potentially cooler along the radiosonde track than in the lidar profile which was measured towards the west at a scan elevation of 72° . Figure 8.4d shows the presence of a well-mixed zone with $d\theta/dz < 0.2$ K/100 m below 2.5 km ASL (≈ 1.3 km AGL) to the west of the cumulus cloud. This unstable zone was likely generated due to the compensating subsidence in the immediate vicinity of the convective cloud.

Figs. 8.5b,c show the vertical temperature profiles of the scans measured from 14:55–16:00 UTC and 16:00–17:05 UTC. The radiosondes launched at 14:00 and 17:00 UTC are shown for comparison. The distance to the Sun was 65° for (b) and 75° in case of (c). The lidar temperature profiles were in very good agreement with the radiosonde measurements. The statistical uncertainties of each profile are shown in Fig. 8.5d. The uncertainties were smaller than 0.8 K up to 3 km altitude AGL. Below the height of 1.2 km AGL, ΔT increased rapidly down to 0.6 km AGL to about 1 K due to the uncertainty of the overlap correction.

In case of the potential temperature field in Fig. 8.3a the uncertainties are less than 1 K for the whole scan and less than 0.5 K for Figs. 8.3b,c. Thus, the uncertainties of the gradient of potential temperature at, e.g., 4 km ASL were 0.7 K/100m, 0.5 K/100m and 0.35 K/100m for Figs. 8.4d–f, respectively.

Figures 8.7a,b show the profiles of statistical uncertainties for the scan measured between 16:00 and 17:05 UTC. The numbers correspond to the elevations of the scan as

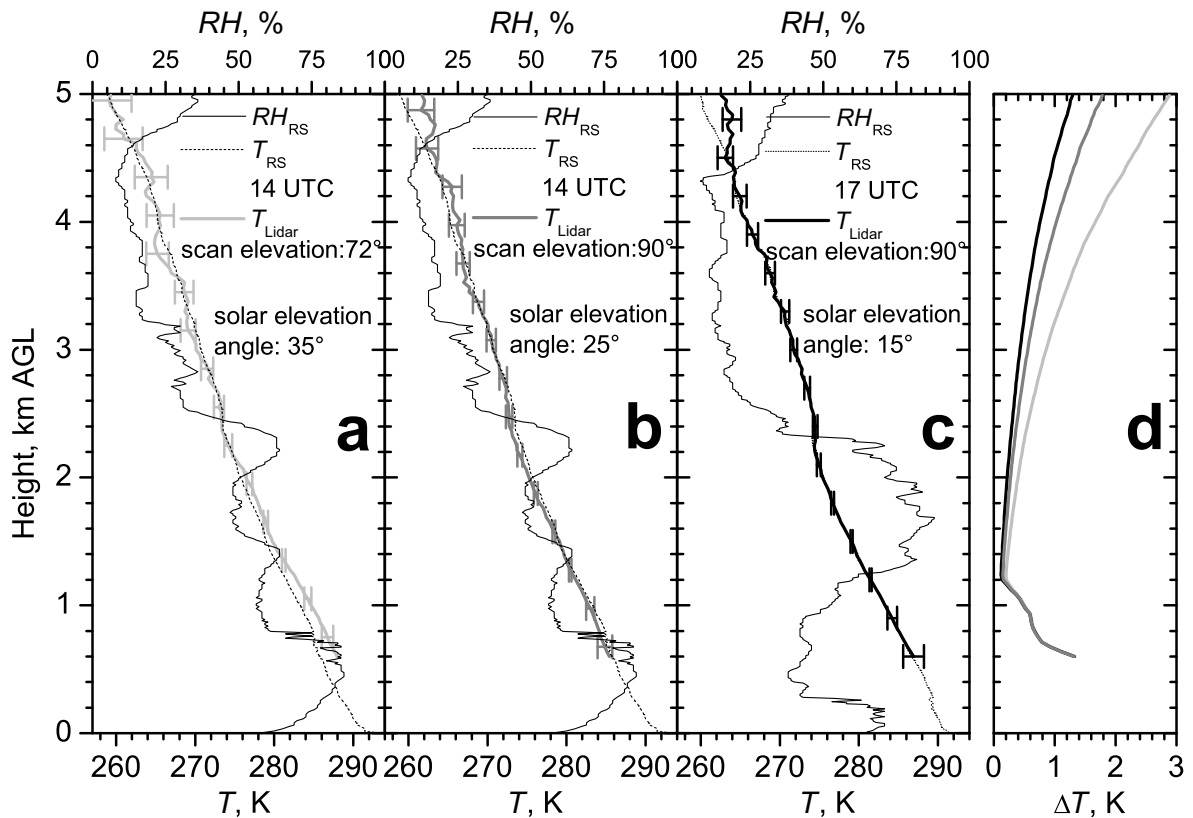


Figure 8.5: (a) Average of 13 profiles measured at a scanner elevation of 72° , each of 13 s integration time giving 169 s. Temperature profiles measured by lidar and radiosonde on 25 August 2007 in the period of 13:50–14:55 UTC on Hornisgrinde in the Northern Black Forest, Germany. The spatial resolution is 37.5 m. A moving average of 300 m was applied to the lidar data. Error bars designate the statistical uncertainties of the lidar data. The radiosonde, included for comparison, was launched at 14:00 UTC from Hornisgrinde. (b): Same as (a) but the lidar profile corresponds to the vertical profile of the scan from 14:55–16:00 UTC. Here, only 9 profiles were incorporated giving 117 s integration time. (c): Same as (a) but the lidar profile corresponds to the vertical pointing profile during the scan measured between 16:00 and 17:05 UTC. The radiosonde shown here was launched at 17:00 UTC from Hornisgrinde. The profile of relative humidity (RH) measured by the radiosondes is shown on the upper axis additionally. (d): Statistical temperature uncertainties of the lidar profiles shown in (a)–(c).

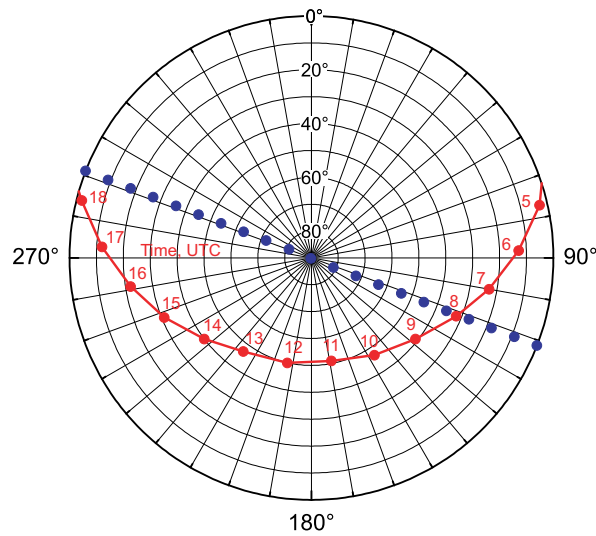


Figure 8.6: Elevation of the Sun on 25 August 2007 on Hornisgrinde during the course of the day. Circles indicate the elevation and radial lines from the center of the plot the azimuthal angle of the Sun. Blue dots mark the pointing directions during the RHI scans (azimuth angle at 291°) that were performed by the lidar. Time is in UTC.

shown in Fig. 8.2. It can be seen that ΔT increased towards lower scan elevations by about 30% from profile 12 to profile 21 and from profile 10 to profile 2. The increasing statistical uncertainties mainly resulted from the denser atmosphere at low elevation angles which in turn led to a higher extinction of the detected signals. Profile 1 was measured horizontally towards the Rhine Valley and showed values of ΔT that were by 40% increased than compared to profile 2. This is explained by a much higher signal extinction due to a higher aerosol load and water vapor concentration that was present. The temperature profiles were corrected for overlap effects below 1.5 km. A correction was suggested by Mattis et al. (2002). This scheme could be simplified since the overlap did not change in time for the measurement example presented here. As proposed by Mattis et al. (2002), the deviation of the vertical lidar profile was calculated for the vertical lidar data measured from 16:00–17:05 UTC and 13:50–14:55 UTC with respect to the closest radiosonde. Because 3 out of 13 vertical profiles in the measurement period between 13:50 and 14:55 UTC were distorted by clouds, those profiles were neglected. The scanning measurements from 14:55–16:00 UTC were not taken into account, since differences in the PBL between the lidar and radiosonde profiles would yield an erroneous deviation. The two functions that were obtained are shown in Fig. 8.8. Finally, the average of both functions was used to correct the temperature in the overlap region on this day for all data shown in Figs. 8.3, Figs. 8.4d–f and Figs. 8.5. The error of the correction was estimated by calculating the difference between the averaged deviation and the individual deviations. Below the height of 600 m AGL, this error increased rapidly and became larger than 0.5% resulting in an increase of temperature uncertainty of more than 1 K just due to the uncertainty of the overlap correction. Thus, systematic effects below 600 m could not be corrected satisfactory by

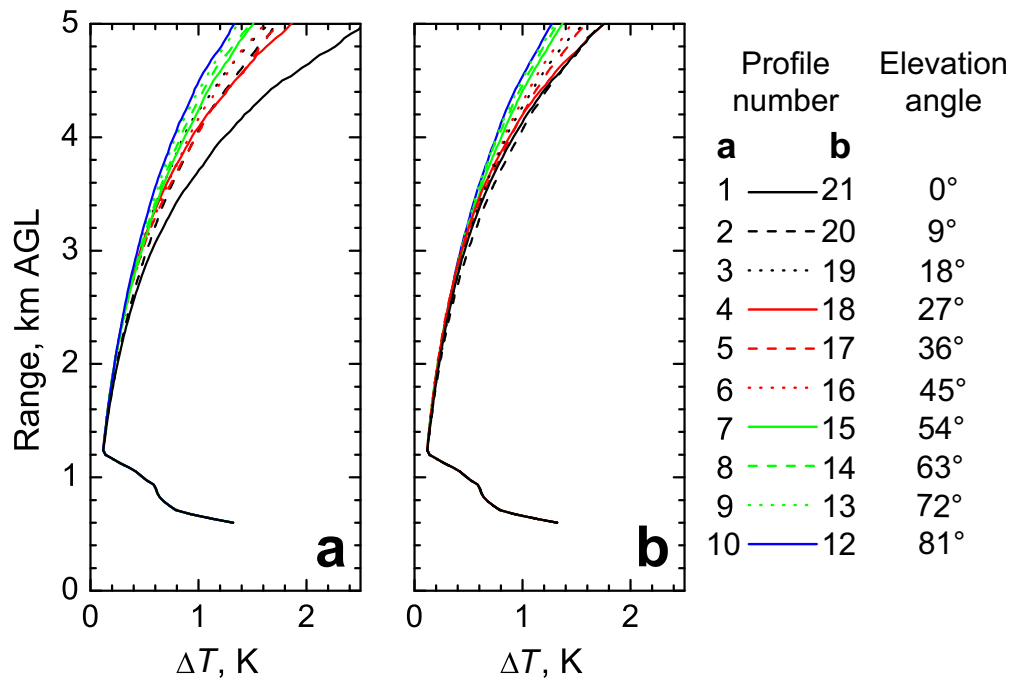


Figure 8.7: 1- σ statistical temperature uncertainties of the lidar profiles measured during the scan from 16:00–17:05 UTC. (a) profiles 1–10 in direction of the Rhine Valley (towards the west) and (b) profiles 12–21 in direction of the Murg Valley (towards the east). The numbers 1–10 and 12–21 correspond to the different elevation angles shown in Fig. 8.2.

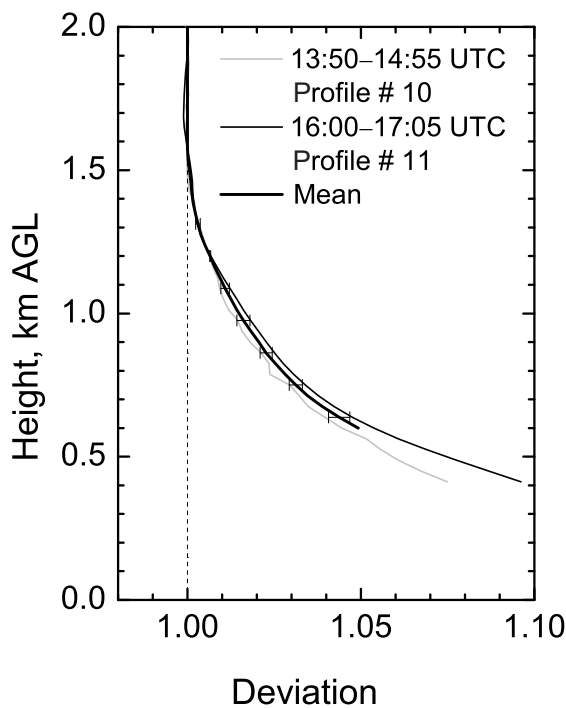


Figure 8.8: Ratio of the lidar-derived temperature to the radiosonde temperature for the lidar measurement performed from 13:50–14:55 UTC at a scan elevation of 81° (profile number 10) and for the vertical pointing measurement from 16:00–17:05 UTC. The average of both functions was used to correct for overlap effects in the lidar temperature measurements on 25 August 2007. Error bars show uncertainties of the overlap correction.

a similar approach. Therefore, the correction was only applied from heights of 600 m upwards.

8.3.2 Temporal and range resolution

The performance of the system was significantly improved compared to the previous field campaign PRINCE in summer 2006. Figures 8.9a,b show the elevation of the Sun and the background signals in the two RR channels on 14 June 2007 between 4:00 and 15:00 UTC. The photon counts per second (cps) of the background were summed up to yield a range resolution of 60 m. Longer gaps between the points that show the vertical pointing data on this day are periods when scanning measurements were performed. Isolated cumulus clouds developed in the vicinity of Hornisgrinde after 10:00 UTC which became denser until 12:00 UTC. The corresponding strong enhancement of the background by a factor of up to 2.5 was caused by diffuse scattering of sunlight on the clouds. For the sake of clarity, it should be mentioned that a few clouds were observed directly above the lidar as well. The profiles containing clouds with cloud bases between 1 and 3 km AGL were excluded in the measurements shown in Figs. 8.9. Figure 8.9c presents the evolution of the statistical temperature uncertainty at heights of 1 km AGL and 3 km AGL with a range resolution of 60 m and 300 m. The temporal resolution of the data points is 1 minute. Between 4:00 and 5:30 UTC the temperature uncertainties increased by up to 50%. During this period, some clouds were observed by the lidar at altitudes between 5 and 8 km AGL which led to an enhanced background signal by more than 50% as can be seen in Fig. 8.9b. The elevation of the Sun changed from 5° to about 57° from 4:00 to 10:00 UTC. Within the same time, ΔT increased by 17% at 1 km AGL from 0.13 K to 0.15 K and 0.3 K to 0.35 K for a spatial resolution of 300 m and 60 m, respectively. The increase was larger at an altitude of 3 km AGL because the SNR becomes lower for increasing height. Therefore, ΔT increased from 0.7 K to 1 K and from 1.5 K to 2.3 K for a range resolution of 300 m and 60 m, respectively. During the cloud events, where the background was higher of about 150%, ΔT increased by 100% at 3 km altitude AGL and by 70% at a height of 1 km AGL. Figure 8.10 shows the time of data acquisition required to achieve a statistical temperature uncertainty of less than 1 K at a certain altitude. These calculations were performed for range resolutions of 60 m and 300 m. The accuracy for daytime temperature profiling was assessed by means of data measured on 14 June 2007 at 9:30–10:00 UTC (thick black lines). The elevation of the Sun was at about 57° in average (see Fig. 8.9a). Data acquired for 1 minute with a range resolution of 60 m resulted in statistical temperature uncertainties of less than 1 K within the lowest 2 km. Daytime temperature profiling up to 3 km height yielded similar uncertainties for integration times of 70 s and a range resolution of 300 m. The nighttime performance was assessed by neglecting the background but using the same lidar measurements. The daylight background dominated over the lidar backscatter above 8 km AGL. Hence, the lidar signals became very noisy and the data was cut here. A simulation of the nighttime performance applying the system efficiency of 6% fitted the experimental results. Temperature uncertainties of less than 1 K are achieved during nighttime up to a range of

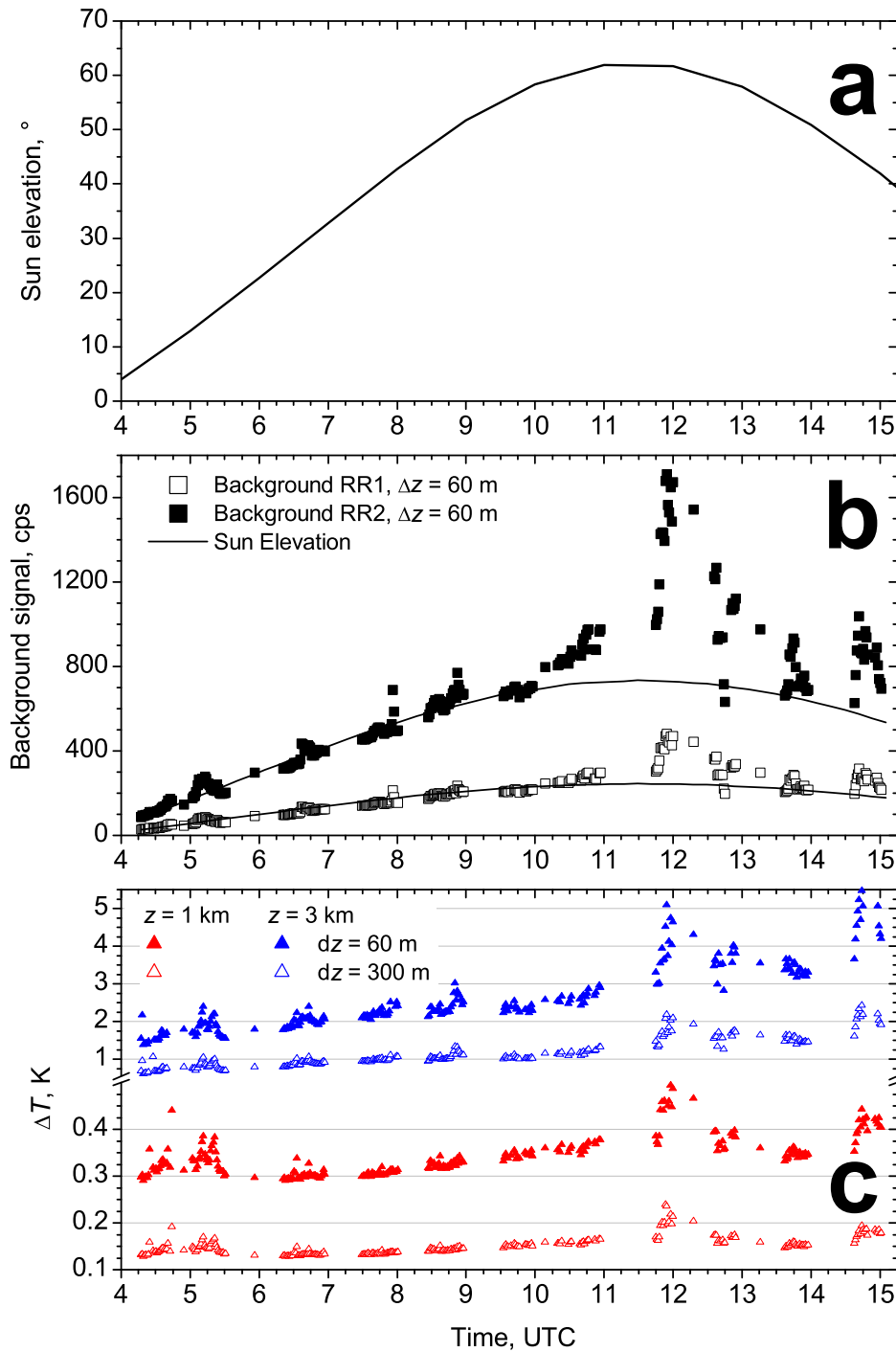


Figure 8.9: (a) Solar elevation angle of the Sun on 14 June 2007 on Hornisgrinde. (b) Background signal in the two RR channels considering a range bin of 60 m length measured on the same day and (c) time series of temperature uncertainties at a height of 1 km AGL and 3 km AGL for a range resolution of 60 m and 300 m and a temporal resolution of 1 minute.

8 km using a temporal resolution of 3 minutes and a range resolution of 300 m. Consequently, to achieve $\Delta T < 1$ K, temperature profiling within the lower troposphere (below 5 km AGL) was feasible within less than 1 minute at a range resolution of 300 m and within 5 minutes using a range resolution of 60 m. Compared to the performance during the PRINCE campaign, the resolution of the UHOH RR lidar could be improved by a factor of about 20 for vertical temperature measurements during day- and nighttime.

Previous studies conducted by Behrendt et al. (2004b) using 355 nm for temperature profiling by RR lidar used data of the RASC lidar system (Shigaraki, Japan) (Behrendt et al., 2002, 2004a) at 532 nm which were scaled to 355 nm. The same RASC data were scaled according to the system parameters of the UHOH RR lidar in Fig. 8.10. It turned out that the integration time needed with the UHOH lidar in order to achieve statistical temperature uncertainties of less than 1 K is only 40% of what was expected by the scaled data.

Also the performance for airborne RR lidar was investigated by Behrendt et al. (2004b) using the data of the RASC lidar. For a flight speed of 500 km/h at a flight level of 15 km ASL, the horizontal resolution was determined with about 10 km that would be necessary to achieve $\Delta T < 1$ K throughout the troposphere with a vertical resolution of 400 m considering a laser power of 15 W at 355 nm and a telescope with primary mirror diameter of 0.4 m. Assuming the same specifications, a horizontal resolution of 4 km is feasible with respect to the presented system performance. With a higher laser power of 25 W, provided by state-of-the-art diode-pumped Nd:YAG lasers (Ostermeyer et al., 2005), even a horizontal resolution of about 2.4 km can be achieved.

Specific observational requirements for regional NWP were formulated by the WMO in a medium-term perspective (2001–2015) (Gustafsson et al., 2001). Observations, e.g., performed with an airborne lidar are important to improve the boundary conditions for NWP in regions where more data are needed, e.g.: over oceans and mountain regions. For tropospheric temperature measurements, an accuracy of 0.5 K, a vertical resolution of 100 m and a horizontal resolution of 3 km are desired. In the lower troposphere, the horizontal and vertical resolution is preferably 1 km and 10 m, respectively, whereas an useful horizontal and vertical resolution already is 10 km and 300 m, respectively.

8.4 Spectral analysis of a high resolved temperature measurement in the boundary layer on 14 June 2007

For studying the turbulent structure in the PBL, it is important to measure turbulent moments. Usually in-situ instruments are used for investigating the turbulent structure in the atmosphere. For temperature this is done by means of platinum thermometers mounted on airborne platforms, e.g., at the research aircraft DO-128 (Corsmeier et al., 2001) and the helicopter-borne turbulence probe Helipod (Muschinski and Wode, 1998; Bange and Roth, 1999; Bange et al., 2002) of the Technical University of Braunschweig, Germany. Airborne sensors can be used to perform flux measurements at different heights and over a large area. Ground-based turbulence stations usually use acoustic

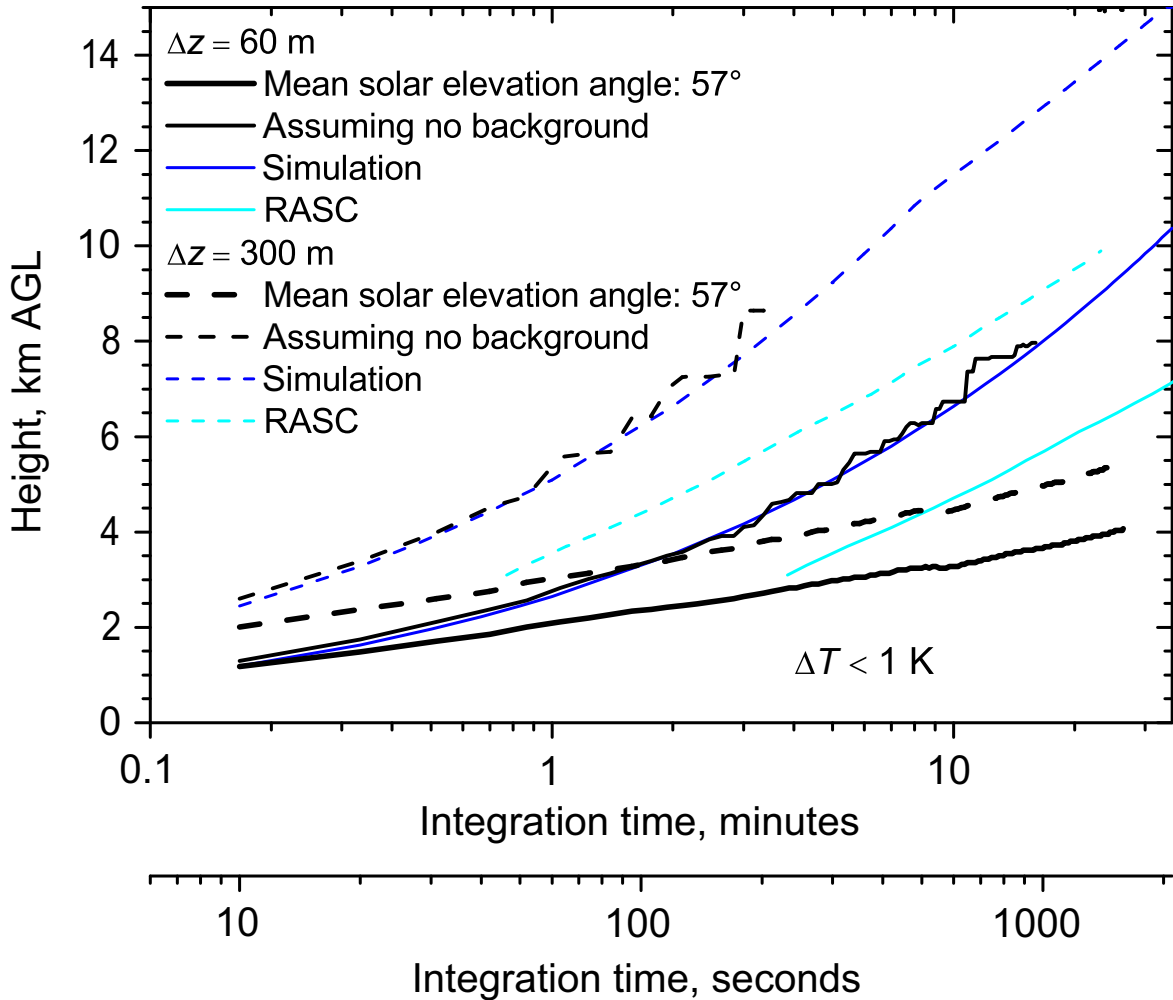


Figure 8.10: Required measurement time to achieve a $1\text{-}\sigma$ statistical temperature uncertainty of less than 1 K for different range resolutions of 60 m and 300 m. The daytime performance was assessed by using the photon-counting data measured between 9:30 and 10:00 UTC on 14 June 2007. The mean solar elevation angle during this measurement period was 57° . Neglecting the background of the same data shows the expected nighttime performance. A simulation of the nighttime measurement performance assuming a system efficiency of 6% fits the experimental results. In addition, the performance estimated from data measured by the RASC lidar (Shigaraki, Japan) (Behrendt et al., 2004b) is shown. The performance of the RASC system obtained at a wavelength of 532 nm with a power of 30 W and with a primary mirror diameter of 80 cm (Behrendt et al., 2002, 2004a) was scaled to the specifications of the UHOH lidar (laser wavelength: 355 nm, laser power: 10 W and telescope diameter: 40 cm).

anemometers that measure with frequencies of 100 Hz and high accuracy. Active remote sensing instruments such as lidar and radar-RASS are the only instruments to measure vertical profiles of the turbulent structure within the PBL. Water vapor DIAL (Senff and Peters, 1994; Kiemle et al., 1997; Wulfmeyer, 1999a), ozone DIAL (Senff et al., 1996) and Doppler wind lidar (Wulfmeyer and Janjić, 2005) were used to analyze turbulent structures in the well-mixed PBL using lidar. The analysis of instrumental noise is important when interpreting higher order moments of such data (Wulfmeyer, 1999b; Lenschow et al., 2000). To the best of my knowledge, there are no publications so far dealing with active measurements of the temperature variance by lidar. This is mainly due to the fact that the required high temporal resolution combined with small measurement uncertainties could not be realized to date.

8.4.1 Temperature variance

Lidar data contain significant instrumental noise which has to be estimated in order to calculate the variance. In general, the SNR can be improved by averaging the signal in time and range, but this in turn reduces the number of resolvable turbulent structures. The variance spectrum and the autocovariance function (ACF) can be used to estimate the variance of a correlated variable. The variance spectra $S(f)$ of a correlated variable is calculated by a Fourier transformation of the variable's fluctuations. The signal variance σ_s^2 and the noise variance σ_n^2 can be assumed to be uncorrelated. The variance spectrum gives an estimation of the noise contribution to the measured signal which is found at the highest frequency, the Nyquist-frequency f_ν , that is resolved by the time series. The product $S(f) \times f_\nu$ yields the noise variance. The atmospheric temperature variance yields

$$\sigma_s^2 = \sigma_{sn}^2 - \sigma_n^2, \quad (8.4.1)$$

with the variance including the noise contribution σ_{sn}^2 .

In the following text, a brief description of the application of the ACF is given according to the method and notation presented by Lenschow et al. (2000).

Considering a time series of temperature fluctuations $T'(t)$ which is contaminated by uncorrelated random noise $\epsilon(t)$, both with a mean of zero, the measured signal is $T'(t) + \epsilon(t)$. T'_τ is the lagged temperature fluctuation at lag τ and is defined as

$$T'_\tau \equiv T'(t + \tau). \quad (8.4.2)$$

The second-order ACF is defined as

$$M_{11}(\tau) \equiv \frac{1}{\mathbb{T}} \int_0^{\mathbb{T}} [T'(t) + \epsilon(t)][T'(t + \tau) + \epsilon(t + \tau)] dt, \quad (8.4.3)$$

which yields

$$M_{11}(\tau) = \overline{(T' + \epsilon)(T'_\tau + \epsilon_\tau)} = \overline{T'T'_\tau} + \overline{T'\epsilon_\tau} + \overline{T'_\tau\epsilon} + \overline{\epsilon\epsilon_\tau}, \quad (8.4.4)$$

where \mathbb{T} is the length of the time series. At the zero lag $\tau = 0$ the second-order autocovariance yields

$$M_{11}(0) = \overline{T'^2} + 2\overline{T'\bar{\epsilon}} + \bar{\epsilon}^2 . \quad (8.4.5)$$

Because ϵ is uncorrelated with T' , $\overline{T'\bar{\epsilon}} = 0$ and $\bar{\epsilon} = 0$, Eq. (8.4.4) and (8.4.5) result in

$$M_{11}(\tau) = \overline{T'T'_\tau} , \quad (8.4.6)$$

$$M_{11}(0) = \overline{T'^2} + \bar{\epsilon}^2 . \quad (8.4.7)$$

The signal variance and the noise variance are both contained in the zero lag value, whereas for $\tau \neq 0$ there is no contribution from the uncorrelated noise. The noise variance is

$$\bar{\epsilon}^2 = \Delta M_{11} \equiv M_{11}(0) - M_{11}(\tau \rightarrow 0) . \quad (8.4.8)$$

$M_{11}(\tau \rightarrow 0)$ is the extrapolated autocovariance to zero lag which provides the real contribution of the temperature variance $\overline{T'^2}$. One method for the extrapolation is suggested to be the inertial subrange hypothesis (Monin and Yaglom, 1979) leading to the ACF

$$\widetilde{M}_{11}(\tau) = \overline{T'^2} - C\tau^{2/3} . \quad (8.4.9)$$

C is a parameter that contains the turbulent eddy dissipation and the scalar variance dissipation and $\widetilde{M}_{11}(\tau)$ is the noise-free ACF. $M_{11}(\tau \rightarrow 0)$ is found by fitting the 2/3 power law to the first few lags of the second-order ACF. A rather simple solution is provided by the assumption that $M_{11}(1)$ equals the signal variance. However, this usually leads to an underestimation of $\overline{T'^2}$ (Kiemle et al., 1997; Lenschow et al., 2000). The integral time scale of $\overline{T'^2}$ is given by

$$\mathcal{T}_{11} = \frac{1}{\overline{T'^2}} \int_0^\infty \widetilde{M}_{11}(\tau) d\tau , \quad (8.4.10)$$

with the second-order autocovariance $\widetilde{M}_{11}(\tau)$ of $T'(t)$. Using the integral scale, the sampling error $\Delta\overline{T'^2}_s$ for the atmospheric variance is specified (Lenschow and Kristensen, 1985) as follows:

$$\Delta\overline{T'^2}_s \simeq 2\overline{T'^2} \sqrt{\frac{\mathcal{T}_{11}}{\mathbb{T}}} . \quad (8.4.11)$$

The instrumental error for the atmospheric variance, with the number of observations N , is (Lenschow and Kristensen, 1985)

$$\Delta\overline{T'^2} \simeq \overline{T'^2} \sqrt{\frac{4}{N} \frac{\bar{\epsilon}^2}{\overline{T'^2}}} . \quad (8.4.12)$$

8.4.2 Results

A time series of temperature for the case of a well-mixed PBL over a mountain peak measured during IOP 4a on 14 June 2006 between 9:32 and 9:59 UTC was selected for this study.

The synoptic pattern was characterized by a cut-off low located over the Atlantic Ocean south of Ireland. The COPS region was influenced by an upper level ridge, present over Italy, which slowed down the eastward propagation of a weakening cold front over central France. A southwesterly flow in the lower troposphere was prevailing during the whole day.

The surface observations from the meteorological station by IMK-FZK installed on Hornisgrinde are shown for this day between 6:00 and 12:00 UTC in Fig. 8.11. No mesoscale disturbances, e.g., frontal systems or upstream convergence lines, occurred during this period as indicated by the constant air pressure. Only a slight increase until 9:00 UTC by less than 0.3 hPa was observed. The temperature increased due to insolation from 15°C at 6:00 UTC to 20°C at 12:00 UTC. The relative humidity decreased from 75% to 55% within that period. The wind direction close to the ground veered from south to west between 7:30 UTC and 8:00 UTC. The wind speed exhibited rather weak variations with values between 2 and 4 m/s.

The radiosonde launched at 8:00 and 11:00 UTC is shown in Fig. 8.12a. The lidar temperature measurements obtained during 30 minutes time intervals at 7:45 UTC, 8:40 UTC and 9:45 UTC are also shown. Lidar data are shown for heights above 700 m (7:45 and 8:45 UTC) and 450 m (9:45 UTC) relying on the same overlap function for both RR channels. Only small differences are evident between the potential temperature profiles measured by the radiosonde above 700 m AGL. The radiosonde launched at 11:00 UTC showed decreasing θ -values up to about 700 m AGL referring to a well-mixed PBL. The lidar measurements observed a cooling of about 2 K between the first profile at 7:45 and the latest at 9:45 UTC in a height of around 900 m AGL. The temperature profiles showed similarly decreasing values above 1000 m AGL. At 9:45 UTC the lidar measured a pronounced temperature lid at 900 m AGL. Consequently, the radiosonde ascent at 11:00 UTC showed a lid of similar strength at an altitude between 1.3 and 1.4 km AGL. The atmosphere was rather dry during the whole morning with relative humidity lower than 70% and smallest values of around 50% below 500 m AGL as evinced by the radiosonde measurements. Figures 8.12b and c show data of the Doppler wind lidar on top of Hornisgrinde. The profiles of wind speed and wind direction were derived by a VAD (Velocity Azimuth Display) algorithm (Browning and Wexler, 1968) applied to the lidar data. The wind speed increased from 5 m/s at the ground to 15 m/s at 2 km AGL. The wind speed remained constant within 1–2 m/s over the whole measurement period. Between 6:00 and 9:00 UTC the prevailing wind direction was southwest. After 10:00 UTC the wind direction had a southerly component between 200 m and 1.6 km AGL.

Figure 8.13a shows the particle backscatter coefficient measured by the RR lidar. Intensive turbulent structures were observed below 1 km AGL within a developing PBL on Hornisgrinde. From this data, a mean PBL top height of 710 m was determined by

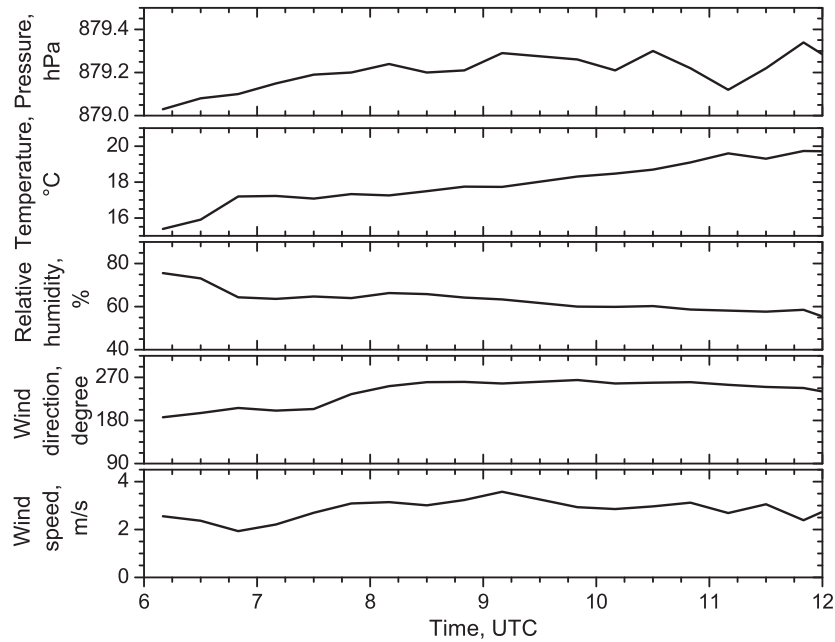


Figure 8.11: Measurements of the meteorological station of IMK-FZK on top of Hornisgrinde on 14 June 2007 from 6:00–12:00 UTC. Air pressure, temperature and relative humidity were measured at 3.3 m above ground. Wind direction and wind speed were measured at 3.9 m above ground. The data were stored in a 20 minutes interval.

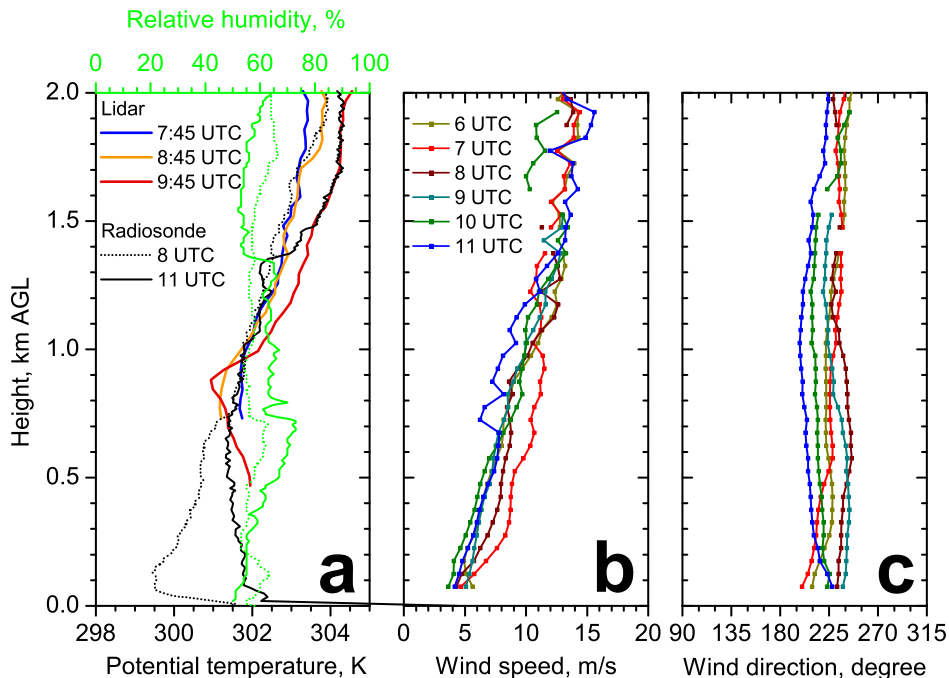


Figure 8.12: (a) Potential temperature and relative humidity profiles measured by the radiosonde launched at 8:00 UTC and 11:00 UTC on 14 June 2007 and profiles of potential temperature measured by the UHOH RR lidar. The lidar data were averaged for 30 minutes. The range resolution is 37.5 m. The lidar data were smoothed with a moving average of 75 m. ΔT is smaller than 0.2 K for all lidar profiles. (b) Wind speed and (c) wind direction derived from measurements of the Doppler wind lidar operated by IMK-FZK on Hornisgrinde. The range resolution is 50 m. The profiles calculated at every full hour are shown here.

applying the Haar-wavelet transform method (Davis et al., 2000; Cohn and Angevine, 2000; Pal, 2009). The temperature time series is shown in Fig. 8.13b with a temporal resolution of 10 s and a spatial resolution of 37.5 m. A 75 m moving average was applied to the signals before calculating the temperature. The mean PBL top height was found to be at about 900 m according to the profile of potential temperature shown in Fig. 8.12a (resulting from the temporal average of the temperature data in Fig. 8.13b). In fact, it was rather complicated to estimate the PBL height z_i for the selected case. Therefore, the profiles are not normalized by z_i .

Below 450 m AGL the lidar data were distorted by overlap effects. Thus, only heights above 450 m were analyzed. Strong upward motions at 9:40 UTC and around 9:47–9:50 UTC led to cloud formation at heights between 800 and 1000 m AGL which influenced the temperature data at the respective time because the strong extinction led to increased temperature uncertainties at these height levels. Furthermore, a correction of the temperature data was performed in order to remove elastic signal intrusion (see Sect. 5.2.3).

The power spectra presented in Fig. 8.14 were calculated following the technique described in Senff et al. (1996). The same technique was applied by Wulfmeyer (1999a,b) and Wulfmeyer and Janjić (2005) for analyzing turbulent processes in water vapor DIAL data and Doppler wind lidar measurements.

Figure 8.14 shows the spectra of the temperature fluctuations. The spectra were normalized with respect to the total variance in the measurement interval and finally smoothed by using a five-point moving average. According to the $f^{-5/3}$ power law (Kolmogorov, 1941) a roll-off for frequencies higher than 0.004 Hz was present for all temperature spectra indicating the transition zone between the large turbulent eddies and the small viscous eddies. Most of the energy was available at a frequency of 0.003 Hz. Therefore, the eddies contributing most to the variability of the atmosphere had time scales of about 5 minutes. The $-5/3$ slope was not observed for frequencies >0.015 Hz at 468.75 m height AGL and >0.01 Hz at 731.25 m height AGL. The noise contribution increased significantly up to 1000 m AGL. Maximum temperature uncertainties of about 0.1 K would be necessary to capture the inertial subrange up to the Nyquist frequency of 0.05 Hz for the measurement example presented here. The noise variance was determined by averaging the high-frequency end from 0.04–0.05 Hz of the spectrum. ΔT increased from 470 m to 730 m AGL from 0.41 K to 0.55 K.

The second-order ACF was calculated for each height level of the data shown in Fig. 8.13b. Figure 8.15 shows the ACF around the zero lag for three different heights. The variance at $\tau = 0$ increases with height mainly due to the contribution of signal noise. To estimate the noise variance, the $2/3$ power law fit (applied to the first 9 lags of the ACF) according to Eq. (8.4.9), the first-lag approximation and the spectral method were applied as shown in Fig. 8.16. It should be mentioned here that all techniques show similar results. There is no reason to believe that one technique is more accurate than the other.

The signal noise increased fast from around 0.5 K at 500 m to 0.9 K at 1000 m AGL. This is consistent with the result of the Poisson statistics which is shown for comparison. The integral scale \mathcal{T}_{11} is shown in Fig. 8.17. \mathcal{T}_{11} was estimated from the maximum

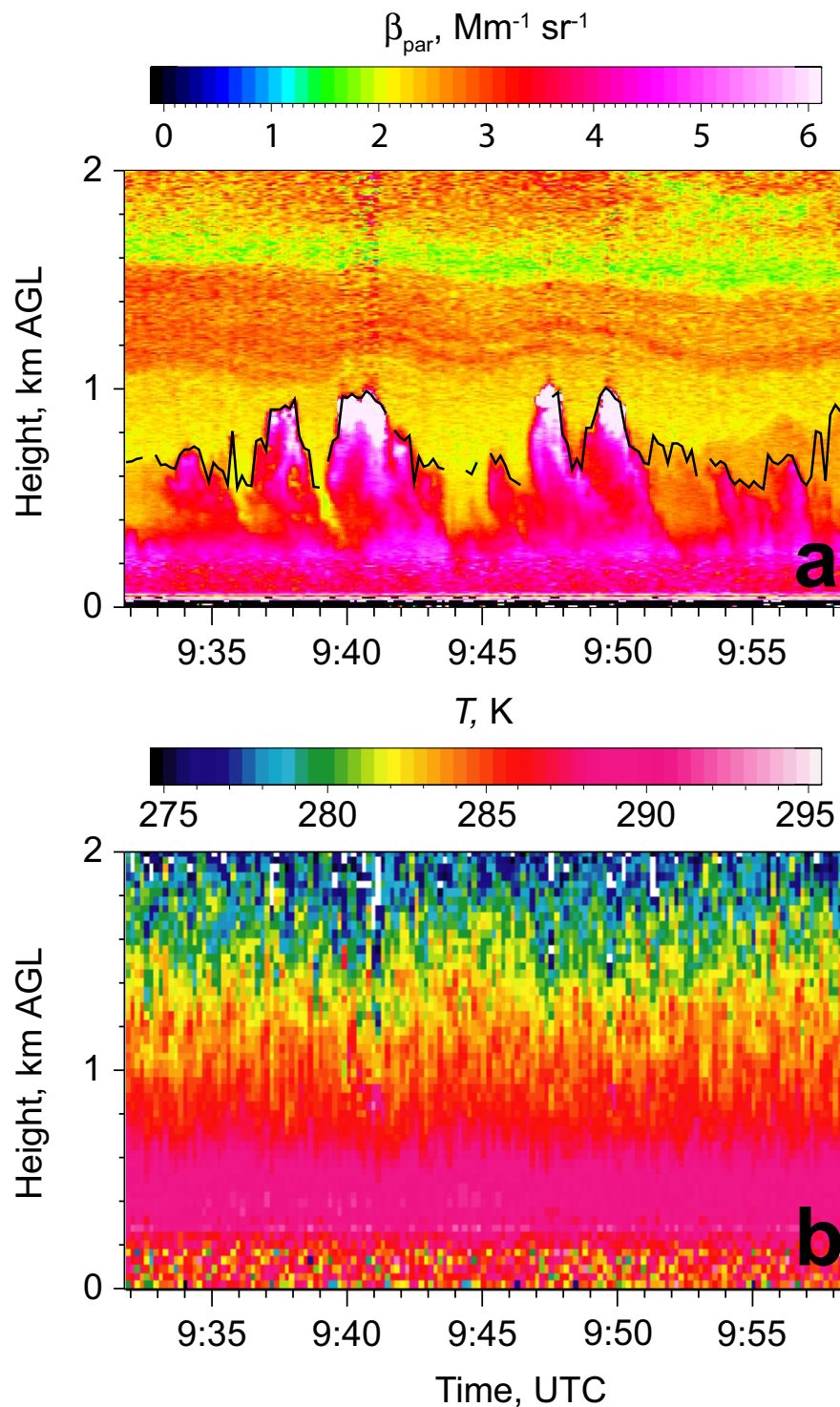


Figure 8.13: (a) Time-height cross section of backscatter coefficient at 355 nm for the measurement period 9:32–9:59 UTC on 14 June 2007 on the mountain peak Hornisgrinde. The range resolution is 3.75 m and the temporal resolution is 10 s. The PBL height derived by the Haar-wavelet transform method of the same data is overlaid. (b) Time-height cross section of the corresponding temperature data with a temporal resolution of 10 s and a range resolution of 37.5 m. A moving average of 75 m was applied to the data.

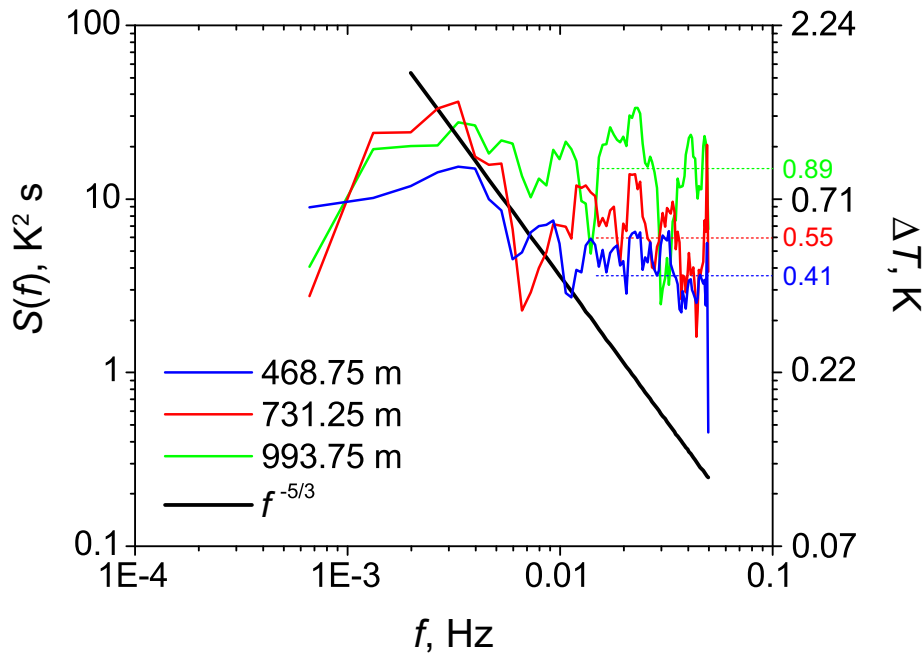


Figure 8.14: Power spectra of temperature fluctuations obtained from the temperature data shown in Fig. 8.13b at 468.75 m, 731.25 m and 993.75 m AGL. The resolution of the data for the calculation of the spectra is the same as in Fig. 8.13b. All spectra are normalized to the total variance in the measurement interval. Finally, the spectra were averaged using a five-point moving average. The $-5/3$ slope of the inertial subrange is plotted. The noise level at higher frequencies (0.04–0.05 Hz) yields the temperature uncertainty which is shown on the right axis.

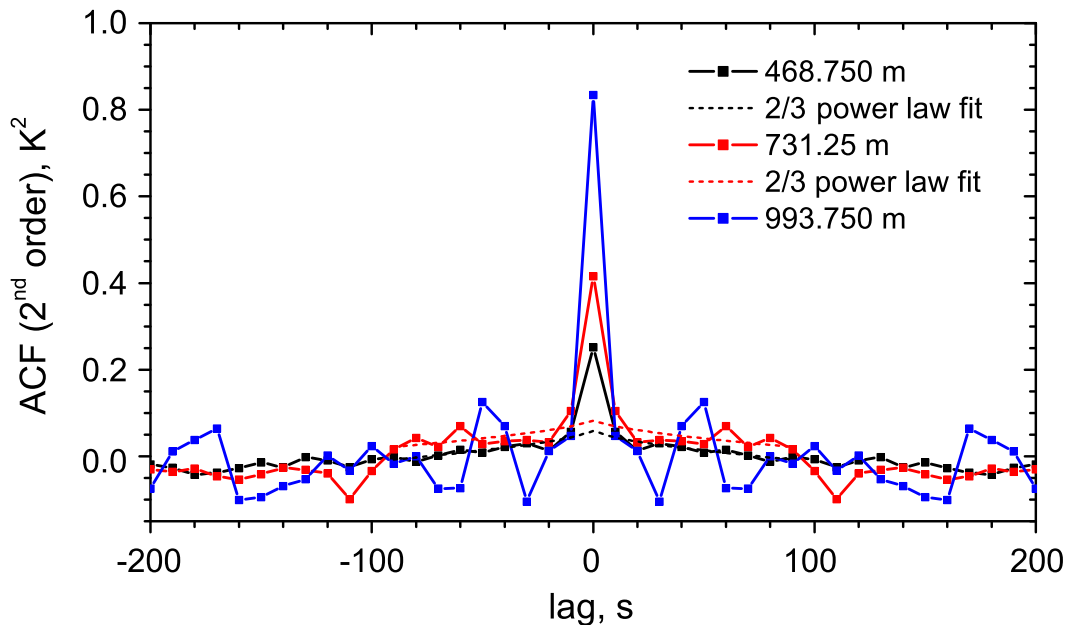


Figure 8.15: The second-order ACF around the zero lag obtained from the temperature data shown in Fig. 8.13b at 468.75 m, 731.25 m and 993.75 m AGL. The strong increase of the total variance at zero lag is mainly due to enhanced temperature noise variance. The extrapolation according to the $2/3$ power law fit is shown for the ACF at 468.75 m and 731.25 m AGL (dotted lines).

of the integral given by (8.4.10). The uncorrected profile shows values that roughly correspond with the temporal resolution of the lidar data. The corrected profile using the first-lag approximation and 2/3 power law fit yielded comparable results. The integral scale was found to be about 50–100 s up to ≈ 750 m AGL with a minimum of 20 s at 800–900 m AGL. This implies that at larger altitudes only a few data points were contained within the inertial subrange.

Figure 8.18 shows the temperature variance profiles obtained by applying the first-lag approximation and the 2/3 power law fit. The uncorrected profile of $M_{11}(0)$ is displayed additionally. The sampling error (Eq. (8.4.11)) and the noise error (Eq. (8.4.12)) are shown for the profile of the 2/3 power law fit. The instrumental noise has the largest contribution accounting for an error of up to 20% in the variance profile between 800–900 m AGL, whereas the sampling error contributes with about 15% to the error. The variance in a well-mixed PBL is largest in the entrainment zone. A small maximum was present at 730 m AGL being likely linked to the entrainment region. A secondary maximum was present at 850 m AGL.

It is not possible to perform a qualitative analysis of the measurement example presented here. Since the measurement was carried out on a mountain ridge, the assumption of Taylor's frozen-field hypothesis (Taylor, 1938) is considerably limited. Taylor's simplification is useful when turbulent eddies evolve with a timescale longer than the time it takes the eddy to be advected past the sensor (Powell and Elderkin, 1974). For the case presented here, the development of the turbulent eddies was strongly influenced by the orography as the depth of the well-mixed layer is not homogenous. More measurement examples are necessary to investigate the turbulent structure of the PBL in complex terrain. The understanding of the exchange between the PBL and the free troposphere is essential for the improvement of weather forecast models as well as climate models. Available boundary layer parametrization schemes used in operational state-of-the-art forecasting models show an insufficient performance to correctly predict, e.g., temperature, wind speed, wind direction and precipitation, in mountainous terrain (Bright and Mullen, 2002; Berg and Zhong, 2005; Schwitalla et al., 2008). This is mainly due to the large-scale humidity convergence and turbulent fluxes of latent heat in the PBL that are not well represented in the model parametrization (Hasel, 2006).

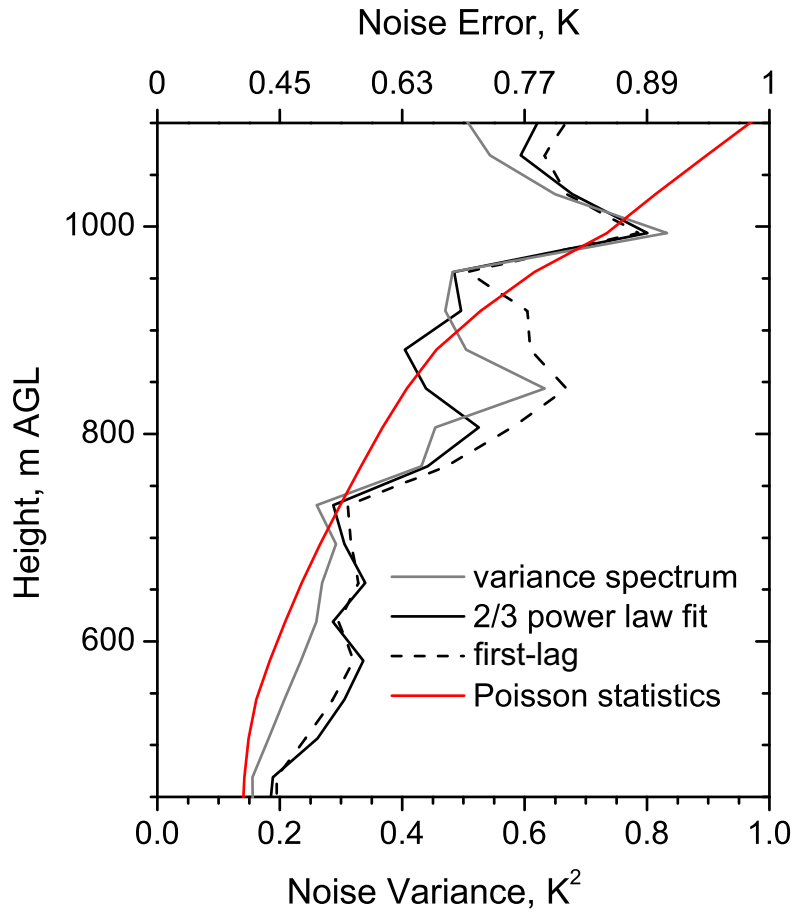


Figure 8.16: Profiles of noise variance derived by the variance spectrum, the 2/3 power law fit and the first-lag approximation. For comparison, the resulting temperature uncertainty calculated by applying Poisson statistics to the photon counting data is shown additionally.

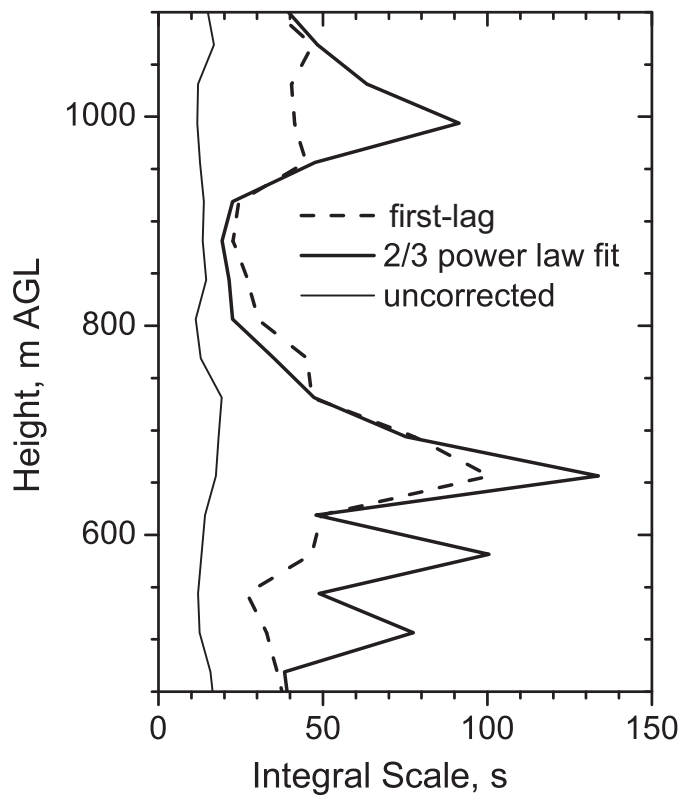


Figure 8.17: Integral scale of the temperature fluctuations as obtained with two different noise corrections: the first-lag assumption and the 2/3 power law fit. The uncorrected profile is also shown.

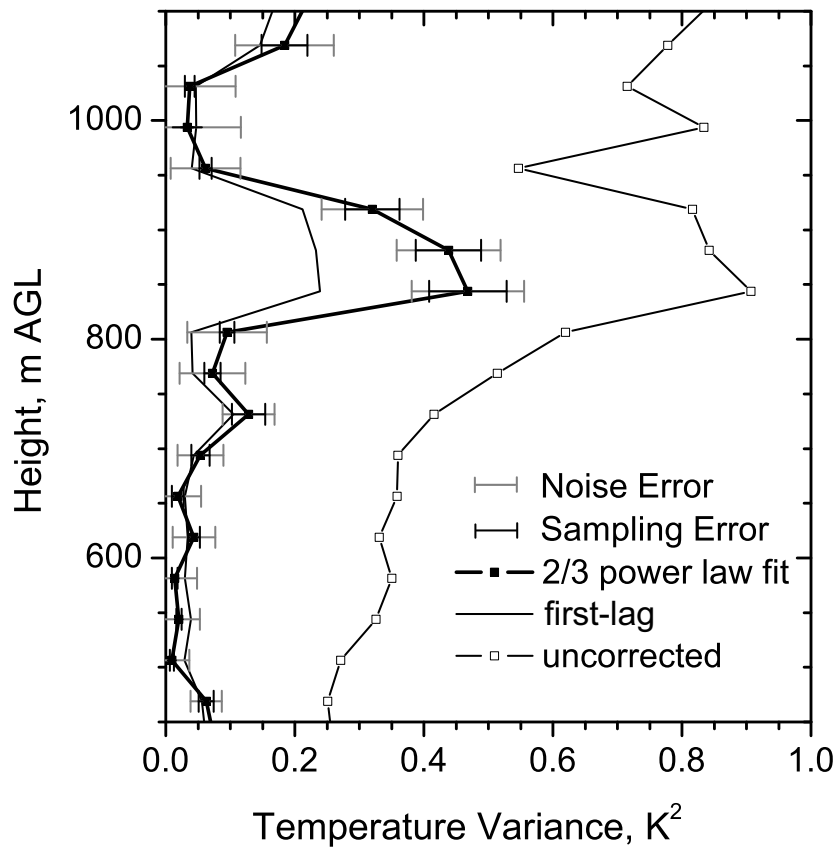


Figure 8.18: Temperature variance profiles for the measurement period 9:32–9:59 UTC on 14 June 2007 on the mountain peak Hornisgrinde retrieved by applying the first-lag assumption and the 2/3 power law fit. The uncorrected profile is shown in addition. Error bars due to instrumental noise and the sampling statistics are shown on the 2/3 power law fit curve.

Chapter 9

Conclusion and outlook

Within this thesis, a scanning RR lidar for daytime temperature measurements was developed. This instrument shows higher performance than any other existing system and, thus, allows to bring new insights into lower tropospheric processes. It is based on the existing eye-safe scanning aerosol lidar of UHOH which was upgraded by two RR channels using the frequency tripled radiation of a Nd:YAG laser. The sequential channel mounting of the interference filter-based polychromator yields high efficiency in separating the signals. The CWL's of the filters can be tuned which allows to optimize the system efficiency for daytime or nighttime background levels, respectively, by selecting the tilting angles.

Detailed filter simulations were performed to optimize the RR filter parameters for both high nighttime and daytime performance in the lower troposphere. The choice of optimal filter widths and central wavelengths yielded statistical uncertainties that were reduced by up to 30% for daytime measurements compared to the previous system at 355 nm of Di Girolamo et al. (2004). This is equivalent to a PAEP improvement by a factor of 1.8.

The system performance was suffering in 2006 due to a low PAEP caused by a degraded silver coating of the laser bending mirrors and the scanner mirrors. After recoating these mirrors, the PAEP yielded 100 mW m² which is in accordance to an increase by a factor of up to 22 compared to the deployment in summer 2006 during the PRINCE campaign. This led to a significant advancement of the measurement capability during the COPS campaign in 2007. The statistical temperature uncertainty ΔT depends on the strength of the background signal. Even in unfavorable conditions ΔT was typically less than 1 K within a range of 3 km for integration times of 169 s in each pointing direction with 300 m moving average. Thus, within one hour 21 different elevation angles were covered. With a very high temporal and spatial resolution of 10 s and 37.5 m, respectively, the lidar resolves also turbulence in the well-mixed PBL with statistical uncertainties of only 0.41 K at 470 m AGL. During nighttime, temperature uncertainties of less than 1 K are achieved up to a range of 8 km using a temporal resolution of 3 minutes and a range resolution of 300 m.

The suppression of the elastically scattered light in the Raman channels showed to be high enough to keep the temperature measurements undisturbed for low to moderate aerosol loads present in the observed atmosphere. Backscatter ratios like they occurred in clouds led to systematic errors. These can be corrected without any additional assumptions because the backscatter ratio is measured simultaneously. This correction results in an increase of the statistical uncertainty of the measurement, e.g.,

a backscatter ratio of 27 yields an increase of $(\Delta T)_{\text{leakage}}$ smaller than 0.04 K.

The first temperature measurements were carried out at the campus of UHOH in March 2006. A noontime temperature measurement showed a very good correlation between the PBL height that was derived by the range square corrected signal and by the temperature gradient of 1800 m and 1810 m, respectively. The temperature gradient at the PBL top varied between -2 and -6 K/km while the height of the PBL varied between 1.7 and 2 km AGL.

From 6 July till 20 July 2006, the lidar was deployed on the mountain peak Hornisgrinde (1161 m ASL) in the Northern Black Forest in southwest Germany during the field experiment PRINCE. The aim of this campaign was to investigate the processes that favor deep convection in complex terrain. Different measurement strategies were developed to probe the atmosphere before convection was initiated and during the mature phase where rain dominated the scenario. The pre-convective conditions were sensed by the UHOH RR lidar and the collocated Doppler wind lidar of IMK-FZK. During the convective period, two radar instruments were used and radiosondes were launched directly in the vicinity of the convective cells by mobile teams. An aircraft, the DO-128 of the Technical University of Braunschweig, Germany, performed different flight patterns and measured wind speed, temperature and humidity at different flight levels within the lowermost 3 km AGL.

A first example of a scanning nighttime temperature measurement by lidar was presented. During this measurement, a temperature inversion with dT/dz of $+5$ K/km was observed above Hornisgrinde. The development of a stable layer was confirmed by the temporal evolution of the vertical temperature profiles, measured by the lidar. The inversion was also existing on the lee side of the mountain and was less pronounced on the luv side.

During the international field experiment COPS, the lidar was deployed at the same site from June to August 2007. The objective of the COPS experiment is to advance the quality of forecasts of orographically-induced convective precipitation by 4D observations and modeling of its life cycle. A large suite of state-of-the-art remote sensing systems, ground-based and airborne were combined with in-situ instruments. A transect of three measurement sites (supersites) was established through the Northern Black Forest. Two additional supersites were located in the French Vosges mountains and on the east side of the Black Forest near Stuttgart, Germany, respectively. The UHOH lidar was deployed together with the same instruments as during the PRINCE campaign at supersite Hornisgrinde. In addition, the scanning water vapor DIAL of UHOH, the scanning microwave radiometer of IMAA-CNR, TARA of IRCTR and a container for in-situ aerosol measurements of the University of Manchester, UK. Furthermore, in-situ sensors such as energy balance stations, automatic weather stations and soil moisture sensors were installed. The RR lidar performed measurements over three months from 1 June until 31 August 2007. The lidar was operated during more than 250 hours and took measurements on 33 days (of which were 27 intensive observation periods). 175 collocated radiosonde launches are available for intercomparisons with the lidar data.

An example for the performance of the RR lidar during COPS was presented. Three

consecutive temperature and aerosol scans on 25 August 2007 covering 3 hours of measurement showed the development of the temperature and particle backscatter coefficient in the vicinity of Hornisgrinde during the afternoon until early evening on 25 August 2007. During the 3 hours period, the PBL subsided from 2 km ASL to about 1 km ASL to the west and to 1.5 km ASL close to the mountain peak. In the last hour, a region with constant potential temperature was observed that stretched towards the ground indicating downward mixing of air within a range of 1 km to the east of Hornisgrinde. Furthermore, an aerosol layer with particle backscatter coefficients up to $2.5 \text{ Mm}^{-1} \text{ sr}^{-1}$ was advected at 2.5–3.5 km ASL while a gradient of potential temperature close to $1 \text{ K}/100 \text{ m}$ and $\approx 0.4 \text{ K}/100 \text{ m}$ showed a rather stable stratification at 3.5–4 km ASL and 2.5–3 km ASL, respectively.

The high performance of the UHOH RR lidar allowed to resolve the temperature variance within the well-mixed PBL on Hornisgrinde. The measurement was restricted by instrumental noise which accounted for an error of up to 20% in the variance profile between 800 and 900 m AGL. Here the temperature variance yielded 0.4 K^2 . It was shown that the analysis of statistical temperature uncertainties derived by Poisson statistics and the spectral analysis matched well.

Even though high performance was reached by the latest state of the lidar presented in this thesis, there is a clear perspective for future improvement. Diode pumped Nd:YAG lasers with a power of up to 25 W at 355 nm are available today (Ostermeyer et al., 2005). In combination with new photomultiplier tubes that are now available with quantum efficiencies as high as 40%, the power efficiency product could be increased by a factor of 5. Furthermore, the system efficiency can be improved by a factor of 2 for pure vertical measurements unmounting the scanner unit. To start with the temperature measurements at low range, we selected for the measurements presented here a RFOV of 0.75 mrad. A decrease of the RFOV would significantly improve the daytime measurement performance but at the same time the minimum range of partial overlap would be increased. By halving the field stop diameter, the daylight background is already reduced to 25%.

In future it is planned to use the capability of the system for scanning measurements in the stable nocturnal and well-mixed daytime PBL. With the aforementioned system improvements, the development of free tropospheric temperature lids can be investigated in more detail. Furthermore, the noise error for measurements of turbulent moments (e.g.: temperature variance, skewness and kurtosis) will be reduced.

Another future application is to couple the UHOH RR receiver to an airborne platform. So far, no airborne Raman lidar with the capability for range resolved temperature measurements exists. Calculations for airborne RR lidar were performed by Behrendt et al. (2004b). They used lidar data of the RASC system (Shigaraki, Japan) at 532 nm which was scaled to 355 nm. These results were related to that of the UHOH RR lidar. Thus, using a laser which provides a power of 15 W at 355 nm and a telescope with primary mirror diameter of 0.4 m it can be stated that tropospheric temperature measurements with a horizontal resolution of about 4 km, a vertical resolution of 400 m and $\Delta T > 1 \text{ K}$ can be achieved, considering a flight speed of 500 km/h at a flight level of 15 km ASL. Therefore, investigations of many atmospheric processes that could

not be performed so far would become possible, e.g.: tropopause foldings, pre-frontal convergence zones, frontal zones and gravity waves. It was shown that the resolution of such a system can be expected to be high enough within the troposphere fulfilling the observational requirements specified by the WMO (Gustafsson et al., 2001).

At NASA GSFC, the Raman Airborne Spectroscopic Lidar has been developed for measurements of water vapor, carbon dioxide and aerosols which already performed a demonstration experiment on ground (Whiteman et al., 2007). A first example of airborne measurements of water vapor and aerosols with a horizontal resolution of 5 km and 300 m, respectively, and a spatial averaging between 30 and 150 m yielding random errors of about 10% was presented just recently by Whiteman et al. (2008).

Also on HALO (High Altitude and Long Range Research Aircraft) a receiver for airborne RR temperature measurements is planned at UHOH. The RR lidar is intended to be used simultaneously with the DLR water vapor DIAL during the demo mission NEPTUN in 2009/2010. The focus shall be on the investigation of cyclogenesis in the Western Mediterranean causing high impact weather. A range of highly interesting synergetic variables would become available, e.g., equivalent potential temperature, relative humidity, atmospheric stability, CAPE and CIN could be sensed continuously.

Appendices

Appendix A

Optimizing filter parameters

A.1 Gaussian filter curves

For selecting ideal filter parameters in terms of filter width, a modified Gaussian curve was used to simulate the signal extraction out of the anti-Stokes branch. The function is defined by

$$f(\lambda) = A \exp \left[- \left(\frac{2(\lambda - \lambda_{\text{CWL}}) B}{\Delta\lambda_{\text{FWHM}}} \right)^4 \right], \quad (\text{A.1.1})$$

with λ_{CWL} the CWL at the peak transmission A and $\Delta\lambda_{\text{FWHM}}$ the filter width. B describes the shape of the function and was chosen in a way that the resulting curve approximates the transmission curve of multi-cavity interference filters (in our case $B = \sqrt[4]{\ln 2}$, see Figs. 4.5a,b). The characteristics of this curve include steep edges and an idealized transmission of 100% ($A = 1$).

The simulations aimed at optimizing the bandwidth of the filters. For this purpose $\Delta\lambda_{\text{FWHM}}$ was changed between 0.05 nm and 0.8 nm using filters of the same FWHM and also filter pairs of different FWHM for the channels RR1 and RR2. In these calculations ideal conditions were assumed which means that the incident light onto the filters is non-divergent and that the individual filter curves are not overlapping. Figures A.1a–e show the results for three different filter pairs of equal bandwidth and for two filter pairs of different bandwidth for each channel. While these are the results without background the same is shown in Figs. A.1f–j with a background signal of $S = 1$ according to Eq. (4.1.8). Table A.1 summarizes the optimum position of these filters in the RR spectrum and the corresponding temperature uncertainties. Figures A.2a,c and A.2b,d compare the wavelength sensitivity of the different investigated filter pairs in respect to the temperature uncertainty without background and with background ($S = 1$), respectively, if the respective filter would be positioned at its optimum CWL according to Table A.1.

The wavelength range in which λ_{CWL1} is positioned best is basically not affected for different filter widths. In case of λ_{CWL2} , the CWL changes towards shorter wavelengths applying broader filter curves. The single RR lines show a higher temperature dependency at lower wavelengths but on the other hand they are much weaker. The intensity of the RR lines, e.g., for N_2 is decreased by one order of magnitude between 354 nm ($J = 8$) and 352.8 nm ($J = 20$). Thus, narrow filters show better performance at longer wavelengths allowing higher signal intensities to be extracted.

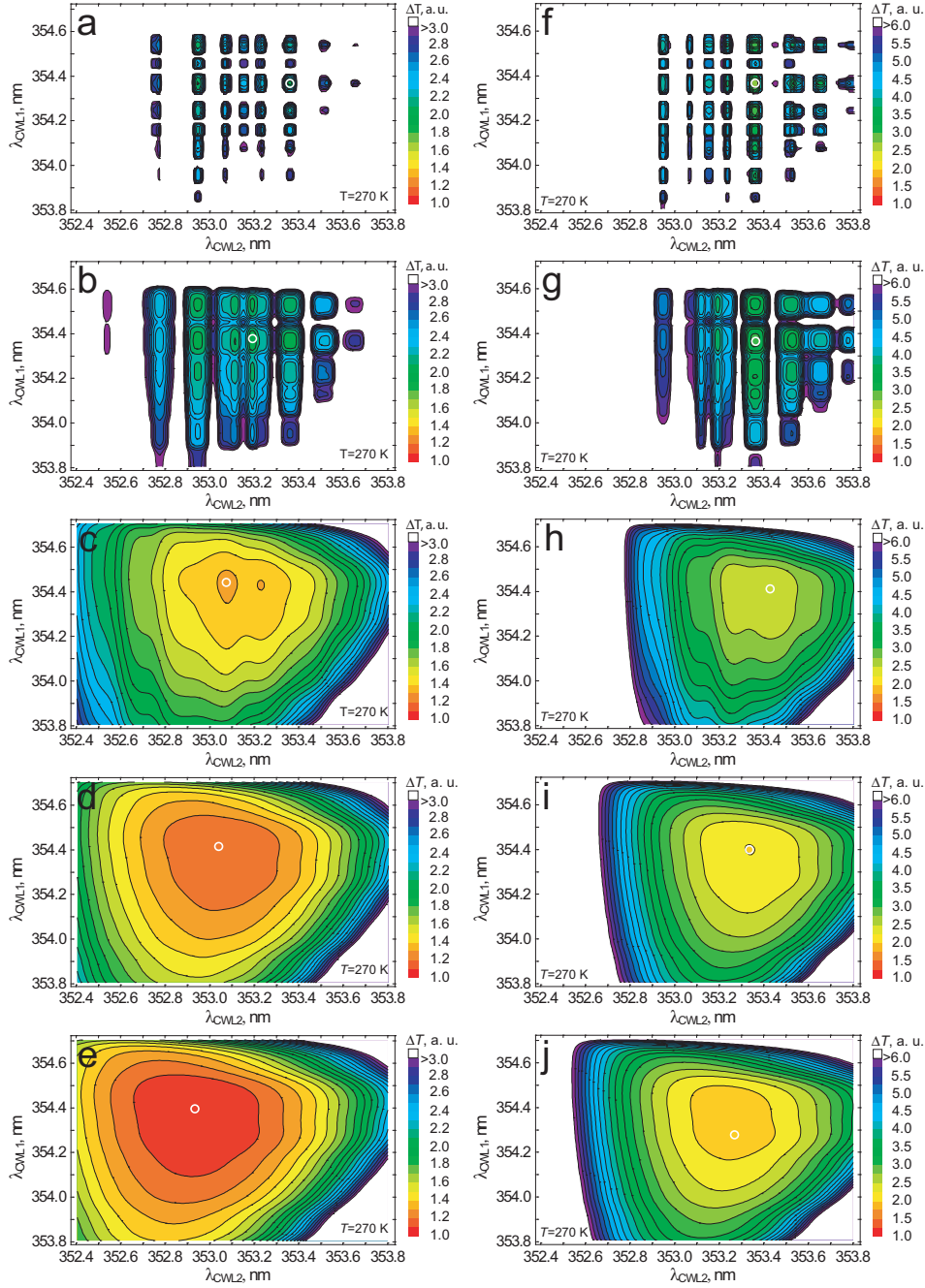


Figure A.1: Statistical temperature uncertainty ΔT versus filter CWLs λ_{CWL1} and λ_{CWL2} for different filter pairs of same bandwidth. (a) $\Delta\lambda_{\text{FWHM1,2}} = 0.05$ nm, (b) $\Delta\lambda_{\text{FWHM1,2}} = 0.1$ nm, (c) $\Delta\lambda_{\text{FWHM1,2}} = 0.3$ nm, (d) $\Delta\lambda_{\text{FWHM1}} = 0.3$ nm, $\Delta\lambda_{\text{FWHM2}} = 0.5$ nm and (e) $\Delta\lambda_{\text{FWHM1}} = 0.3$ nm, $\Delta\lambda_{\text{FWHM2}} = 0.8$ nm. (f–j) same as (a–e) but with a background signal of the same intensity as the strongest RR line in the anti-Stokes branch added to the signals. A laser wavelength of 354.7 nm was used for the calculations and temperatures between 270 K and 275 K. Calculation step width was 0.01 nm. The color scale of ΔT is plotted on the right. Values for ΔT are scaled relatively to the minimum of (e). The white circle marks the combination of lowest ΔT .

Table A.1: Optimum position for filters with the approach of a Gaussian shaped curve and idealized transmission with and without a background signal.

λ_{CWL1}	λ_{CWL2}	CWL1	CWL2	ΔT (a.u.)
Background level $S = 0$				
0.05 nm	0.05 nm	354.36 nm	353.36 nm	1.97
0.1 nm	0.1 nm	354.36 nm	353.19 nm	1.93
0.3 nm	0.3 nm	354.43 nm	353.08 nm	1.28
0.3 nm	0.5 nm	354.42 nm	353.04 nm	1.10
0.3 nm	0.8 nm	354.41 nm	352.93 nm	1.00
Background level $S = 1$				
0.05 nm	0.05 nm	354.36 nm	353.36 nm	2.53
0.1 nm	0.1 nm	354.36 nm	353.36 nm	2.95
0.3 nm	0.3 nm	354.41 nm	353.43 nm	2.30
0.3 nm	0.5 nm	354.40 nm	353.33 nm	2.00
0.3 nm	0.8 nm	354.29 nm	353.26 nm	1.85

When the background signal is taken into account it can be seen that this is not affecting λ_{CWL1} . The shift of 0.1 nm towards shorter wavelengths of the filter pair with $\Delta\lambda_{\text{FWHM1}} = 0.3$ nm and $\Delta\lambda_{\text{FWHM1}} = 0.8$ nm should not mislead the interpretation since the uncertainties are low over the whole range between 354.3 nm to 354.4 nm as shown in Fig. A.1j. By contrast, λ_{CWL2} is changed towards longer wavelengths. This is due to the larger signal intensities prevailing at these wavelengths which balance the background and, thus, keeping the temperature uncertainties small (see Eq. (4.1.7)).

The least appropriate bandwidth was found to be at around 0.1 nm. For such narrow filters, there is never more than one RR line of N_2 within the extracted signal because the RR lines are separated by ≈ 0.1 nm for a primary wavelength of 354.7 nm. Furthermore, the uncertainties are largest for $\Delta\lambda_{\text{FWHM1,FWHM2}} = 0.1$ nm considering a background signal of $S = 1$. This is also seen in Figs. A.2b,d where the minima of ΔT is enhanced by more than 15% compared to broader and more narrow filters than 0.1 nm assuming a background level of $S = 1$. The simulations showed that a pair of broader filters with different FWHM is a reasonable choice. Comparing filters with bandwidths of $\Delta\lambda_{\text{FWHM1}} = \Delta\lambda_{\text{FWHM2}} = 0.05$ nm and $\Delta\lambda_{\text{FWHM1}} = 0.3$ nm and $\Delta\lambda_{\text{FWHM2}} = 0.5$ nm, much lower statistical uncertainties are found for the broader pair of filters regardless of the intensity of the background (i.e. $S \gg 1$). This led to the conclusion to favor filters with $\Delta\lambda_{\text{FWHM1}} = 0.3$ nm and $\Delta\lambda_{\text{FWHM1}} = 0.5$ nm.

Figures A.2 show that filters with $\Delta\lambda_{\text{FWHM1,2}} > 0.1$ nm are not sensitive to a change in CWL in the region of the lowest temperature uncertainties. A misalignment of $\Delta\lambda = \pm 0.1$ nm results in an increase of ΔT of not more than 10%. Considering a background level of $S = 1$, ΔT increases by about 100% but still there is no significant sensitivity for small changes of the CWL. A filter bandwidth of 0.1 nm shows for a

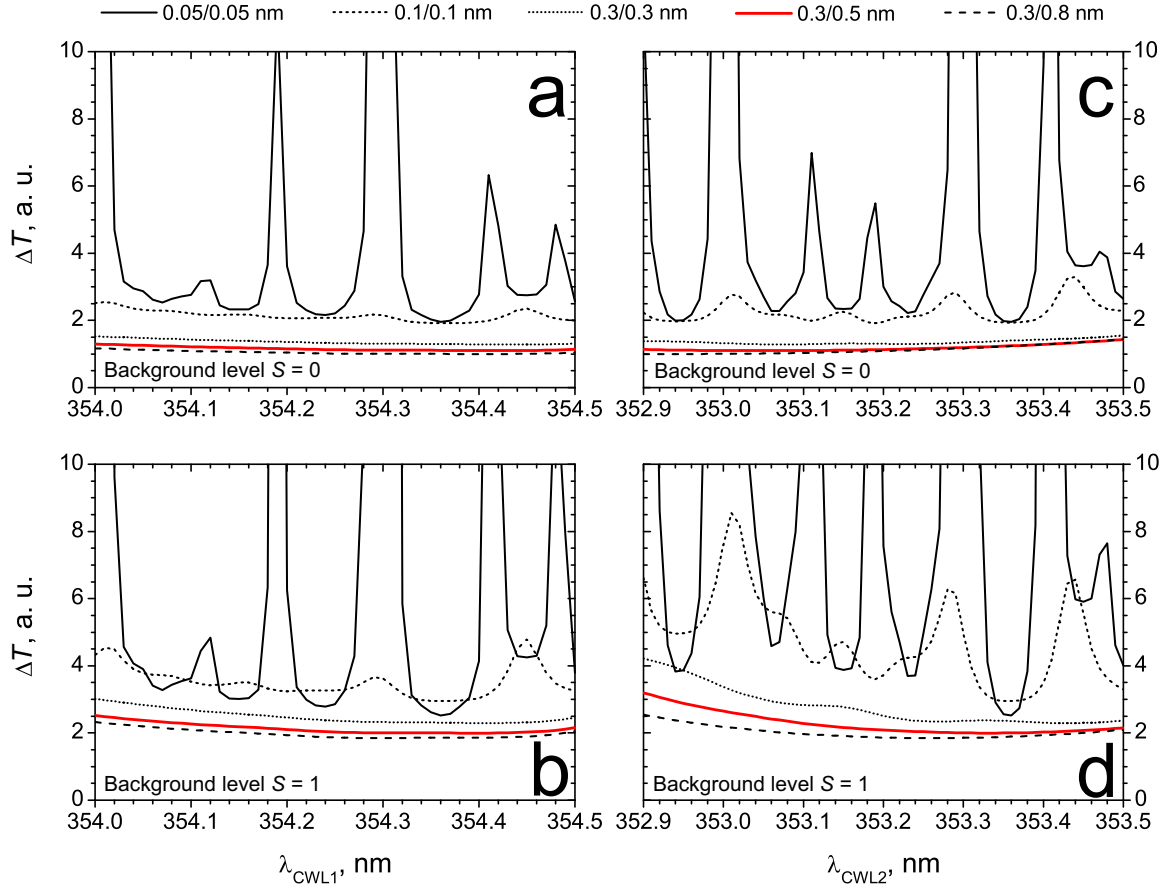


Figure A.2: Temperature uncertainty for the different filter configurations (a) for different λ_{CWL1} at optimum of λ_{CWL2} , (c) for different λ_{CWL2} at optimum of λ_{CWL1} (see Table A.1) and (b) and (d) with a background signal of the same intensity as the strongest rotational Raman line in the anti-Stokes branch added to the signals, respectively.

small change of the CWL an increase of ΔT by up to 20% and 40% for the position of λ_{CWL1} and λ_{CWL2} , respectively. These differences are amplifying by a factor of 2 assuming a background signal of $S = 1$. Filters with $\Delta\lambda_{\text{FWHM1,2}} = 0.05$ nm already show an increase of ΔT by more than 100%, if $\Delta\lambda_{\text{CWL}}$ is different by less than 0.05 nm in respect to the minimum of ΔT . Di Girolamo et al. (2004) used filter bandwidths of $\Delta\lambda_{\text{FWHM1}} = 0.2$ nm and $\Delta\lambda_{\text{FWHM2}} = 1.0$ nm and CWL's of $\lambda_{\text{CWL1}} = 354.3$ nm and $\lambda_{\text{CWL2}} = 352.9$ nm. A broader filter at λ_{CWL2} requires a larger spectral distance to the laser wavelength λ_0 in order to achieve a sufficiently high suppression at λ_0 . Thus, for daytime measurements a filter with $\Delta\lambda_{\text{FWHM2}} < 1.0$ nm is favorable which can be used closer to λ_0 .

Figure A.3 shows a comparison of the theoretical background signal P_B with a measured background signal $P_{\text{BG,Lidar}}$. The lidar data was measured during the PRINCE campaign (see Sect. 7.1) on the mountain peak Hornisgrinde (Northern Black Forest)

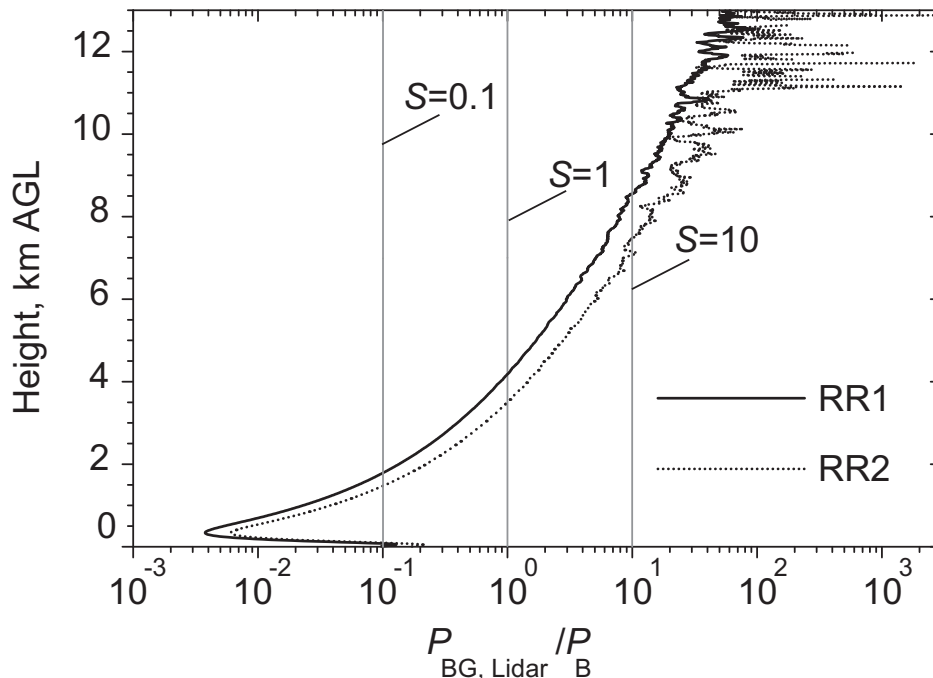


Figure A.3: Comparison of a measured daylight background in the RR channels RR1 and RR2 measured on 11 July 2006 on Hornisgrinde, 1161 m ASL (Black Forest, Germany) between 11:30 and 12:15 UTC to the simulated background P_B . Local noon is at 11:33 UTC. The ratio $P_{BG, Lidar} = P_B$ is equal to the value of S which needs to be selected to obtain the measured background according to Eq. (4.1.8) for the simulation.

on 12 July 2006 between 11:30 and 12:15 UTC. The mean solar elevation angle here was about 60° during the lidar measurement. The theoretical derived background is scaled to the measured background by $P_{Lidar}/P_{Simulation} \times P_B$, with the lidar signal P_{Lidar} and the simulated signal $P_{Simulation}$. It turned out that the simulations with the artificial background matches the reality at about 4 km altitude. Furthermore, a scaling factor of $S = 1$ is too high for heights below 4 km and too low above. Nevertheless, this does not affect the conclusions since no significant changes in optimum filter parameters were found for even much higher values of S . If S is matched to simulate the performance for higher temperatures (e.g. $S = 0.1$ for heights at around 1.5 km, which corresponds to a temperature of 285 K in that case) the optimum value for λ_{CWL2} is shifted towards shorter wavelengths by 0.1 nm whereas λ_{CWL1} is not shifted.

A.2 Simulated filter curves by Barr

Barr Associates provided simulated filter curves for the filter pair of choice with $\Delta\lambda_{FWHM1} = 0.3$ nm and $\Delta\lambda_{FWHM2} = 0.5$ nm with $\lambda_{CWL1} = 354.3$ nm and $\lambda_{CWL2} = 353.25$ nm. These filters featured a realistic transmission and filter

Table A.2: Optimum position for simulated filters with $\lambda_{\text{FWHM1}} = 0.3$ nm and $\lambda_{\text{FWHM2}} = 0.5$ nm at different atmospheric temperatures with and without a background signal.

Temperature	Background level $S = 0$		Background level $S = 1$	
	CWL1	CWL2	CWL1	CWL2
220 K	354.35 nm	353.18 nm	354.23 nm	353.40 nm
270 K	354.23 nm	353.01 nm	354.22 nm	353.22 nm
300 K	354.23 nm	352.91 nm	354.22 nm	353.19 nm

shape as well as a suppression of 7 orders of magnitude of the elastically scattered light (Behrendt, 2000, 2005). Thus, it was possible to optimize the CWL in particular. It is important to mention here that the high suppression can only be reached when using two filters for channel RR1 which was considered in the calculations.

The simulations were performed for different atmospheric temperatures ranging from 220 K to 300 K. Figures A.4a–c and A.4d–f show the results of the calculations without and with a background signal of $S = 1$, respectively. Table A.2 summarizes the optimum position of the filters in the RR spectrum. All calculations show that the region of the lowermost temperature uncertainties are displaced towards longer wavelengths whereas again the shifts of λ_{CWL1} are rather small compared to λ_{CWL2} . In the observed temperature range, the optimum for λ_{CWL2} for decreasing temperatures is changed by 0.27 nm towards longer wavelengths and by 0.21 nm considering a background signal with a scaling factor of $S = 1$. In accordance to attain optimum measurement performance during day- and nighttime conditions, the following filter parameters have been specified with an AOI of 5° for the two RR channels in respect to the laser wavelength *in vacuo* of 354.8 nm:

- RR1: $\lambda_{\text{CWL1}} = 354.4$ nm, $\Delta\lambda_{\text{FWHM1}} = 0.3$ nm
- RR2: $\lambda_{\text{CWL2}} = 353.35$ nm, $\Delta\lambda_{\text{FWHM2}} = 0.5$ nm

According to Barr Associates, with such filter parameters the high suppression of the elastically scattered light in the two RR channels should be achieved using two filters in a row for RR1. Furthermore, these filters should feature a high performance during daytime and nighttime measurements throughout the whole troposphere. As shown in Figs. A.4a–c for nighttime conditions (background level $S = 0$), ΔT is increased by about 18%, 12% and 4% compared to the minimum considering a temperature of 300 K, 270 K and 220 K, respectively. Whereas for the simulations shown in Figs. A.4d–f the difference in ΔT do not exceeds 12% for the investigated temperature range assuming a background signal with a scaling factor of $S = 1$.

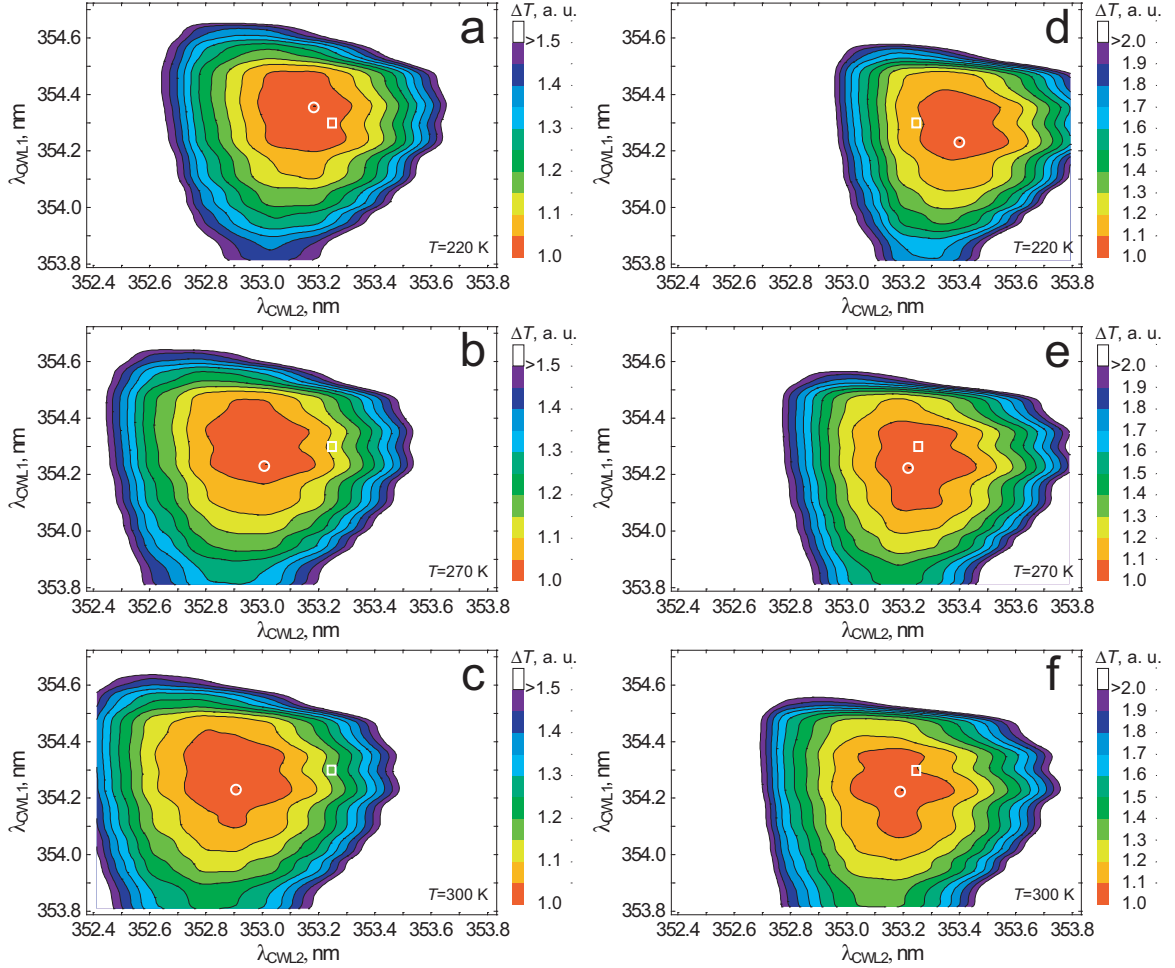


Figure A.4: Statistical temperature uncertainty ΔT versus filter CWLs λ_{CWL1} and λ_{CWL2} for filter bandwidths of $\lambda_{\text{FWHM1}} = 0.3$ nm and $\lambda_{\text{FWHM2}} = 0.5$ nm at different atmospheric temperatures. (a) $(T_1, T_2) = (220 \text{ K}, 225 \text{ K})$, (b) $(T_1, T_2) = (270 \text{ K}, 275 \text{ K})$ and (c) $(T_1, T_2) = (300 \text{ K}, 305 \text{ K})$. (d)–(f) same as (a)–(c) but with a background signal of the same intensity as the strongest RR line in the anti-Stokes branch added to the signals. A laser wavelength of 354.7 nm was used for the calculations. Calculation step width was 0.01 nm. Values for ΔT are scaled relatively to the minimum (white circle) of each plot. White rectangles mark the setup of choice according to a laser wavelength of 354.7 nm. The color scale of ΔT is plotted on the right.

Appendix B

Lidar operation times and measurement modes during PRINCE and COPS

B.1 PRINCE

Operation times of the UHOH RR lidar during the measurement campaign PRINCE in July 2006. The intensive observation period during the campaign was between 10 and 21 July 2006. The measurement modes included mainly vertical pointing measurements (green labeled) and RHI scans in east-west direction at an azimuth of 270° in respect to north. Horizontal measurements (blue labeled) were performed during overflights by the DO-128 research aircraft towards the east in direction of the flight. Conic PPI (plane position indicator) scans were performed on 12 July 2006 at an elevation angle of 45° whereas the azimuth angle was changed over the full 360° starting from 270° with 45° steps. A PPI sector scan has been performed on 15 July 2006 at an elevation angle of 45° within the azimuth of $45\text{--}135^\circ$ with a scan speed of $1^\circ/\text{s}$.

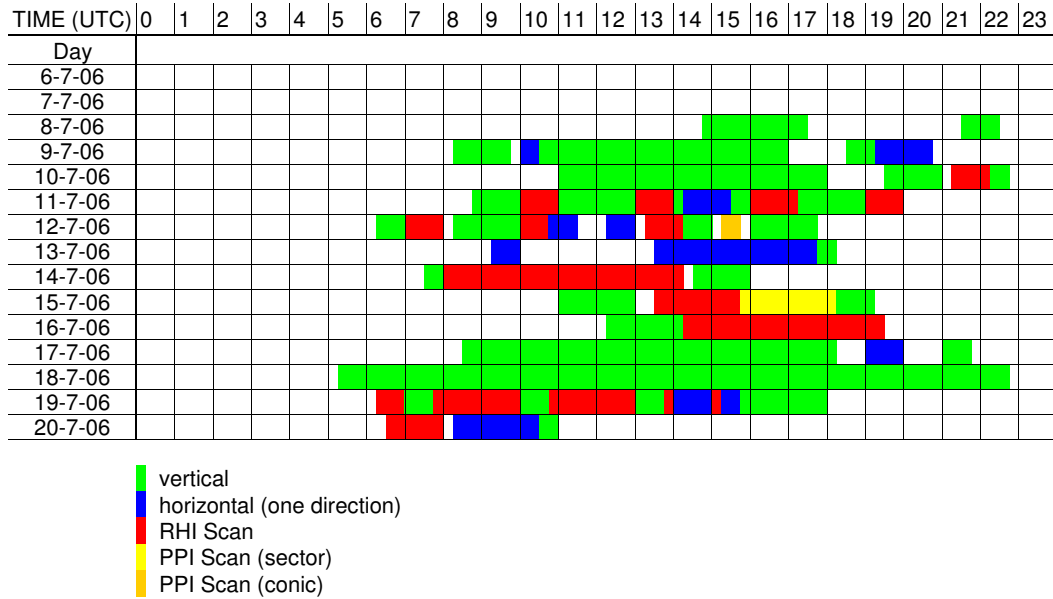


Figure B.1: Overview of the lidar operation and the different measurement modes during PRINCE from 6 July–20 July 2006 on Hornisgrinde in the Northern Black Forest, Germany.

B.2 COPS

Operation times of the UHOH RR lidar during the measurement campaign COPS from June to August 2007 (Figs. B.2–B.4). The measurement modes that were performed during the COPS intensive observation periods include vertical measurements (green labeled), one full-RHI scan along the supersites transect R–H–M (see Fig. 8.1) at an azimuth angle of 291° according to the scan pattern shown in Fig. 8.2 on the hour and on the half-hour and in between vertical measurements (green with shading) and continuous RHI scans (red labeled) along the supersites transect R–H–M at an azimuth angle of 291° according to the scan pattern shown in Fig. 8.2.

Coordinated measurements were performed on 14 August 2007 towards the Rhine Valley and the Murg Valley where Doppler-on-wheels performed measurements towards Hornisgrinde. Therefore, low elevation PPI scans (plane position indicator) were performed (blue labeled) at an elevation angle of -1° towards the Rhine Valley covering the azimuthal plane of 226 to 286° with a step width of 6° and towards the Murg Valley (only from 14:45–15:45 UTC) at an elevation angle of 1.5° covering the azimuthal plane of 46 to 96° with a step width of 5° . Furthermore, RHI scans at an azimuth angle of 270° covering the elevation angles between 0 and 45° with a step width of 5° were performed (orange labeled).

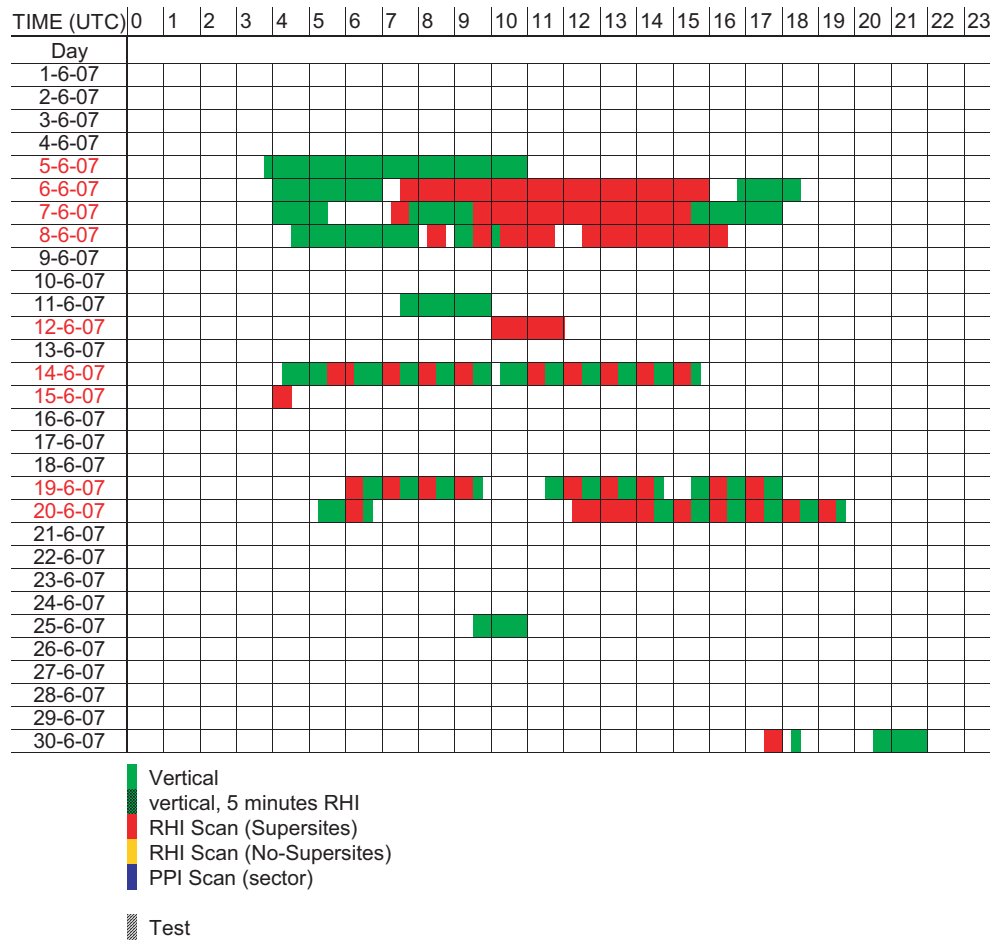


Figure B.2: Overview of the lidar operation and the different measurement modes during COPS in June 2007 on Hornisgrinde ((48.61°N, 8.20°E, 1161 m ASL) in the Northern Black Forest, Germany. IOPs are denoted by red dates.

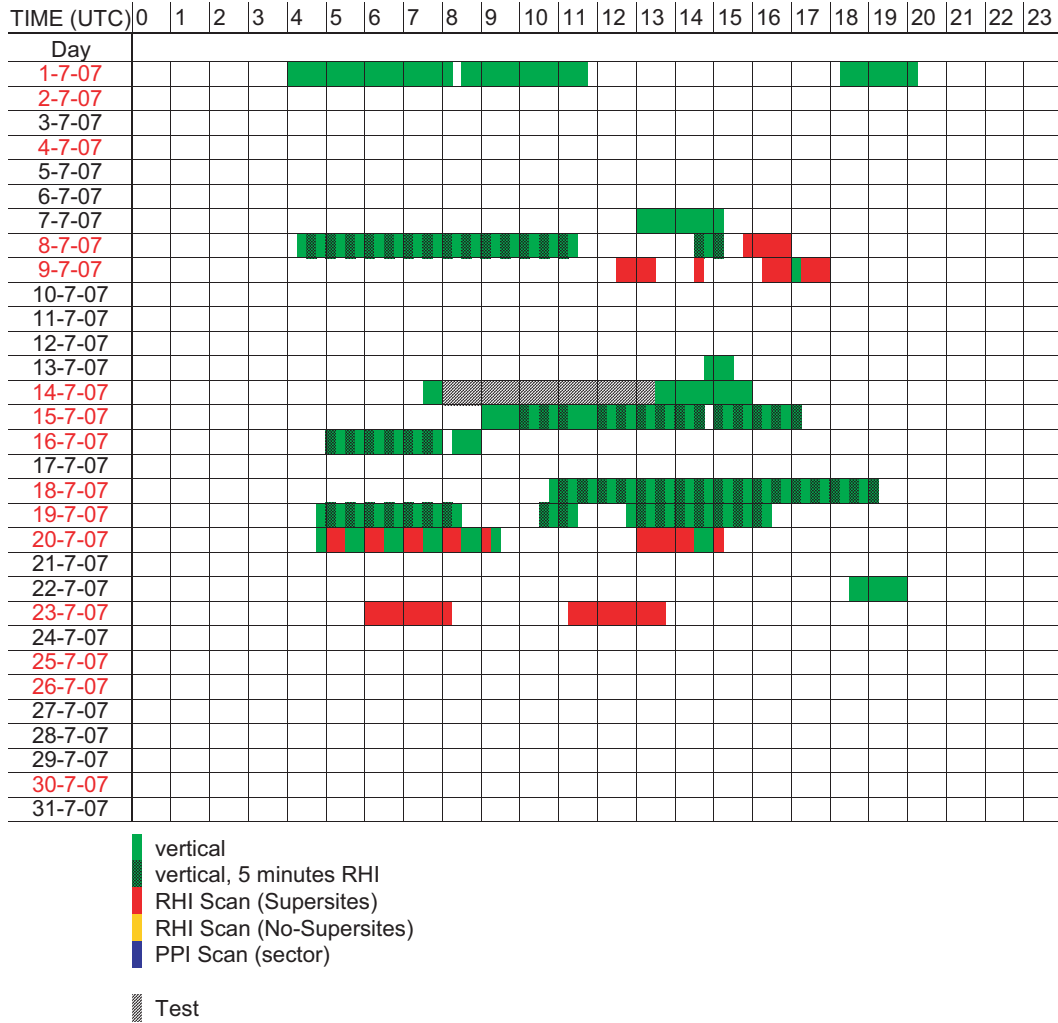


Figure B.3: Overview of the lidar operation and the different measurement modes during COPS in July 2007 on Hornisgrinde ((48.61°N, 8.20°E, 1161 m ASL) in the Northern Black Forest, Germany. IOPs are denoted by red dates.

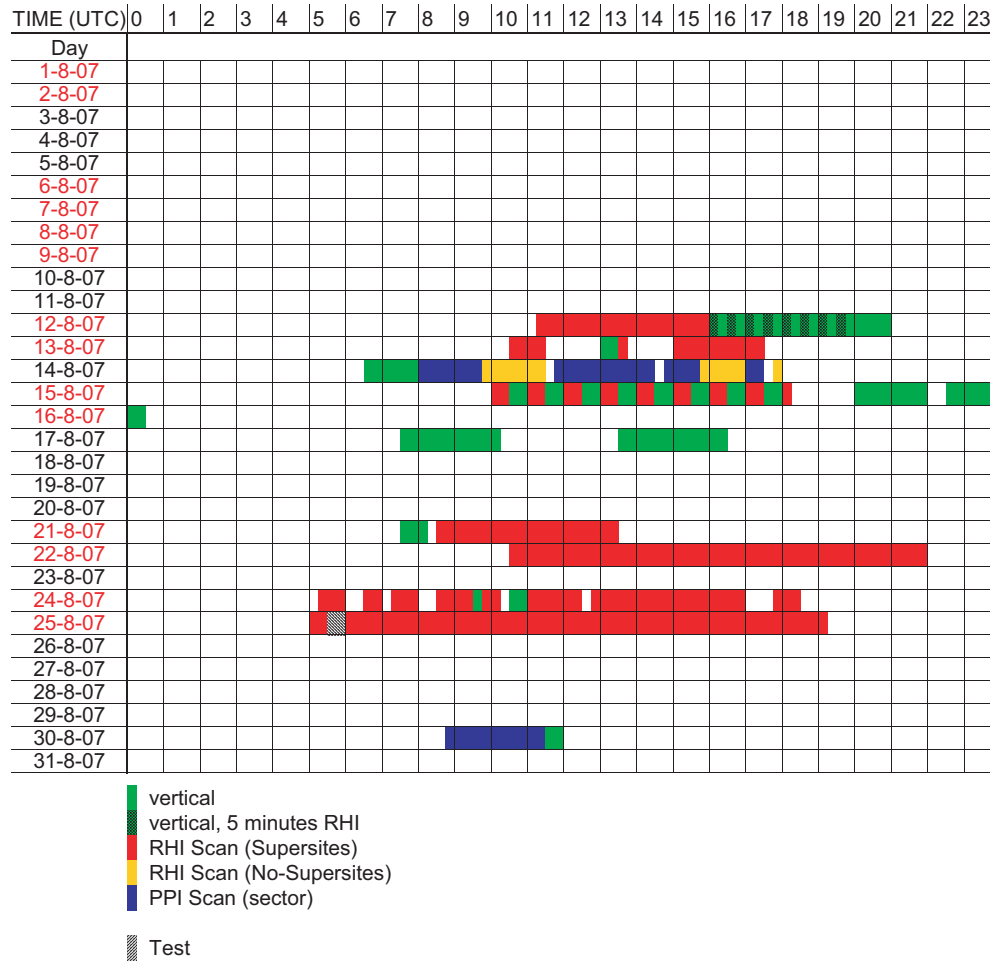


Figure B.4: Overview of the lidar operation and the different measurement modes during COPS in August 2007 on Hornisgrinde ((48.61°N, 8.20°E, 1161 m ASL) in the Northern Black Forest, Germany. IOPs are denoted by red dates.

Bibliography

- Althausen, D., Müller, D., Ansmann, A., Wandinger, U., Hube, H., Clauder, E., and Zörner, S. Scanning 6-wavelength 11-channel aerosol lidar. *J. Atmos. and Oceanic Technol.*, 17:1469–1482, 2000.
- Angevine, W. M. and Ecklund, W. L. Errors in radio acoustic sounding of temperature. *J. Atmos. and Oceanic Technol.*, 11:837–842, 1994.
- Angevine, W. M., Avery, S. K., Ecklund, W. L., and Carter, D. A. Fluxes of heat and momentum measured with a boundary-layer wind profiler radar-radio acoustic sounding system. *J. Appl. Meteorol.*, 32:73–80, 1993a.
- Angevine, W. M., Ecklund, W. L., Carter, D. A., and Gage, K. S. Improved radio acoustic sounding system. *J. Atmos. and Oceanic Technol.*, 11:42–49, 1993b.
- Ansmann, A., Wandinger, U., Riebesell, M., Weitkamp, C., and Michaelis, W. Independent measurement of extinction and backscatter profiles in cirrus clouds by using a combined Raman elastic-backscatter lidar. *Appl. Opt.*, 31:7113–7131, 1992.
- Arshinov, Y. F., Bobrovnikov, S. M., Zuev, V. E., and Mitev, V. M. Atmospheric temperature measurements using pure rotational Raman lidar. *Appl. Opt.*, 22:2984–2990, 1983.
- Arshinov, Y. F., Bobrovnikov, S. M., Serikov, I. B., Ansmann, A., Wandinger, U., Althausen, D., Mattis, I., and Müller, D. Daytime operation of a pure rotational Raman lidar by use of a Fabry-Perot interferometer. *Appl. Opt.*, 44:3593–3603, 2005.
- Bange, J. and Roth, R. Helicopter-borne flux measurements in the nocturnal boundary layer over land – a case study. *Boundary-Layer Meteorol.*, 92:295–325, 1999.
- Bange, J., Beyrich, F., and Engelbart, D. A. M. Airborne measurements of turbulent fluxes during LITFASS-98: Comparison with ground measurements and remote sensing in a case study. *Theor. Appl. Climatol.*, 73:35–51, 2002.
- Barr Associates. personal communication.
- Barthlott, C., Corsmeier, U., Meißner, C., Braun, F., and Kottmeier, C. The influence of mesoscale circulation systems on triggering convective cells over complex terrain. *Atmos. Res.*, 81:150–175, 2006.
- Behrendt, A. Temperature measurements with lidar. In Weitkamp, C., editor, *Lidar – Range-Resolved Optical Remote Sensing of the Atmosphere*. Springer, 2005.

- Behrendt, A. *Fernmessung atmosphärischer Temperaturprofile in Wolken mit Rotations-Raman-Lidar*. PhD thesis, Universität Hamburg, Fachbereich Physik, 2000.
- Behrendt, A. and Reichardt, J. Atmospheric temperature profiling in the presence of clouds with a pure rotational Raman lidar by use of an interference-filter-based polychromator. *Appl. Opt.*, 39:1372–1378, 2000.
- Behrendt, A. and Weitkamp, C. Optimizing the spectral parameters of a lidar receiver for rotational Raman temperature measurements. In *Proceedings of the 20th International Laser Radar Conference*, pages 113–116, Vichy, France, 2000.
- Behrendt, A., Nakamura, T., Onishi, M., Baumgart, R., and Tsuda, T. Combined Raman lidar for the measurement of atmospheric temperature, water vapor, particle extinction coefficient, and particle backscatter coefficient. *Appl. Opt.*, 41:7657–7666, 2002.
- Behrendt, A., Nakamura, T., and Tsuda, T. Combined temperature lidar for measurements in the troposphere, stratosphere, and mesosphere. *Appl. Opt.*, 43:2930–2939, 2004a.
- Behrendt, A., Nakamura, T., Tsuda, T., and Wulfmeyer, V. Rotational Raman temperature lidar: New experimental results and performance expected for future ground-based and airborne systems. pages 33–36, Matera, Italy, 2004b.
- Behrendt, A., Wulfmeyer, V., Kottmeier, C., and Corsmeier, U. The benefits of lidar for meteorological research: The Convective and Orographically-induced Precipitation Study (COPS). In *Proceedings of the 23rd International Laser Radar Conference*, pages 695–698, Nara, Japan, 2006.
- Behrendt, A., Wulfmeyer, V., Pal, S., Wieser, A., Radlach, M., Riede, A., Schiller, M., Träumner, K., and Fix, A. Synergetic measurements with three collocated scanning lidars: Water vapor DIAL, rotational Raman lidar, and doppler lidar. In *Proceedings of the 24th International Laser Radar Conference*, pages 1025–1028, Boulder, CO, USA, 2008.
- Bendtsen, J. The rotational and rotation-vibrational Raman spectra of $^{14}\text{N}_2$, $^{14}\text{N}^{15}\text{N}$ and $^{15}\text{N}_2$. *Journal of Raman Spectroscopy*, 2:133–145, 1974.
- Berg, L. K. and Zhong, S. Sensitivity of MM5-simulated boundary layer characteristics to turbulence parameterizations. *J. Appl. Meteor.*, 44:1467–1483, 2005.
- Bright, D. R. and Mullen, S. L. The sensitivity of the numerical simulation of the southwest monsoon boundary layer to the choice of PBL turbulence parameterization in MM5. *Wea. Forecasting*, 17:99–114, 2002.
- Browning, K. A. and Wexler, R. The determination of kinematic properties of a wind field using doppler radar. *J. Appl. Meteorol.*, 7:105–113, 1968.

- Buldakov, M. A., Matrosov, I. I., and Papova, T. N. Determination of the anisotropy of the polarisability tensor for N₂ and O₂ molecules. *Optics and Spectroscopy*, 46: 867–869, 1979.
- Butcher, R. J., Willetts, D. V., and Jones, W. J. On the use of a Fabry-Perot etalon for the determination of the rotational constants of simple molecules — the pure rotational Raman spectra of oxygen and nitrogen. *Proceedings of the Royal Society of London A*, 324:231–245, 1971. replace the exponent 2 by 3 in Eq. (8), p. 238.
- Chanin, M. L. and Hauchecorne, A. Lidar studies of temperature and density using Rayleigh scattering. *International Council of Scientific Unions Middle Atmosphere Handbook*, 13:87–98, 1984.
- Cimini, D., Hewison, T. J., Martin, L., Güldner, J., Gaffard, C., and Marzano, F. S. Temperature and humidity profile retrievals from ground-based microwave radiometers during COPS. *Meteorol. Z.*, 15:45–56, 2006.
- Cohn, S. A. and Angevine, W. M. Boundary layer height and entrainment zone thickness measured by lidars and wind-profiling radars. *J. Appl. Meteorol.*, 39:1233–1247, 2000.
- Cooney, J. Measurement of atmospheric temperature profiles by Raman backscatter. *Appl. Meteorol.*, 11:108–112, 1972.
- Cooney, J. and Pina, M. Laser radar measurement of atmospheric temperature profiles by use of Raman rotational backscatter. *Appl. Opt.*, 15:602–603, 1976.
- Corsmeier, U., Hankers, R., and Wieser, A. Airborne turbulence measurements in the lower troposphere onboard the research aircraft Dornier 128-6, D-IBUF. *Meteorol. Z.*, 10:315–329, 2001.
- Crewell, S., Czekala, H., Löhnert, U., Simmer, C., Rose, T., Zimmermann, R., and Zimmermann, R. Microwave radiometer for cloud cartography: A 22-channel ground-based microwave radiometer for atmospheric research. *Radio Sci.*, 36:621–638, 2001.
- Crutzen, P. J. and Arnold, F. Nitric acid cloud formation in the cold antarctic stratosphere. *Nature*, 324:651–655, 1986.
- Davis, K. J., Gamage, N., Hagelberg, C. R., Kiemle, C., Lenschow, D. H., and Sullivan, P. P. An objective method for deriving atmospheric structure from airborne lidar observations. *J. Atmos. Oceanic Technol.*, 17:1455–1468, 2000.
- Di Girolamo, P., Marchese, P., Whiteman, D. N., and Demoz, B. Rotational Raman lidar measurements of atmospheric temperature in the UV. *Geophys. Res. Lett.*, 31 (doi: 10.1029/2003GL018342), 2004.
- Eloranta, E. High spectral resolution lidar. In Weitkamp, C., editor, *Lidar – Range-Resolved Optical Remote Sensing of the Atmosphere*. Springer, 2005.

- Evans, D. R. *The Atomic Nucleus*. McGraw-Hill, New York, 1955.
- Feltz, W. F., Smith, W. L., Howell, H. B., Knuteson, R. O., Woolf, H., and Revercomb, H. E. Near-continuous profiling of temperature, moisture, and atmospheric stability using the Atmospheric Emitted Radiance Interferometer (AERI). *J. Appl. Meteorol.*, 42:584–597, 2003.
- Groenemeijer, P., Barthlott, C., Behrendt, A., Corsmeier, U., Handwerker, J., Kohler, M., Kottmeier, C., Mahlke, H., Pal, S., Radlach, M., Trentmann, J., Wieser, A., and Wulfmeyer, V. Observations of kinematics and thermodynamic structure surrounding a convective storm cluster over a low mountain range. *Mon. Wea. Rev.*, 2008. accepted.
- Gustafsson, N., Capaldo, M., Estrada, B. O., and Quiby, J. Position paper – requirements of observations for regional NWP. Technical report, World Meteorological Organization, 2001.
- Hair, J. W., Caldwell, L. M., Krueger, D. A., and She, C. Y. High-spectral-resolution lidar with iodine-vapor filters: measurement of atmospheric-state and aerosol profiles. *Appl. Opt.*, 40:5280–5294, 2001.
- Handwerker, J. and Görzdorf, U. Wind profiles generated with a scanning cloud radar. In *Proceedings of the 4th European Conference on Radar in Meteorology and Hydrology*, Barcelona, Spain, 2006a.
- Handwerker, J. and Görzdorf, U. A comparison of vertical cloud radar profiles with RHI scans. In *Atmospheric Profiles in Research and Operations, COST 720*, Toulouse, France, 2006b.
- Hasel, M. T. *Strukturmerkmale und Modelldarstellung der Konvektion über Mittelgebirgen*. PhD thesis, 2006.
- Heijnen, S. H., Ligthart, L.P., and Russchenberg, H.W.J. First measurements with tara; an s-band transportable atmospheric radar. *Phys.Chem.Earth(B)*, 25:995–998, 2000.
- Herzberg, G. *Molecular Spectra and Molecular Structure*, volume I. Krieger Publishing Company, 1950.
- Hofmann, D. J., Oltmans, S. J., Harris, J. M., Solomon, S., Deshler, T., and Johnson, B. J. Observation and possible causes of new ozone depletion in Antarctica in 1991. *Nature*, 359:283–287, 1991.
- Hua, D., Uchida, M., and Kobayashi, T. Ultraviolet Rayleigh-Mie lidar with mie-scattering correction by Fabry-Perot etalons for temperature profiling of the troposphere. *Appl. Opt.*, 44:1305–1314, 2005a.
- Hua, D., Uchida, M., and Kobayashi, T. Ultraviolet Rayleigh-Mie lidar for daytime-temperature profiling of the troposphere. *Appl. Opt.*, 44:1315–1322, 2005b.

- Janhäll, S., Olofson, F. G., Andersson, P. U., Pettersson, J. B. C., and Hallquist, M. Evolution of the urban aerosol during winter temperature inversion episodes. *Atmos. Env.*, 40:5355–5366, 2006.
- Kalthoff, N., Binder, H. J., Koßmann, M., Vögtlin, R., Corsmeier, U., Fiedler, F., and Schlager, H. Temporal evolution and spatial variation of the boundary layer over complex terrain. *Atmos. Env.*, 32:1179–1194, 1998.
- Keckhut, P., Chanin, M. L., and Hauchecorne, A. Stratosphere temperature measurement using Raman lidar. *Appl. Opt.*, 29:5182–5186, 1990.
- Kiemle, C., Ehret, G., Giez, A., Davis, K. J., Lenschow, D. H., and Oncley, S. P. Estimation of boundary layer humidity fluxes and statistics from airborne differential absorption lidar (DIAL). *J. Geophys. Res.*, 102(D24):29,189–29,203, 1997.
- Knuppe, K. R., Ware, R., Cimini, D., Vandenberghe, F., Vivekanandan, J., Westwater, E., Coleman, T., and Phillips, D. Ground-based passive microwave profiling during dynamic weather conditions. *J. Atmos. and Oceanic Technol.*, 2008. accepted.
- Kolmogorov, A. N. The local structure of turbulence in incompressible viscous fluid for very large Reynolds numbers. *Doklady ANSSSR*, 30:301–304, 1941.
- Koßmann, M., Corsmeier, U., Wekker, S. F. J., Fiedler, F., Vögtlin, R., Kalthoff, N., Güsten, H., and Neining, B. Observations of handover processes between the atmospheric boundary layer and the free troposphere over mountainous terrain. *Contr. Atmos. Phys.*, 72:329–350, 1999.
- Koßmann, M. R., Vögtlin, R., Corsmeier, U., Vogel, B., Fiedler, F., Binder, H.-J., and Kalthoff, N. Aspects of the convective boundary layer structure over complex terrain. *Atmos. Env.*, 32:1323–1348, 1998.
- Kottmeier, C., Reetz, T., Ruppert, P., and Kalthoff, N. A new aerological sonde for dense meteorological soundings. *J. Atmos. and Oceanic Technol.*, 18:1495–1502, 2001.
- Lammel, G., Wulfmeyer, V., Pal, S., Valdebenito, A. M., Behrendt, A., Müller, F., and Radlach, M. Aerosole aus der Nutztierhaltung (aerosols in livestock farming). <http://bwplus.fzk.de/berichte/SBer/Z03K23005+Z03K23007SBer.pdf>, 2007. Förderkennzeichen: ZO3K23005 and ZO3K23007.
- Lenschow, D. H. and Kristensen, L. Uncorrelated noise in turbulence measurements. *J. Atmos. and Oceanic Technol.*, 2:68–81, 1985.
- Lenschow, D. H., Wulfmeyer, V., and Senff, C. Measuring second- through fourth-order moments in noisy data. *J. Atmos. and Oceanic Technol.*, 17:1330–1347, 2000.
- Licel GmbH. personal communication.

- Licel GmbH. *Licel Ethernet Controller – Installation and Reference Manual*. Germany, 2008.
- Lightwave. Single-frequency injection seeding laser — user’s manual for series 6350, January 1994.
- Löhnert, U., Crewell, S., and Simmer, C. An integrated approach toward retrieving physically consistent profiles of temperature, humidity, and cloud liquid water. *J. Appl. Meteorol.*, 43:1295–1307, 2004.
- Löhnert, U., van Meijgaard, E., Baltink, H. K., Groß, S., and Boers, R. Accuracy assessment of an integrated profiling technique for operationally deriving profiles of temperature, humidity, and cloud liquid water. *J. Geophys. Res.*, 112 (doi:10.1029/2006JD007379), 2007a.
- Löhnert, U., Crewell, S., Krasnov, O., O’Connor, E., and Russchenberg, H. Advances in continuously profiling the thermodynamic state of the boundary layer: Integration of measurements and methods. *J. Atmos. and Oceanic Technol.*, 25:1251–1266, 2007b.
- Long, D. A. *The Raman Effect*. John Wiley and Sons, 2002.
- Lugauer, M. and Winkler, P. Thermal circulation in South Bavaria – climatology and synoptic aspects. *Meteorol. Z.*, 15:15–30, 2005.
- Macleod, H. A. *Thin-film optical filters*. Adam Hilger Ltd., Bristol, second edition, 1986.
- Malek, E., Davis, T., Martin, R. S., and Silva, P. J. Meteorological and environmental aspects of one of the worst national air pollution episodes (January, 2004) in Logan, Cache Valley, Utah, USA. *Atmos. Res.*, 79:108–122, 2006.
- Marling, J. 1.05–1.44 μm tunability and performance of the cw Nd³⁺:YAG laser. *IEEE Journal of Quantum Electronics*, QE-14:56–62, 1978.
- Mason, J. B. Lidar measurement of temperature: a new approach. *Appl. Opt.*, 14: 76–78, 1975.
- Mattis, I., Ansmann, A., Althausen, D., Jaenisch, V., Wandinger, U., Müller, D., Arshinov, Y. F., Bobrovnikov, S. M., and Serikov, I. B. Relative-humidity profiling in the troposphere with a Raman lidar. *Appl. Opt.*, 41:6451–6462, 2002.
- Mayor, S. D. and Spuler, S. M. Raman-shifted eye-safe aerosol lidar. *Appl. Opt.*, 43: 3915–3924, 2004.
- Monin, A. S. and Yaglom, A. M. *Statistical Fluid Mechanics*, volume 2. MIT Press, 1979.

- Muschinski, A. and Wode, C. First in situ evidence for coexisting submeter temperature and humidity sheets in the lower free troposphere. *J. Atmos. Sci.*, 55:2893–2906, 1998.
- Nedeljkovic, D., Hauchecorne, A., and Chanin, M.-L. Rotational Raman lidar to measure the atmospheric temperature from the ground to 30 km. *IEEE Trans. Geosci. Remote Sensing*, 31:90–101, 1993.
- North, E. M., Peterson, A. M., and Parry, H. D. RASS, a remote sensing system for measuring low-level temperature profiles. *Bull. Amer. Meteor. Soc.*, 54:912–919, 1973.
- Onishi, M., Behrendt, A., Kurimoto, K., Furumoto, J., Nakamura, T., and Tsuda, T. Simultaneous humidity and temperature measurements with Raman lidar and radio acoustic sounding. In *Proceedings of the 21st International Laser Radar Conference*, pages 709–712, Quebec, Canada, 2002.
- Ostermeyer, M., Kappe, P., Menzel, R., and Wulfmeyer, V. Diode-pumped Nd:YAG master oscillator power amplifier with high pulse energy, excellent beam quality, and frequency-stabilized master oscillator as a basis for a next-generation lidar system. *Appl. Opt.*, 44:582–590, 2005.
- Pal, S. *A mobile, scanning eye-safe lidar for the study of atmospheric aerosol particles and transport processes in the lower troposphere*. PhD thesis, University of Hohenheim, 2009.
- Pal, S., Behrendt, A., Radlach, M., Schaberl, T., and Wulfmeyer, V. Eye-safe scanning aerosol lidar at 355 nm. In *Proceedings of the 23rd International Laser Radar Conference*, pages 797–800, Nara, Japan, 2006.
- Pal, S., Behrendt, A., Bauer, H., Radlach, M., Riede, A., Schiller, M., Wagner, G., and Wulfmeyer, V. 3-dimensional observations of atmospheric variables during the field campaign COPS. *IOP Conf. Series: Earth and Environmental Science*, 1 (doi:10.1088/1755-1307/1/1/012031), 2008.
- Pety, D. and Turner, D. Combined analog-to-digital and photon counting detection utilized for continuous Raman lidar measurements. In *Proceedings of the 23rd International Laser Radar Conference*, Nara, Japan, 2006. post deadline paper.
- Philbrick, C. R. Raman lidar measurements of atmospheric properties. In Flood, W. A. and Miller, W. B., editors, *Atmospheric Propagation and Remote Sensing III*, Proc. SPIE 2222, pages 922–931, 1994.
- Pospichal, B. and Crewell, S. Boundary layer observations in West Africa using a novel microwave radiometer. *Meteorol. Z.*, 16:513–523, 2007.

- Powell, D. C. and Elderkin, C. E. An investigation of the application of Taylor's hypothesis to atmospheric boundary layer turbulence. *J. Atmos. Sci.*, 31:990–1002, 1974.
- Präventionsrecht-digital GbR. Laserstrahlung. <http://www.pr-o.info/bc/uvv/93/anh2.htm>.
- Press, W. H., Teukolsky, S. A., Vetterling, W. T., and Flannery, B. P. *Numerical Recipes in C*. Cambridge University Press, 2nd edition, 1992.
- Qu, J. J., Gao, W., Kafatos, M., Murphy, R. E., and Salomonson, V. V., editors. *Earth Science Satellite Remote Sensing*, volume 1. Springer, 2006.
- Radlach, M., Behrendt, A., Pal, S., Schaberl, T., and Wulfmeyer, V. Scanning rotational Raman lidar at 355 nm for the measurements of tropospheric temperature fields. In *Proceedings of the 23rd International Laser Radar Conference*, pages 699–702, Nara, Japan, 2006.
- Radlach, M., Behrendt, A., and Wulfmeyer, V. Scanning rotational Raman lidar at 355 nm for the measurement of tropospheric temperature fields. *Atmos. Chem. Phys.*, 8:159–169, 2008a.
- Radlach, M., Behrendt, A., Pal, S., Riede, A., and Wulfmeyer, V. State-of-the-art daytime scanning temperature measurements by rotational Raman lidar. In *Proceedings of the 24th International Laser Radar Conference*, pages 1056–1059, Boulder, CO, USA, 2008b.
- Revercomb, H. E., Best, F. A., Dedecker, R. G., Dirkx, T. P., Herbsleb, R. A., Knuteson, R. O., Short, J. F., and Smith, W. L. Atmospheric Emitted Radiance Interferometer (AERI) for ARM. In *Fourth Symp. on Global Climate Change Studies*, pages 46–49, Anaheim, CA, USA, 2003. Amer. Meteor. Soc.
- Richard, E., Buzzi, A., and Zängl, G. Quantitative precipitation forecasting in the Alps: The advances achieved by the Mesoscale Alpine Program. *Q.J.R. Meteor. Soc.*, 133:831–846, 2007.
- Rosen, J. M., Kjome, N. T., Larsen, N., Knudsen, B. M., Kyrö, E., Kivi, R., Karhu, J., Neuber, R., and Beninga, I. Polar stratospheric cloud threshold temperatures in the 1995–1996 arctic vortex. *J. Geophys. Res.*, 102(D23):28,195–28,202, 1997.
- Rotach, M. W. and Zardi, D. On the boundary layer structure over highly complex terrain: Key findings from MAP. *Q.J.R. Meteor. Soc.*, 133:937–948, 2007.
- Rotunno, R. and Houze, R. A. Lessons on orographic precipitation from the Mesoscale Alpine Program. *Q.J.R. Meteor. Soc.*, 133:811–830, 2007.
- Schiller, M. *High power laser transmitter for the remote definition of the atmospheric variables*. PhD thesis, University of Hohenheim, 2009.

- Schwiesow, R. L. and Lading, L. Temperature profiling by Rayleigh-scattering lidar. *Appl. Opt.*, 20:1972–1979, 1981.
- Schwitalla, T., Bauer, H.-S., Wulfmeyer, V., and G.Zängl. Systematic errors of QPF in low-mountain regions. *Meteorol. Z.*, 2008. submitted.
- Senff, C. and Peters, J. Bösenberg G. Measurement of water vapor flux profiles in the convective boundary layer with lidar and radar-RASS. *J. Atmos. Oceanic Technol.*, 11:85–93, 1994.
- Senff, C., Peters, G., and Schaberl, T. Remote sensing of turbulent ozone fluxes and the ozone budget in the convective boundary layer with DIAL and radar-RASS: A case study. *Contribu. Atmos. Phys.*, 69:161–167, 1996.
- Shimizu, H., Lee, S., and She, C. Y. High-spectral-resolution lidar system with atomic blocking filters for measuring atmospheric parameters. *Appl. Opt.*, 22:1373–1381, 1983.
- Spuler, S. M. and Mayor, S. D. Scanning eye-safe elastic backscatter lidar at 1.54 μ m. *J. Atmos. and Oceanic Technol.*, 22:696–703, 2005.
- Stein, B., Wedekind, C., Wille, H., Immler, F., Müller, M., Wöste, L., del Guasta, M., Morandi, M., Stefanutti, L., Antonelli, A., Agostini, P., Rizi, V., Readelli, G., Mitev, V., Matthey, R., Kivi, R., and Kyro, E. Optical classification, existence temperatures, and coexistence of different polar stratospheric cloud types. *J. Geophys. Res.*, 104(D19):23,983–23,993, 1999.
- Strauch, R. G., Derr, V. E., and Cupp, R. E. Atmospheric temperature measurement using Raman backscatter. *Appl. Opt.*, 10:2665–2669, 1971.
- Stull, R. B. *An Introduction to Boundary Layer Meteorology*. Kluwer Academic Publisher, Dordrecht/Boston/London, 1988.
- Taylor, I. G. The spectrum of turbulence. *Proc. Roy. Soc. London*, A164:476–490, 1938.
- Theopold, F. A. and Bösenberg, J. Differential absorption lidar measurements of atmospheric temperature profiles: Theory and experiment. *J. Atmos. and Oceanic Technol.*, 10:165–179, 1993.
- Trentmann, J., Keil, C., Salzmann, M., Barthlott, C., Bauer, H.-S., Schwitalla, T., Lawrence, M. G., Leuenberger, D., Wulfmeyer, V., Corsmeier, U., Kottmeier, C., and Wernli, H. Multi-model simulation of a convective situation in low-mountain terrain in central Europe. *Meteorol. Atmos. Phys.*, (doi:10.1007/s00703-008-0323-6), 2008.
- Wandinger, U. Raman lidar. In Weitkamp, C., editor, *Lidar – Range-Resolved Optical Remote Sensing of the Atmosphere*. Springer, 2005.

- Ware, R., Carpenter, R., Güldner, J., Liljegren, J., Nehrkorn, T., Solheim, F., and Vandenberghe, F. A multichannel radiometric profiler of temperature humidity, and cloud liquid. *Radio Sci.*, 38(doi:10.1029/2002RS002856), 2003.
- Weitkamp, C. Lidar – range-resolved optical remote sensing of the atmosphere. Springer, 2005.
- Westwater, E. R., Han, Y., Irisov, V. G., Leutskiy, V., and Kadygrov, E. N. Remote sensing of boundary layer temperature profiles by a scanning 5-mm microwave radiometer and RASS: Comparison experiments. *J. Atmos. and Oceanic Technol.*, 16: 805–818, 1999.
- Whiteman, D. N., Demoz, B., Girolamo, P. Di, Comer, J., Veselovskii, I., Evans, K., Wang, Z., Cadirola, M., Rush, K., Schwemmer, G., Gentry, B., Melfi, S. H., Mielke, B., Venable, D., and Van Hove, T. Raman lidar measurements during the International H₂O Project. Part I: Instrumentation and analysis techniques. *J. Atmos. and Oceanic Technol.*, 23:157–169, 2006.
- Whiteman, D. N., Veselovskii, I., Cadirola, M., Rush, K., Comer, J., Potter, J. R., and Tola, R. Demonstration measurements of water vapor, cirrus clouds, and carbon dioxide using a high-performance Raman lidar. *J. Atmos. and Oceanic Technol.*, 24: 1377–1388, 2007.
- Whiteman, D. N., Rush, K., Rabenhorst, S., Cadirola, M., Venable, D., Connel, R., Veselovskii, I., Demoz, B., Leblanc, T., Vömel, H., Miloshevich, L., and Joseph, E. Airborne and ground-based measurements of water vapor and aerosols using a high-performance Raman lidar. In *Proceedings of the 24th International Laser Radar Conference*, pages 87–90, Boulder, CO, USA, 2008.
- Wieser, A. The Karlsruhe Doppler wind lidar: Comparison with tower-, profiler-, sodar-, radiosonde- and thethersonde-data. http://www.imk.uni-karlsruhe.de/download/WieserEGU2005_final.pdf, 2005.
- Wulfmeyer, V. Ground-based differential absorption lidar for water-vapor and temperature profiling: development and specifications of a high-performance laser transmitter. *Appl. Opt.*, 37:3804–3824, 1998.
- Wulfmeyer, V. Investigation of turbulent processes in the lower troposphere with water vapor DIAL and radar-RASS. *J. Atmos. Sci.*, 56:1055–1076, 1999a.
- Wulfmeyer, V. Investigations of humidity skewness and variance profiles in the convective boundary layer and comparison of the latter with large eddy simulation results. *J. Atmos. Sci.*, 56:1077–1087, 1999b.
- Wulfmeyer, V. and Janjić, T. Twenty-four-hour observations of the marine boundary layer using shipborne NOAA high-resolution doppler lidar. *J. Appl. Meteorol.*, 44: 1723–1744, 2005.

- Wulfmeyer, V., Behrendt, A., and the COPS Project Investigators. COPS field report. Technical report, University of Hohenheim, 2007. URL <https://www.uni-hohenheim.de/cops/documents/COPSFeldReport2.pdf>.
- Wulfmeyer, V., Behrendt, A., Bauer, H.-S., Kottmeier, C., Corsmeier, U., Blyth, A., Craig, G., Schumann, U., Hagen, M., Crewell, S., Girolamo, P. Di, Flamant, C., Miller, M., Montani, A., Mobbs, S., Richard, E., Rotach, M.W., Arpagaus, M., Russchenberg, H., Schlüssel, P., König, M., Gärtner, V., Steinacker, R., Dorninger, M., Turner, D.D., Weckwerth, T., Hense, A., and Simmer, C. The Convective and Orographically-induced Precipitation Study: A Research and Development Project of the World Weather Research Program for improving quantitative precipitation forecasting in low-mountain regions. *Bull. Amer. Meteor. Soc.*, (DOI 10.1175/2008BAMS2367.1), 2008a.
- Wulfmeyer, V., Behrendt, A., Shiler, M., Pal, S., Riede, A., Bauer, H. S., Fix, A., Wirth, M., Ehret, G., Wandinger, U., and Althausen, D. High-resolution water-vapor measurement using a ground-based, mobile differential absorption lidar system. In *Symposium on Recent Developments in Atmospheric Applications of Radar and Lidar, 88th Annual Meeting of the American Meteorological Society*, New Orleans, LA, USA, 2008b.
- Wulfmeyer, V., Behrendt, A., Bauer, H.-S., Corsmeier, U., Kottmeier, C., Craig, G., Ehret, G., Hagen, M., Schumann, U., Volkert, H., Blyth, A., Crewell, S., Girolamo, P. Di, Flamant, C., Miller, M., Montani, A., Mobbs, S., Richard, E., Rotach, M.W., Arpagaus, M., Russchenberg, H., Schlüssel, P., König, M., Gärtner, V., Steinacker, R., Dorninger, M., Turner, D.D., and Weckwerth, T. The Convective and Orographically-induced Precipitation Study: A Research and Development Project of the World Weather Research Program. In *Proceedings of the 24th International Laser Radar Conference*, pages 722–725, Boulder, CO, USA, 2008c.
- Zeyn, J., Lahmann, W., and Weitkamp, C. Remote daytime measurements of tropospheric temperature profiles with a rotational Raman lidar. *Opt. Lett.*, 21:1301–1303, 1996.

Acknowledgements

I would like to express my profound respect and gratitude to my principal supervisor Prof. Dr. Volker Wulfmeyer, Institute of Physics and Meteorology, University of Hohenheim, for the help, support and patience.

I take this opportunity to thank my co-advisor Dr. Andreas Behrendt, Institute of Physics and Meteorology, University of Hohenheim, for continuous, invaluable and extensive support throughout the last years.

I would like to thank Prof. Dr. Christoph Kottmeier and Dr. Ulrich Corsmeier, Institute of Meteorology and Climate Research, Research Center Karlsruhe, for their continuous interest in my work. It was a nice experience to work closely with them within the VI COSI-TRACKS and COPS.

I'm thankful to my colleague Sandip Pal who was always supportive during the experiments and a very good friend in real life. He kept the scanner moving. Your authentic Indian style to cook surely is incomparable.

I thank Max Schiller, next-chair neighbor and very good friend for allowing me a little bit more insight to laser related topics.

Furthermore, I appreciated the evenings sitting together and playing Doppelkopf (thank you Matthias for teaching us).

Thanks also to Dr. Andrea Riede member of our lidar group providing her office from to time for a coffee break.

I thank Dr. Norbert Kalthoff and Martin Kohler, Institute of Meteorology and Climate Research, Research Center Karlsruhe, who contributed the data of the weather station on Hornisgrinde during the COPS experiment and Katja Träumner, from the same institute, who contributed the data of the Doppler wind lidar.

A special thanks belongs to Karsten Haustein, a friend, fellow student and original team member of SChAPLe who critically read this thesis.

Thanks to Dr. Hans-Stefan Bauer, Prof. Roland Wurster and PD Dr. Hans-Dieter

Wizemann for their comments on this thesis.

Many colleagues at our institute helped me in one way or another. Be assured that my gratitude is not less than for those mentioned here.

Many peoples at our university workshop contributed mechanical works for the modification of the mobile platform.

I'm grateful for the chances that I had during conferences and the field experiments getting in touch with the international science community.

This work was carried out within the virtual institute COSI-TRACKS (Convective Storms Virtual Institute), a virtual institute within the "Impuls- und Vernetzungsongs" of the Helmholtz Research Association between the Institute of Meteorology and Climate Research, Karlsruhe, Germany; Institute of Atmospheric Physics at the German Aerospace Center, Oberpfaffenhofen, Germany; Institute for Atmospheric Physics, University of Mainz, Germany; and the Institute of Physics and Meteorology, University of Hohenheim, Germany.

The Nd:YAG lasers were kindly provided by the Institute for Tropospheric Research (IfT) and GKSS Research Center Geesthacht. I also thank GKSS Research Center for donating the mobile platform. Furthermore, my thanks belong to Jack Fox and his team at NCAR's Design and Fabrication Services, Boulder, USA, for building the scanner of the system and the enduring support.

Last but not least I would like to thank my parents in particular: Ein großes Dankeschön gilt meinen Eltern für die fortwährende Unterstützung. Ihr habt nie den Glauben an mich verloren und mich bei all meinen Vorhaben immer unterstützt!